Glial *betaPix* is essential for blood vessel development in the zebrafish brain

ShihChing Chiu[1], Qinchao Zhou[1], Chenglu Xiao[2], Linlu Bai[1], Xiaojun Zhu[1,*], Wanqiu Ding[1,*], and Jing-Wei Xiong[1,2,*,#]

[1]Beijing Key Laboratory of Cardiometabolic Molecular Medicine, Institute of Molecular Medicine, and College of Future Technology, Peking University, Beijing 100871, China; [2]School of Basic Medical Sciences, The Second Affiliated Hospital, Institute of Biomedical Innovation, The MOE Basic Research and Innovation Center for the Targeted Therapeutics of Solid Tumors, Jiangxi Medical College, Nanchang University, Nanchang 330031, China

*Corresponding authors: WD (dingwq@pku.edu.cn), XZ (zhuxiaojun@pku.edu.cn), and JWX (jingwei_xiong@pku.edu.cn)

#Lead Contact: Jing-Wei Xiong, Ph.D. (jingwei_xiong@pku.edu.cn)

Abstract

The formation of blood-brain barrier and vascular integrity depends on the coordinative development of different cell types in the brain. Previous studies have shown that zebrafish *bubblehead* (*bbh*) mutant, which has mutation in the *betaPix* locus, develops spontaneous intracerebral hemorrhage during early development. However, it remains unclear in which brain cells *betaPix* may function. Here, we established a highly efficient conditional knockout method in zebrafish by using homology-directed repair (HDR)-mediated knockin and knockout technology, and generated *betaPix* conditional trap (*betaPix*^{ct}) allele in zebrafish. We found that *betaPix* in glia, but neither neurons, endothelial cells, nor pericytes, was critical for glial and vascular development and integrity, thus contributing to the formation of blood-brain barrier. Single-cell transcriptome profiling revealed that microtubule aggregation signaling stathmins and pro-angiogenic transcription factors *Zfhx3/4* were down-regulated in glial and neuronal progenitors, and further genetic analysis suggested that betaPix may act upstream on the PAK1-Stathmin and Zfhx3/4-Vegfaa signaling to regulate glia migration and angiogenesis. Therefore, this work reveals that glial *betaPix* plays an important role in brain vascular development in zebrafish embryos and possibly human cells.

Keywords: *betaPix*; hemorrhage; glial migration; knock-in; stathmin

Introduction

Intracerebral hemorrhage (ICH) is a life-threatening stroke type with the worst prognosis and few proven clinical treatments. Most patients who survive intracerebral hemorrhage end up with disabilities and are at risk for recurrency, cognitive decline, and systemic vascular issues, making this condition particularly significant among neurological disorders [1,2]. Several rodent models have been used for modeling ICH, including autologous blood injection, collagenase injection, thrombin injection, and micro-balloon inflation techniques [3]. Zebrafish (Danio rerio) exhibit a closed circulatory system and regulatory pathways that are highly conserved among vertebrates [4] with relatively cheap and easy to maintain disease models. Over the past decades, varieties of zebrafish mutants that spontaneously developed brain hemorrhage have been generated in mutagenesis screens, such as *redhead* [5], *reddish* [6,7] and *bubblehead* (*bbh*) [8,9]. Elucidating mutated gene function in these zebrafish models enables us to gain insights into the genetic basis and pathophysiological mechanisms of ICH development. The *bbh* mutant was identified independently in two large-scale ethylnitrosourea-induced mutagenesis screens [8,9] and positional cloning revealed that p21-activated kinase (Pak)-interacting exchange factor beta (*betaPix*) gene was mutated in *bbh* mutants [10]. *betaPix* contains SH3 domain that binds group I PAKs, and Dbl homology (DH) and pleckstrin homology (PH) domains that function as a RhoGEF to interact with Rac/Cdc42 small GTPases [11], thus participating in multiple cellular pathways to regulate cell polarity, adhesion and migration [12].

66

67 Various studies have reported that brain vessels are highly supported by neurons and

68 glial cells during development and regeneration [13,14]. Glial-specific *betaPix* have been

69 proposed to interact with *αvβ8* integrin and the Band 4.1s in glia, which link to

70 multiple intracellular signaling effectors such as *Wnt7a* and *Wnt7b* [15], but this

71 hypothesis was not experimentally addressed [16]. To this end, *betaPix* has been shown

72 to interact with *αvβ8* integrins and mediate focal adhesion formation and thus

73 modulate cerebral vascular stability in *bbh* zebrafish mutant [17]. Integrins are the main

74 molecular link between cells and the extracellular matrix (ECM) which serves as

75 scaffolds in the perivascular space. Based on a chemical suppressor screening of *bbh*

76 hemorrhages, we have previously reported that a small molecule called miconazole

77 downregulated the pErk-matrix metalloproteinase 9 (Mmp9) signaling to reduce ECM

78 degradation, thus improving vascular integrity [18]. However, how *betaPix* cell-type

79 specifically contributes to vascular integrity and maturation remains unclear. Here, we

80 generated *betaPix* conditional trap (*betaPix*^{ct}) alleles by using a CRISPR/HDR-based

81 Zwitch method, and found that *betaPix* acted mainly in glia to regulate glial and

82 vascular development and integrity *via* Stathmin and Zfhx3/4 signaling. Therefore,

83 this work provides the first experimental evidence that *betaPix* acts in glia for

84 vascular integrity development, and its functional conservation between zebrafish and

85 human cells may further guide us to decipher the genetic basis of ICH in the future.

86

87 **Results**

88 **Generating *betaPix* conditional trap (*betaPix*^{ct}) allele by an HDR-mediated**

89 **knockin and knockout method**

90 To study *betaPix* function in cell-specific manner, we utilized a donor vector with an

91 invertible gene trap cassette *via* HDR (Zwitch) [19-21] for generating *betaPix* conditional

92 trap (*betaPix*^{ct}) alleles. Zwitch consists of a splice acceptor conjugated to a red

93 fluorescent protein *via* a 2A self-cleaving peptide, flanked by two LoxP sites and two

94 Lox 5171 sites in reciprocal orientations. Outside this conditional trap cassette, we

95 included a lens-specific enhanced green fluorescence protein α-crystallin:EGFP for

96 screening knockout founders, as well as inserted both left and right arms for targeting

97 homologous sequences on the genome. We modified the Zwitch vector by adding a

98 glycine-serine-glycine (GSG) spacer in front of the 2A peptide to enhance cleavage

99 efficiency, and adding universal guide RNA (UgRNA)[22] target sequences outside the

100 left and right homologous arms for linearizing donor vector (Figures 1A and S1A).

101 We chose CRISPR/Cas9 system to generate double-strand breaks (DSBs) on intron 5

102 of the *betaPix* locus, and chose the most efficient guide RNAs based on their

103 efficiency to induce CRISPR indels. We used either long arms such as ~1000 bp or

104 short arms such as 24 bp that located upstream and downstream the guide RNA sites.

105 We then co-injected the donor vectors with targeting guide RNA, universal guide

106 RNA, and Cas9 mRNA into one-cell-stage embryos. At 4 days post-fertilization (dpf),

107 we selected α-crystallin-EGFP-positive embryos (F_0) for raising to adulthood, and

108 pre-selected F_0 founders by examining inheritable EGFP reporter expression of F_1

109 embryos. To confirm the correct homologous recombination in the *betaPix* locus, we
110 identified potential founders by genomic PCR to examine Zwitch insertion in the
111 *betaPix* locus. Precise knock-in genotypes were further verified using Sanger
112 sequencing (Figure 1B, 1C and S1B). Among 184 adult F_0 founders with
113 *α*-crystallin-EGFP expression, we found 84 founders had EGFP-positive F_1 embryos,
114 and 7 founders had expected PCR fragments around both 5' and 3' arms, which two
115 founders had correct insertions in the *betaPix* locus by Sanger sequencing (Figure
116 S1C), thus achieving ~1% efficiency on generating conditional alleles. Briefly, we
117 established an efficient method for generating conditional knockin/knockout mutants
118 in general, and generated a conditional gene trap line Ki(*betaPix*:Zwitch) in the
119 *betaPix* locus in particular, which is referred to as $betaPix^{ct}$ hereafter.
120

121 A previous work has shown that *bubblehead* (bbh^{fn40a}) mutant has a global reduction
122 in *betaPix* transcripts, and bbh^{m292} mutant has a hypomorphic mutation in *betaPix,*
123 thus establishing that *betaPix* is responsible for *bubblehead* mutant phenotypes[10].
124 bbh^{fn40a} mutants developed cerebral hemorrhages phenotype between 36 to 52 hpf
125 (Figure S1D and S1E). To characterize the $betaPix^{ct}$ allele, we injected one-cell-stage
126 $betaPix^{ct/ct}$ embryos with *Cre* mRNA to induce global inversion of Zwitch and
127 deletion of *betaPix*. As expected, we found *Cre*-induced precise inversion in
128 $betaPix^{m/m}$ as confirmed by Sanger sequencing (Figure 1C). By using *o*-dianisidine
129 staining to label hemoglobins, we found severe brain hemorrhages developed in
130 $betaPix^{m/m}$ mutant with the time window similar to bbh^{fn40a} mutants (Figure 1D and

131 1E). Consistently, qPCR analysis showed that *betaPix* decreased and *RFP* increased
132 in heterozygous *betaPix*$^{m/+}$ and homozygous *betaPix*$^{m/m}$ mutants compared with
133 *betaPix*$^{ct/ct}$ wild-type siblings, while *alphaPix* expression was not affected (Figure 1F).
134 Of note, *TagRFP* expression in *betaPix*$^{m/+}$ (after Cre-mediated recombination in
135 *betaPix*$^{ct/+}$ embryos) reflected endogenous *betaPix* expression in the boundary of
136 midbrains and hindbrains as well as the hindbrains by light-sheet fluorescence
137 microscopy imaging (Figure S1F and S1G). Together, these results suggest that the
138 conditional trap *betaPix*$^{ct/ct}$ zebrafish is functional for visualizing endogenous *betaPix*
139 expression (knockin) and performing loss-of-function study (conditional knockout).
140

141 **_betaPix_$^{m/m}$ mutant has brain hemorrhages, central arteries defects and abnormal**
142 **glial structure that is partially rescued by Pak1 inhibitor IPA3 treatment**

143 The main phenotypes in *bbh* mutants consist of brain hemorrhage and hydrocephalus
144 as early as 36 hpf, as well as poor endothelial–mesenchymal contacts and defective
145 central arteries (CtAs) sprouting in the hindbrain [10,17]. To demonstrate the
146 practicability of *betaPix* conditional trap lines, we assessed reported phenotypes
147 associated with *betaPix* deficiency using homozygous *betaPix*$^{ct/ct}$ zebrafish. Global
148 *betaPix* inactivation with *Cre* mRNA injection resulted in severe cerebral
149 hemorrhages (Figure 1D and 1E). By crossing the *betaPix*$^{m/m}$ mutant line with
150 Tg(*kdrl*:GFP) transgenic line, we found defective angiogenesis in hindbrain central
151 arteries *via* light-sheet fluorescence microscopy imaging (Figure S2A and S2B),
152 which is consistent with *betaPix* mutant phenotypes as reported [10,18].

153

154 It has been suggested that endothelial *betaPix* might not contribute to the occurrence

155 of brain hemorrhage [10]. During brain development, neurons and glia are important

156 perivascular cells and they orchestrate with endothelial cells in a temporal and spatial

157 pattern. Transgenic zebrafish that express fluorescent proteins driven by the glial

158 fibrillary acidic protein (*gfap*) promoter have been widely used for labeling glial

159 population [26]. By crossing the *betaPix*$^{m/m}$ mutant line with Tg(*gfap*:GFP) transgenic

160 line, we found that radial glial structure of the hindbrain had disoriented arrangement

161 and shorten process length in *betaPix*$^{m/m}$ embryos compared to siblings by light-sheet

162 fluorescence microscopy imaging (Figure 2A, 2B and S2C). RNA *in situ*

163 hybridization showed that neuronal and glial precursors marker *nestin* increased while

164 differentiated neuronal marker *pax2a* decreased at the hindbrain of *betaPix*$^{m/m}$

165 embryos, suggesting delayed neuronal development and differentiation after *betaPix*

166 inactivation (Figure 2C). By using global *betaPix* knockout with multiple guide-RNA

167 simultaneously [23], we found that CRISPR-induced *betaPix* mutant F_0 embryos had

168 almost identical phenotypes to those in *betaPix*^{fn40a} mutants (Figure S3A and S3B),

169 such as cerebral hemorrhages, central arteries defects, and abnormal hindbrain glial

170 and neuronal precursor development (Figure S3C to S3G), further confirming the

171 loss-of-function phenotypes in *betaPix*$^{m/m}$ mutants.

172

173 Vascularisation of the central arteries in the zebrafish hindbrain starts at 29 hpf. Tip

174 cells start to form in the dorsal side of the primordial hindbrain channels (PHBC),

175 sprout and migrate into the hindbrain tissue, moving towards the center around 36 hpf
176 to establish connections with the basilar artery. A characteristic arch architecture
177 forms at 48 hpf as boundaries dividing the hindbrain into rhombomeres[24]. In
178 Tg(*gfap*:GFP);Tg(*kdrl*:mCherry) double transgenic embryos, CRISPR-induced
179 *betaPix* knockouts showed that CtA sproutings were restricted to the bottom of glial
180 processes that failed to migrate upwards to form an arched structure in compared with
181 non-injected siblings (Figure 2D). The transcription factor SRY box-2 (Sox2) is
182 another marker gene for neuron and glial precursors. In Tg(*sox2*:GFP);
183 Tg(*kdrl*:mCherry) transgenic background, *Sox2*-positive precursor cells tightly
184 wrapped around the central artery in control siblings, but *Sox2* precursor cells had
185 loose contacts with the central arteries, with larger perivascular distances in
186 CRISPR-induced *betaPix* mutants (Figure 2E). These results implicate the impaired
187 interactions between endothelial cells and neuronal/glial cells during development
188 after *betaPix* deletion.
189
190 p21-activated kinase (Pak) is a binding partner for *betaPix*. *Pak2a* has been shown
191 mediating downstream signaling in bbh^{m292} mutants. Group I PAK allosteric
192 inhibitor IPA-3 covalently modifies and stabilizes the autoinhibitory N-terminal
193 region of PAK1, PAK2 and PAK3 [25]. As expected, IPA-3 treatment significantly
194 decreased incidence and intensity of cerebral hemorrhages in $betaPix^{m/m}$ mutant
195 embryos (Figure 2F and 2G), while IPA-3 treatment had no effect on hemorrhage
196 induction in $betaPix^{ct/ct}$ control siblings. In addition, central arterial defects were

197 partially rescued in *betaPix*$^{m/m}$ mutant embryos after IPA-3 treatment, showing
198 increased endothelial protruding into the hindbrain and more arch structure formation
199 (Figure 2H and 2I). IPA-3 treatment also decreased abnormal glial process
200 arrangements, which the lengths of glial processes statistically reached the levels of
201 the control siblings (Figure 2J). Thus, these data suggest that the *betaPix-Pak1/2*
202 signaling regulates brain vascular integrity during development.
203

204 **Glial-specific *betaPix* knockouts recapture its global knockout phenotypes**

205 To investigate *betaPix* function in different types of perivascular cells, we generated
206 glial- or neuronal-specific transgenic lines using either *gfap* [26] or *huC* [27] promoters to
207 drive *EGFP-Cre* fusion gene expression under *betaPix*$^{ct/ct}$ background, respectively
208 (Figure S4A). EGFP signals reported *Cre* expression while RFP signals efficiently
209 reported *Cre*-induced gene trap cassette inversion and disruption of *betaPix*
210 expressions (Figure S4B to S4F). Interestingly, glial-specific *betaPix* knockouts
211 developed severe cerebral hemorrhages and abnormal central arteries vascularization,
212 which were partially rescued by IPA-3 treatment (Figure 3A, 3B and 3C),
213 highlighting *betaPix* function in glia *via* Pak1/2 signaling. On the other hand, neither
214 vascular-, neuronal-, nor mural-specific deletion of *betaPix* had evident *betaPix*
215 mutant phenotypes (Figure S5A to S5D). These results suggest that glial *betaPix*
216 plays crucial roles in zebrafish embryonic vascular integrity and glial development *via*
217 regulating *Pak* activities.
218

219 **Single-cell transcriptome profiling reveals that *gfap*-positive progenitors were**

220 **affected in *betaPix* knockouts**

221 To investigate the interplays between glial and hemorrhagic pathology caused by

222 *betaPix* loss-of-function, we profiled the cranial tissues of CRISPR-edited zebrafish at

223 1 and 2 dpf using the 10X Chromium single-cell RNA sequencing (scRNA-seq)

224 platform (Figure 4A). Multi-guide targeting was able to generate almost 100% F_0 null

225 mutants, allowing us to select mutant embryos before brain hemorrhages starting from

226 36 hpf. Low-quality cells were excluded based on the numbers of genes detected and

227 percentages of reads mapped to mitochondrial genes per sample. A total of 38,670

228 cells passed quality control and were used for subsequent analyses. Uniform manifold

229 approximation and projection (UMAP) identified 71 cell clusters, which represented

230 24 zebrafish cranial cell types based on known marker gene expression profiles

231 (Figure 4B and S6A). Enriched gene markers were compared with previously

232 annotated gene markers in the ZFIN database and literatures[28,29]. By comparing the

233 proportion of cells in each sample, we found that most neuronal clusters had increased

234 relative proportions, while the numbers of glial and neuronal progenitors, endothelial

235 cells, erythrocytes, neural crests, muscles, cartilages, retinas (photoreceptor precursor

236 cells), olfactory bulbs, or epidermis and pharyneal arches were reduced in *betaPix*

237 knockout heads at 2 dpf (Figure 4C and S6B). This is consistent with the open public

238 databases of single-cell transcriptome atlas where *betaPix* is weakly expressed in a

239 broad range of cells including glia, neurons and neuronal precursors, retinas,

240 endothelial cells, pharynx, exocrine pancreas, olfactory cells and heart cells [30]. Given

241 that *betaPix* is critical in glia during brain vascular integrity development as shown
242 above (Figures 1 and 2), we examined the *gfap* expression among each cluster, and
243 found relatively high *gfap* expression in clusters including glial and neuronal
244 progenitors, hindbrain, ventral diencephalon, ventral midbrain and floor plate (Figure
245 S6A, indicated by the arrow). We next focused on the progenitor cluster owing to the
246 enriched *gfap* expression and the significantly reduced numbers of cells in this cluster
247 by *betaPix* deficiency. Furthermore, this progenitor cluster exhibited high-level
248 expression of cell proliferation and cell cycle related genes (*mki67*, *pcna*, *ccnd1*, *rrm1*
249 and *rrm2*) as well as key glial-associated genes (*gfap*, *fabp7a*, *her4*.1, *cx43*, *id1*,
250 *fgfbp3*, *atp1a1b* and *mdka*) (Table S1). From differentially expressed genes (DEGs) in
251 this progenitor cluster between controls and *betaPix* knockouts at 2 dpf, gene
252 ontology (GO) terms revealed three major categories: epigenetic remodeling,
253 microtubule organizations, and neurotransmitter secretion/transportation (Figure 4D).
254 Of these signaling genes, we were particularly interested in microtubule organizing
255 genes for further studies.
256

257 **Stathmin acts downstream of *betaPix* in glial migration *via* regulating tubulin**
258 **polymerization**

259 Microtubules are essential cytoskeletal elements composed of α/β-tubulin
260 heterodimers. The regulation of microtubule polymerization affects important cellular
261 functions such as mitosis, motor transport, and migration [31]. Based on the above
262 scRNA-seq data (Figure 4E and S6C), we examined if microtubule-destabilizing

263 protein Stathmins were affected in *betaPix* mutants. We found that *stathmin1a*
264 (*stmn1a*), *stathmin1b* (*stmn1b*), and *stathmin4l* (*stmn4l*) were relatively abundant in
265 both the whole brain and the progenitor cluster, and decreased specifically at 2 dpf in
266 *betaPix* knockout progenitor cells (Figure 4E). Subsequent qRT-PCR revealed that
267 these *Stathmin* expression decreased in both global *betaPix* knockouts (*betaPix*$^{m/m}$)
268 and glial-specific *betaPix* knockout glia (*gfap*:EGFP-Cre;*betaPix*$^{ct/ct}$) (Figure 4F and
269 4G), which was further verified by RNA *in situ* hybridization analysis (Figure 4H).
270 We next investigated whether *Stathmins* act downstream to *betaPix* signaling on
271 regulating vascular integrity development. To this end, we found that *Pak1/2*
272 inhibition enabled to rescue down-regulated expressions of *stmn1a*, *1b* and *4l* in either
273 global *betaPix*$^{m/m}$ or glial-specific *betaPix* knockout zebrafish (Figure 5A, 5B and
274 S7A), which is consistent with previous findings that *Stathmin-1* acts downstream to
275 *betaPix-Pak* signaling in neurite outgrowth in mice[32].
276
277 To test whether *Stathmin* family genes are important for vascular stability, we utilized
278 CRISPR-induced F_0 knockout system simultaneously targeting the three stathmin
279 genes. While singular stathmin gene knockout led to no evident phenotypes (data not
280 shown), we found that simultaneously inactivating *stmn1a*, *stmn1b* and *stmn4l* caused
281 brain hemorrhages and hydrocephalus in the brain, similar to that from *betaPix*^{fn40a}
282 *and betaPix*$^{m/m}$ mutants (Figure 5C, 5D, and S7B to S7E). By labeling both glia and
283 vasculature with Tg(*gfap*:GFP; *kdrl*:mCherrry) transgenic embryos, we found that
284 triple stathmin gene knockouts had impaired CtAs, abnormal glia and neuronal

285 development in the hindbrain region (Figure 5E, 5F, and S7F to S7H). Furthermore,
286 overexpressing *stmn1b* by the *gfap* promoter partially rescued brain hemorrhages and
287 delayed neuronal development in *bbh*^{fn40a} mutants (Figure 5G, 5H, S7I and S7J), of
288 which glial processes elongation also improved, but CtAs defects failed to restore
289 (Figure 5I, 5J and S7K). Thus, these data support the critical role of *stathmins* in glia.
290
291 To examine the direct role of *betaPix-stathmin* in glia, we turned to use human
292 glioblastoma cell lines and manipulated the *betaPIX* levels by siRNA knockdown or
293 transgenic overexpression. We found that *betaPIX* knockdown attenuated glial
294 migration (Figure 5K, 5L, and S7L to S7N), which is consistent with previous studies
295 on *betaPix* function in the endoderm [33], epithelial cells [34], neurons [35] and multiple
296 carcinoma cell lines including glioblastoma [36-38]. Either *betaPIX* or *STMN1*
297 overexpression led to a partial restoration of the impaired glial migration, suggesting
298 *Stathmins* as downstream effectors of *betaPix*. Furthermore, immunofluorescence
299 analysis revealed that *betaPIX* knockdown led to abnormal accumulation of
300 microtubules at the cell periphery, whereas ectopic expression of *betaPIX* and
301 *Stathmin* partially rescued these microtubule defects (Figure 5M and
302 5N). Together, these results suggest that *betaPix* depletion disrupts
303 microtubule dynamics and leads to impaired glial development acting upstream to the
304 *Pak-Stathmin* signaling, subsequently disrupting vascular integrity and resulting in
305 brain hemorrhages. While the brain hemorrhages were only partially rescued and
306 abnormal CtAs defects failed to restore, indicating that additional pathways may act

307 downstream of *betaPix*.

308

309 ***Zfhx3/4* acts downstream of *betaPix* in regulating vascular integrity development.**

310 Previous studies have identified multiple signaling pathways important for zebrafish
311 hindbrain angiogenic sprouting, such as VEGF, Notch, Wnt, Integrin β1,
312 angiopoietin/TIE, and insulin-like growth factor signaling [39-42]. To investigate whether
313 angiogenic signal is disrupted by *betaPix* depletion, we examined several angiogenic
314 gene expression pattern by performing RNA *in situ* hybridization of embryos at 36
315 hpf. The expression level of *Vegfaa* in sprouting CtAs decreased in bbh^{fn40a} mutants
316 (Figure 6A). Consistently, *betaPix* knockdown significantly reduced *VEGFA*
317 expression in cultured glial cells, which was rescued by ectopic expression of *betaPix*
318 (Figure 6B; right panel). To explore how *betaPix* regulate *Vegf* signaling in glia, we
319 re-examined the GO analysis of single-cell sequencing data and found a significant
320 enrichment of epigenetic and transcriptional regulation in glial progenitor cluster
321 (Figure 4D). Among these candidate genes, transcription factor Zinc Finger
322 Homeobox 3 (ZFHX3) is known to mediate hypoxia-induced angiogenesis in
323 hepatocellular carcinoma *via* transcriptional activation of VEGFA [43]. Furthermore,
324 ZFHX3 has been associated with stroke in multiple genome-wide association studies
325 [44-46]. Interestingly, we found that transcription factors *ZFHX3* and *ZFHX4*
326 significantly downregulated after *betaPIX* inactivation in cultured glial cells (Figure
327 6B). The transcription levels of *Zfhx3* and *Zfhx4* also downregulated in glial
328 progenitor cluster of our single cell RNA sequencing data upon *betaPix* knockout at 2

329 dpf (Figure S8A), as well as the glia-specific *betaPix* mutants (Figure S8B), thus
330 suggesting that Zfhx3/4 might acts as downstream effectors of *betaPix*.
331
332 To determine whether *Zfhx3/4* is critical for vascular integrity by interacting with
333 *betaPix* in zebrafish, we depleted *Zfhx3* and *Zfhx4* simultaneously *via*
334 CRISPR-mediated F_0 knockouts (Figure S8C to S8E). We found that *Zfhx3/4*
335 knockouts decreased *Vegfaa* expression at sprouting CtAs at 36 hpf (Figure 6C).
336 *Zfhx3/4* knockouts at 48 hpf had under-developed CtAs and reduced penetration of
337 endothelial cells into the hindbrain (Figure 6F and 6G), developed cerebral
338 hemorrhages during 36 to 52 hpf, which are comparable with *betaPix* mutant
339 phenotypes (Figure 6D to 6G). Despite up-regulated expression level of *nestin*, glial
340 arrangement and processes elongation remained statistically unaffected after *Zfhx3/4*
341 inactivation (Figure 6F, 6G and S8F). We next investigated whether increasing
342 expression level of *Vegfaa* in *betaPix* mutants was able to rescue impaired vascular
343 integrity. By using *Zfhx4* mRNA microinjection into one-cell stage embryos in either
344 bbh^{fn40a} mutants or CRISPR-induced *betaPix* knockouts, we found that ectopic
345 expression of *Zfhx4* increased *Vegfaa* expression level (Figure 6L), thus leading to a
346 drastic reduction of both percentages and volumes of brain hemorrhage shown in
347 these global *betaPix* mutants (Figure 6H, 6I, and S8G to S8I), as well as improved
348 CtAs and glial development (Figure 6J and 6K). To further explore whether
349 angiogenic potential altered in the endothelial cells, we re-examined our scRNA-seq
350 data and noted significant reduction of endothelial proportions among *betaPix*

351 knockouts (Figure S6B), which showed similar trend as glial progenitors. In this
352 endothelial cluster, CRISPR-induced *betaPix* knockouts had down-regulated
353 angiogenic gene expression at 2 dpf (Figure 6M). Despite the lack of endothelial
354 phenotype in cellular resolution in our present results, the disruptive transcriptome
355 signature in endothelial cluster suggests a potential link to the defective central
356 arterial development. Together, these data support the critical role of *Zfhx3/4* in
357 vascular integrity and glial development probably acting upstream to VEGFA and
358 downstream to *betaPix*.
359

360 **Discussion**

361 Conditional knockout technology in mice has been widely used to modify and
362 determine targeted gene function in a cell-specific manner. Spatio-temporal specific
363 modification is beneficial for studying embryonic lethality genes or investigating the
364 function of targeted genes in specific cell populations. Despite being broadly utilized
365 in mice, conditional knockouts in other animal models are limited due to technical
366 difficulties. To this end, multiple research groups have designed different strategies
367 for establishing floxed-mutant alleles, gene traps, and inducible Cas9 in zebrafish [47].
368 In particular, the Zwitch gene trap-based approach has been established successfully
369 in zebrafish, enabling to simultaneously produce knockin reporter driven by the
370 endogenous gene promoter and disrupting endogenous gene function in specific cell
371 types [19-21]. We adapted this strategy with the aid of CRISPR/Cas9 technology, and
372 added a GSG spacer to enhance cleavage efficiency and universal guide RNA target

373 sites on both homologous arms for producing linearized targeting vector. Moreover,
374 we also found that utilizing either short or long homologous arms enables to achieve
375 precise targeted integrations with this donor vector. Our short arms-based method can
376 be broadly adapted because of less restrictions on arm sequences and easily
377 engineering the donor vector. From the *betaPix* locus and other five unpublished loci
378 that we already generated, we achieved Zwitch alleles with ~1% correct insertions
379 based on homologous recombination as well as *Cre*-induced, cell-specific deletion
380 and functional analysis of targeted genes in both embryos and adult hearts. Therefore,
381 our CRISPR-based Zwitch method can be widely applied for generating conditional
382 mutant zebrafish in particular and possibly extended for other animal mutants in
383 general.
384
385 The maturation hallmark of central nervous system (CNS) vasculature is acquisition
386 of blood brain barrier (BBB) properties, establishing a stable environment crucial for
387 brain homeostasis in response to extrinsic factors and physiological changes. The core
388 features of the BBB include specialized tight junctions, highly selective
389 transporters and limited immune cell trafficking [48,49]. In zebrafish, BBB can be
390 functionally characterized from 3 dpf [50,51]. *Bubblehead* mutants acquire vessel rupture
391 phenotype early before BBB maturation, presenting a good hemorrhagic model for
392 studying early BBB development in this work. Multiple types of cells contribute to
393 diverse aspects of BBB development and maintenance, leading to proper vasculature
394 function across developmental timeline. Endothelial cells form the continuous inner

395 layer of blood vessels with junctional proteins and selective transporters, which are
396 the main subject of permeability regulation in BBB. It is well accepted that
397 endothelial cells do not show a predetermined role and that the brain environment is
398 sufficient to induce endothelial barrier [52]. Nevertheless, accumulative evidences point
399 to critical role of endothelial angiocrine signals in regulating several aspects of BBB
400 development. For example, Wnt7a/b ligands secreted by neural progenitor cells bind
401 to Frizzled receptors on endothelial cells, activating canonical Wnt signaling and
402 downstream genes. WNT ligands knockouts lead to angiogenic defects and BBB
403 leakages specifically in the CNS [53]. Endothelial GPR124, as a coactivator of canonical
404 Wnt signaling, has important function in CNS-specific angiogenesis and BBB
405 establishment [54-56]. Other signaling ligands such as angiopoietins and Ephrin family
406 ligands orchestrate with Tie or EphB receptors on endothelial cells, respectively[57].
407
408 Complex interactions between BBB cell types orchestrate proper angiogenesis and
409 CNS development in a spatio-temporal manner. Astrocytes ensheathe capillaries
410 through polarized end feet that is enriched with aquaporin-4 (Aqp4) proteins,
411 colocalized with inwardly rectified K^+ channels[58,59]. Functional coupling of ion and
412 water fluxes plays a critical role in regulating local osmotic equilibrium. During
413 development, radial glia is a neuroepithelial origin with heterogeneous populations
414 that are able to generate neurons, astrocytes, and oligodendrocytes[60-63]. In zebrafish,
415 radial glia has long been considered serving an astrocytic role. Radial glia in zebrafish
416 enriches with several key molecular markers for astrocytes and tight junctions while

417 Aqp4^{+} radial glial processes rarely contact the vasculature[64]. A more recent article has
418 reported that zebrafish *Glast*-expressing radial glia transform into astrocyte-like cells,
419 displaying dense cellular processes, tiling behavior and proximity to synapses [65].
420 Whether end feet of these astrocyte-like cells enwrap capillary blood vessels and
421 resemble mammalian astrocytes warrants future investigations. In agreement with
422 mammalian astrocytes, two independent groups have shown that ablation of pan-glia
423 results in progressive brain hemorrhage[66,67] or deficiency of spinal cord arteries
424 development in zebrafish [68], demonstrating important role of zebrafish glia in BBB
425 formation. Multiple glia/astrocyte-derived signals have been shown to contribute to
426 endothelial barrier properties development. Astrocyte-expressed sonic hedgehog (Shh)
427 bind to hedgehog (Hh) receptors on endothelial cells and contribute to the BBB
428 functions by promoting junctional protein expression and the quiescence of the
429 immune system [69-72]. Before BBB formation, notochord-derived Shh activity promote
430 arterial cell fate on developing endothelial cells [73]. Shh stimulates the production of
431 angiogenic cytokines, angiopoietins and interleukins, *via* downstream transcription
432 factor *Gli* or non-canonical pathways crosstalks with iNOS/Netrin-1/PKC,
433 RhoA/Rock, ERK/MAPK, PI3K/Akt, Wnt/β-catenin, and Notch signaling pathways [74].
434 By establishing conditional alleles of *betaPix*, we determined the critical roles of
435 betaPix in glia, but not in other brain cells, on its cerebral vessel development and
436 integrity. However, it remains unclear how glial betaPix is related to the above
437 endothelial signaling to regulate endothelial cell function and blood vessel integrity.
438

439 It has been known that Pix and Pak participate in multiple signal transduction

440 pathways [12]. We are interested in distinctive zebrafish phenotype of the *betaPix*

441 mutants that exhibit severe cranial hemorrhage and hydrocephalus. Previous studies

442 have reported *betaPix-Pak2a* signaling and downstream regulation in focal adhesion

443 essential for vascular stabilization [10,17]. The experiments reported here establish glial

444 *betaPix* mediate vascular integrity development *via* two downstream effectors

445 (Figures 6M and 7). IPA-3 has been shown to decrease the level of phosphorylated

446 PAK1 in a rat model of subarachnoid hemorrhage [75], and presented anti-angiogenic

447 activity in zebrafish [76]. Moreover, constitutively active human *Pak1* mRNA

448 administration induced cranial hemorrhage in zebrafish [77]. While previous researches

449 focused on *Pak2*, our data suggest that *Pak1* also works with *betaPix* in vascular

450 integrity development.

451

452 *Stathmin* was first discovered in a study of leukemia, of which *Stathmins are* rapidly

453 phosphorylated when induced cells undergo terminal differentiation and stopped

454 proliferation [78]. Subsequent studies have showed downregulated *Stathmin* expressions

455 after stopping proliferation of leukemia cells by chemical reagents [79]. Similar

456 expression changes of *Stathmins* are also found in other tumor cell lines such as breast

457 cancer and ovarian cancer [80,81]. *Stathmins* have also been associated with the

458 development of the central nervous system. Systemic *Stathmin* knockout mice

459 develop pan-neural axonopathy upon aging [82]. Knockdown or overexpression of

460 *Stathmin* significantly reduced the dendritic growth of Purkinje cells [83]. Moreover,

461 *Stathmin* is downregulated with the differentiation of oligodendrocyte progenitor cells
462 *in vitro* [84]. In zebrafish, *Stathmin-1* and *Stathmin-2* deficiencies resulted in defected
463 optic nerves development with ectopic branches and axonal adhesions gaps [85].
464 Knockdown or overexpression of *Stathmin-4* led to premature differentiation of dorsal
465 midbrain neural progenitors [86]. Systemic knockout of *Stmn4* showed cell cycle arrest
466 in zebrafish retinal progenitor cells [87]. These studies are consistent with our results,
467 suggesting that transcriptionally downregulated *Stathmins* are highly correlated with
468 the impaired glial development in the phenotypic analysis of this study. Previous
469 studies have revealed the role of *betaPix*-d isoform in mouse hippocampal neuron
470 development *via* regulating microtubule stability and PAK-induced *Stathmin*
471 phosphorylation [32]. It remains identified whether deletion of glial- or neuronal-*betaPix*
472 leads to brain hemorrhage. Our study found that *stathmin* knockouts impair
473 development in a variety of cell types in the zebrafish hindbrain. Importantly,
474 hemorrhage and hydrocephalus of *stathmin* knockouts partially phenocopy *betaPix*
475 mutants. *In vivo* glial-specific *Stmn1b* overexpression confers partial rescue of the
476 glial and neuronal but not vascular developmental defects in *bbh* mutants.
477 Furthermore, ectopic expression of *betaPix* and *Stathmin* alleviate the impaired cell
478 migration and cell shape maintenance in betaPix siRNA glioblastoma cells. Therefore,
479 this work suggests that the *betaPix-Pak1-Stathmin* signaling regulates vascular
480 integrity *via* glial development.
481

482 *Zfhx4* administration confers partial protection against *betaPix* depletion-induced
483 hemorrhage, establishing the novel association between the two. However, additional
484 components of this system remain to be discovered. It has been reported that
485 cAMP-response element binding protein (CREB) binds to the CRE consensus site at
486 the ZFHX3 promoter [88]. A variety of protein kinases modulate CREB activation *via*
487 phosphorylation at Ser133 [89] including protein kinase A (PKA), phosphatidylinositol
488 3-kinase (PI3K)/Akt, mitogen- and stress-activated kinase 1/2 (MSK1/2), and
489 Ca2+/calmodulin-dependent protein kinases and *Pak1* [90-92]. Our results demonstrate
490 that *Pak1* inhibition attenuated the majority of phenotypes induced by *betaPix*
491 deficiency. Thus, we speculate *Zfhx3/4* are closely associated with pathogenic
492 mechanisms downstream of *betaPix* signals by modulating expressions of
493 angiogenetic ligands. Further investigations are required to address this hypothesis.
494
495 VEGF is the main pro-angiogenic growth factor produced by various cell types that
496 controls multiple vascular development steps, such as proliferation, migration,
497 permeability and survival *via* interacting with VEGF receptors on endothelial cells.
498 Inactivation of VEGFA in astrocytes leads to BBB disruption in multiple sclerosis
499 models [93,94]. In early development of avascular neural tube, VEGF derived from
500 neuroectoderm serve as a central role in inducing tip cells sprouting from the
501 perineural vascular plexus (PVNP) and formation of vasculature lumens from stem
502 cells [95,96]. Ablating neuroglia reduces *vegfab* signals and leads to ectopic
503 intersegmental vessels sprouting and vertebral arteries in zebrafish [68]. VEGF signaling

504 orchestrates elaborately with other signaling pathways such as delta-like 4

505 (Dll4)/Notch signaling [97] and activates downstream components including the

506 Ras/Raf/MEK, PI3K/AKT, and p38/MAPK/HSP27 pathways [98]. Our data suggest

507 glial *betaPix* as an important factor in vascular integrity development. Together with

508 previous studies, *betaPix-Pak1-stathmin* signaling regulates glial growth and

509 differentiation[32] and *betaPix* might regulate *Vegfaa* secretion *via* downstream

510 transcription factors *Zfhx3/4*. Thus, this work presents novel glial *betaPix* signaling in

511 stabilizing and maintaining vascular integrity, and loss of this function causes

512 hemorrhage and subsequent disruption of the BBB (Figure 7). However, the

513 molecular mechanism of *betaPix* to *Zfhx3/4*, the sufficiency of *Vegfaa* and the

514 corresponding ligand-receptor interaction between glia and endothelial cells certainly

515 warrant future investigations.

516

517 Basement membrane is a non-cellular component consisting of several extracellular

518 matrix (ECM) proteins; serve as hub for structural supports, anchoring and

519 intercellular communication. Components of basement membrane are synthesized in

520 surrounding cells with diverse expression patterns [99]. For example, mice with deletion

521 of Collagen IV in either brain microvascular endothelial cells (BMEC)- or pericytes

522 lead to fully penetrant intracerebral hemorrhage, while COL4A1 deletion in astrocytes

523 results in mild hemorrhage phenotypes [100]. Differential cell-specific expression

524 pattern of laminin isoforms contribute differently to BBB formation [101]. As astrocytic

525 laminins mediate pericyte differentiation and regulate capillary permeability [102],

526 intercellular interactions with the ECM occur by cell surface integrin receptors.

527 Integrin β1 on endothelial cells are critical during angiogenesis[103]. On the other hand,

528 integrin αvβ8 has glial-specific enrichment which mediate focal adhesion to modulate

529 vascular integrity[17,104,105]. Notably, degradation of ECM and focal adhesions at the

530 perivascular space is critical to the hemorrhagic phenotypes of *bbh* mutants [17,18]. It

531 would be of great interest to determine whether glial *betaPix* account for ECM

532 breakdown in *bbh* mutants. Apart from *Vegfaa*, multiple pro-angiogenic growth

533 factors and signaling ligands contribute to effective glial–vascular communication in

534 the perivascular space. Interestingly, ZFHX3 has been reported activating a set of

535 procollagens, integrin and platelet-derived growth factor receptor β (*Pdgfrb*) genes in

536 response to retinoic acid stimulus, protecting cerebellar neurons from oxidative stress

537 [88]. In the future, it will be interesting to examine whether *Zfhx* signaling modulate

538 adhesion molecules in the pathogenesis of *betaPix* mutants.

539

540

541

542 **Acknowledgements**

543 The authors thank Drs. Bo Zhang, Jiulin Du, Jia Li, Liangyi Chen, Kazu Kikuchi, and
544 Jian Chen for providing fish lines, plasmid clones, and human glial cell lines; the
545 members of Dr. Xiong's laboratory for helpful discussions and technical assistance;
546 and the National Center for Protein Sciences at Peking University, particularly Dr.
547 Liying Du at the Flow Cytometry Core for technical help on the Beckman Coulter
548 MoFlo XDP; and Dr. Hua Liang at National Biomedical Imaging Center, Peking
549 University for assistance with the Luxendo Multi-View Selective-Plane Illumination
550 Microscopy (Bruker). This work is supported by grants from the National Key R&D
551 Program of China (2019YFA0801602 and 2023YFA1800600); the National Natural
552 Science Foundation of China (32230032 and 31730061).

553

554 **Declaration of Interest**

555 The authors declare no competing financial interests.

556

557 **Materials and Methods**

558 **Fish maintenance**

559 Zebrafish were raised and handled in accordance with the guidelines of the Peking
560 University Animal Care and Use Committee accredited by the AAALAC.

561 The *bbh*^{fn40a} mutant was isolated from a large-scale mutagenesis screen of the
562 zebrafish genome at Massachusetts General Hospital, Boston[9]. Tg(*acta2:GFP-Cre*)
563 was purchased from Xinjia Pharmaceutical Technology Co., Ltd (Nanjing, China);
564 Tg(*neurod:EGFP*) were kindly provided by Dr. Bo Zhang (Peking University, China);
565 Tg(*huC:GFP*) were kindly provided by Dr. Liangyi Chen (Peking University, China);
566 Tg(*kdrl:GFP*) [106] and Tg(*kdrl:mCherry*) [107] were described previously.

567

568 **Cell culture and transfection**

569 U251 and A172 human glioblastoma cell lines, kindly provided by Dr. Jian Chen at
570 Chinese Institute for Brain Research, Beijing, were cultured in high glucose DMEM
571 medium (Hyclone) supplemented with 10% fetal bovine serum and 1%
572 penicillin/streptomycin, at 37°C in 5% CO_2 humidified incubator. The *betaPIX*
573 siRNA[37] and *STMN1* siRNA[108] targeting glioblastoma cell lines as previously
574 reported were purchased from GenePharma (Shanghai, China). The sequences of the
575 siRNAs are listed in **Table S2**. The full-length coding cDNAs of human *betaPIX* or
576 *STMN1* were isolated from U251 cDNA library and subcloned into the pcDNA3.1
577 vector backbone. Transfection was conducted with Lipofectamine 3000 (Invitrogen)
578 according to manufacturer's instructions at a final siRNA concentration of 30 nM.

579

580 **mRNA/gRNA synthesis and microinjections**

581 mRNA and gRNA were synthesized as described previously [109]. In brief, linearized
582 pT3TS-nls-zCas9-nls [110], pXT7-*Cre*, and pXT7-*Zfhx4* plasmid DNA were purified as
583 templates using TIANquick Mini Purification Kit (TIANGEN, DP203, China). Next,
584 *in vitro* transcription reactions were performed using the mMESSAGE mMACHINE
585 T3 (for pT3TS-nls-zCas9-nls) or T7 (for pXT7-*Cre* and pXT7-*Zfhx4*) kits (Life
586 Technologies) according to manufacturer's instructions. Templates for gRNA were
587 generated by complementary annealing and elongation of two oligos. Forward oligo
588 contained a T7 promoter and gRNA target sequence, and reverse oligo contained the
589 universal gRNA scaffold [23]. The resulting double-stranded DNA served as the
590 templates for *in vitro* transcription using HiScribe® T7 High Yield RNA Synthesis
591 Kit (NEB). The sequences of the gRNAs are listed in **Table S3**. For global *betaPix*
592 inactivation, *Cre* mRNA with a working concentration of 200 ng/μL were injected
593 into the *betaPix*$^{ct/ct}$ embryos at one-cell stage. For CRISPR-mediated knockouts, 300
594 ng/μL Cas9 mRNA and 20-50 ng/μL gRNAs were injected into zebrafish embryos at
595 one-cell stage. For *Zfhx4* rescue experiments, *Zfhx4* mRNA with a working
596 concentration of 400 ng/μL were injected into the *bbh*^{fn40a} mutants or in combination
597 with CRISPR-mediated *betaPix* knockout system at one-cell stage. Injected embryos
598 were scored for mutant phenotypes at 36 or 48 hpf.

599

600 **Construction of *betaPix* conditional knockout zebrafish**

601 The pZwitch plasmid clone was kindly provided by Dr. Kazu Kikuchi (National
602 Cerebral and Cardiovascular Center Research Institute, Suita, Japan). GSG spacer was
603 added to pZwitch+3 between P2A and TagRFP coding sequences by overlapping
604 primer pairs. Next, a highly efficient gRNA was found from the fifth intron of *betaPix*.
605 Primer pairs were designed to amplify the left and right homologous arms from the
606 gRNA site for 1000 bp and 24 bp with following modifications: 1) The 5' end of the
607 forward primer of the left homologous arm were added with an *Nhe*1 site and a
608 universal gRNA site which provided an *in vivo* linearization cleavage site; a *Mlu*1 site
609 to the 5' end of the reverse primer of the left arm. 2) Added *EcoR*1 site to the 5' end of
610 the forward primer of the right homologous arm; added *Xho1* site and universal
611 gRNA site to the 5' end of the reverse primer of the right homologous arm. Then we
612 cloned the inverted homologous arms into polyclonal sites of the modified pZwitch+3,
613 and purified plasmid DNA with EndoFree Mini Plasmid Kit (Tiangen, DP118). *In*
614 *vivo* knock-in system was composed of 300 ng/μL Cas9 mRNA, 50 ng/μL
615 *betaPix*-intron5 gRNA, 50 ng/μL Universal gRNA, and 20 ng/μL donor vector.
616 Microinjected *in vivo* knock-in system into wildtype embryos at one-cell stage. Fish
617 founders were screened for *α*-crystallin reporter expression, raised to adulthood, and
618 re-screened for germline transmission and precise knock-in by Sanger sequencing.
619

620 **Construction of transgenic reporters**

621 The glial reporter plasmid *gfap*-EGFP [26] was kindly provided by Dr Jiulin Du
622 (Shanghai Institute for Biological Sciences, Shanghai, China). The *gfap* promoter was

623 used to establish Tg(*gfap:GFP-Cre*) plasmid. The *stmn1b* coding sequences were

624 amplified from wild-type zebrafish cDNA library, which were used to establish

625 Tg(*gfap:GFP-stmn1b*) plasmid.

626 Transgenic reporters were generated by using *Tol2*-based transgenesis [111]. In brief,

627 100 ng/μL *Tol2* transposase mRNA in combination with 20 ng/μL donor plasmid

628 DNA were co-injected into the embryos at one-cell stage. Transgenic founders were

629 screened for specific transgenic GFP expression, raised to adulthood, and re-screened

630 for germline transmission.

631

632 **Inhibitor treatment**

633 IPA-3 (Proteintech, CM05727) were dissolved in DMSO to form a 10 mM stock, and

634 then diluted with E3 medium to 3 μM in 6-well plates. Zebrafish embryos were

635 treated from 24 to 48 hpf, and then washed with E3 medium for phenotypic analysis.

636

637 ***o*-dianisidine staining**

638 *o*-dianisidine staining was performed as described previously [18]. In brief, embryos

639 were dechorionated, anesthetized and incubated in fresh staining solution (0.6 mg/mL

640 *o*-dianisidine, 0.01 M sodium acetate pH4.5, 0.65% H_2O_2 and 40% Ethanol) for 20

641 minutes in dark. Washed three times with methanol, and performed benzyl

642 alcohol/benzyl benzoate (BABB) tissue clearing before imaging with stereo

643 microscope (Leica, 160F).

644

645 **Whole-mount *in situ* hybridization (WISH)**

646 Whole-mount *in situ* RNA hybridization was performed as described previously [112].
647 Antisense probes were synthesized using a digoxigenin RNA labeling kit (Roche,
648 11277073910). Primer sequences for all WISH probes used in this paper are provided
649 in **Table S4**.

650

651 **Quantitative real-time RT-PCR**

652 Total RNA was isolated from embryos using Trizol (invitrogen) and cDNA was
653 generated using HiScript® III RT SuperMix (Vazyme) according to the
654 manufacturer's instruction. Quantitative real-time PCR was performed using
655 Lightcycler (Roche) and ChamQ SYBR qPCR Master Mix (Vazyme). Primer
656 sequences are listed in Supplementary Materials **Table S5**. Gene expression level was
657 normalized against GAPDH level.

658

659 **Light-sheet fluorescence microscopy imaging**

660 Light-sheet microscopy imaging was performed as described previously [113]. In brief,
661 transgenic zebrafish embryos were collected and maintained at 28.5°C. At the
662 required developmental stages, the embryos were carefully dechorionated, paralyzed
663 with tricaine, and transferred into 1% ultrapure low melting point agarose (16520-050;
664 Invitrogen). The embryo was then drawn into a glass tube in top-down position using
665 a 1 mL syringe with an 18G blunt needle. After agarose coagulation, a wire was
666 inserted from bottom to push the agarose with embryo upwards, removed excess agar

667 until the head area is exposed from the top of the glass tube. Finally, the glass tube
668 was fixed in a sample holder for subsequent imaging.
669 Imaging was carried out with Luxendo Multi-View Selective-Plane Illumination
670 Microscopy (Bruker). Optical calibrations were adjusted according to the instruction
671 manual.
672 The optical plates are emitted from two Nikon CFI Plan Fluor 10x W 0.3 NA
673 immersion objectives in opposite directions. The detection is completed by two
674 Olympus 20x 1.0 NA immersion lenses. The parameters are set as follows: the green
675 fluorescence channel uses a laser of 488 nm coupled with BP497-554 filter, the red
676 fluorescent channel uses laser 561 nm coupled with BP580-627 filter, with an
677 exposure time of 100 ms, a delay of 11 ms, a line mode of 50 px, and z-Stack interval
678 of 3 μm. The raw data were stored in H5 file format, processed into TIFF format and
679 merged Multi-View dataset using MATLAB software. After pre-processing,
680 multi-fluorescence channels were merged in ImageJ, and 3D visualization and
681 measurement were performed by Imaris.
682
683 **Single-cell RNA sequencing**
684 For knockout samples, 300 ng/μL Cas9 mRNA and a mixture of number 1 to 4
685 *betaPix* gRNAs with 50 ng/μL each were co-injected into wildtype embryos at
686 one-cell stage. Injection with equivalent concentration of Cas9 mRNA with PBS
687 served as siblings. After microinjection, embryos were collected and maintained at
688 28.5°C. At 24 or 48 hpf, zebrafish were dechorionated, paralyzed and transferred onto

689 agarose plate. Heads were harvested with dissecting scissors in cold sterile 1X PBS
690 with pooling 200 heads for each group. Heads were then dissociated in 900 μL
691 Accutase cell detachment solution (Sigma-Aldrich, A6964) at 28.5°C for 3 hours and
692 re-suspended by pipetting every 30 min. Once digestion was complete, 100 μL FBS
693 was added to cell suspension and centrifuged at 4℃, 500 g for 3 min. The cells were
694 gently re-suspended in cold 500 μL 2.5% FBS in 1X PBS and filtered through a 40
695 μm strainer. PI and Hoechst33342 were stained for distinguishing living cells.
696 The single, living cells were sorted by Aria SORP (BD biosciences) into 1.5 ml tubes.
697 The cell counts and vitality were verified by AOPI staining coupled with an
698 Automated Cell Counter (Countstar BioTech). Around 10,000-12,000 cells were
699 loaded for each group. Single cells were barcoded with Chromium Next GEM Single
700 Cell 3 'Reagent Kits V3.1 kit (10x Genomics, 1000269) in 10× Chromium Controller
701 (10× Genomics). After qualified by peak shapes, fragment size and tailing with
702 Fragment Analyzer System kit (Agilent Technologies, DNF-915), single-cell
703 transcriptome libraries were sequenced via Illumina High Throughput Sequencing
704 PE150 (Novogene, Beijing). The sequencing data were analyzed using the
705 CellRanger-6.1.1 (10x Genomics) and mapped to reference genome
706 GRCz11-GRCz11.103. The output numbers of reads in four sample groups are
707 494,735,089 for ctrl-1d, 615,837,087 for ko-1d, 554,470,209 for ctrl-2d and
708 583,809,243 for ko-2d.
709 Low-quality cells were excluded from subsequent analyses under the following
710 conditions: when the number of expressed genes was less than 500, when there were

711 abnormally high counts of UMIs or genes (outliers of a normal distribution), or when
712 the mitochondrial content exceeded 9%. A total of 38,670 cells were qualified for
713 subsequent analyses. Unsupervised clustering was performed using Seurat (version:
714 4.0.2) with a resolution of 2.5, resulted in 71 cell populations and further annotated
715 into 24 zebrafish major cranial cell types. Differential expression analysis in Seurat v4
716 was used to identify cluster/cell type markers by Wilcoxon rank sum test.
717

718 **Scratch assay**

719 U251 cells were planted into culture plate and performed transfection at the desired
720 density. At 24 hours post-transfection, we vertically scratched monolayer cells by
721 using a 200 μL pipette tip. Washed the cells three times with PBS, then replaced with
722 serum-free culture medium for further culture. Stereo fluorescence microscopy (Leica,
723 160F) was used to document the scratch size at 0 hours, 18 and 24 hours. Images were
724 processed by ImageJ.
725

726 **Immunostaining**

727 For assessing tubulin expression, U251 cells were planted into chamber slides
728 (Saining, 1093000) and transfected at the desired density. At 24 hours
729 post-transfection, washed the cells once on ice with pre-cooled PBS, then fixed with
730 pre-cooled methanol at -20℃ for 20 minutes. The fixed cells were permeabilized with
731 pre-cooled acetone at -20℃ for 1 minute. Removed acetone, incubated 0.5%
732 BSA/PBS blocking solution at room temperature for 15 minutes. Cells were then

733 incubated with 1:200 anti-α-tubulin mouse monoclonal antibody (EASYBIO, BE0031)

734 at 37℃ for 45 minutes. After rinsing once with PBS, cells were incubated with 1:400

735 Alexa Fluor™ 488 goat anti-mouse IgG (H+L) secondary antibody (Invitrogen,

736 A11029) at 37℃ for another 45 minutes. Washed three times with PBS, and sealed

737 with Mounting Medium with DAPI (ZSGB Bio, ZLI-9557). Images were acquired by

738 upright fluorescence microscopy (Leica, DM5000B) at 40× magnification, and

739 processed by ImageJ.

740

741 **Statistical analysis**

742 Statistical analysis was performed using Graphpad Prism 6. The statistical

743 significance of differences between the two groups was determined by the

744 independent unpaired Student's t-test. Among three or more groups, one-way

745 ANOVA analysis coupled with Dunnett's test were used. All data are presented as the

746 mean ± SEM. P value <0.05 indicates significant, with individual P values mentioned

747 in the figure/figure legends.

748

749 **Figure Legends**

750 **Figure 1. Generation of *betaPix* conditional trap (*betaPix*^{ct}) allele by an**

751 **homologous recombination (HDR)-mediated knock-in method.**

752 (A) Schematic diagram illustrates the HDR-mediated *Zwitch* strategy for

753 generating zebrafish knock-in allele at the *betaPix* locus.

754 (B) Genomic PCR analysis of the F_1 embryos confirming the right *Zwitch*

755 insertions.

756 (C) Sanger sequencing confirming the junction of *betaPix*^{ct} (after HDR-mediated

757 insertion) or *betaPix*^{m} (after Cre-mediated inversion) that are highlighted by

758 RED lines in (A).

759 (D) Representative stereomicroscopy images of erythrocytes stained with

760 *o*-dianisidine in *betaPix*$^{ct/ct}$ and *betaPix*$^{m/m}$ embryos at 48 hpf. Brain

761 hemorrhages, indicated with arrow, in *Cre* mRNA-injected embryos

762 (*betaPix*$^{m/m}$). Lateral views, anterior to the left.

763 (E) Quantification of hemorrhagic parameters in (D). Left panel showing

764 hemorrhage percentages, with independent experiments as dots. Right panel

765 showing hemorrhage areas, with each dot representing one embryo, #

766 represents the numbers of embryos scored for each analysis, and three or more

767 individual experiments conducted. Data are presented in mean ± SEM;

768 unpaired Student's t test with individual *P* values mentioned in the figure.

769 (F) qRT-PCR analysis showing the expression of *betaPix*, *RFP,* and *alphaPix* in

770 *betaPix*$^{ct/ct}$, *betaPix*$^{ct/m}$, and *betaPix*$^{m/m}$ embryos at 48 hpf. Each dot represents

771 one embryo. Data are presented in mean ± SEM; one-way ANOVA analysis

772 with Dunnett's test, individual *P* values mentioned in the figure. cryaa, α

773 A-crystallin; PA, polyadenylation signal; SA, splice acceptor; T2A,

774 T2A self-cleaving peptide. Individual scale bars indicated in the figure.

775

776 **Figure 2. *betaPix$^{m/m}$* mutant have brain hemorrhages, central artery defects and**

777 **abnormal glial structure that was partially rescued by Pak1 inhibitor IPA-**

778 **3 treatment.**

779 (A) Left panel showing the maximum intensity projection of the glial structures in

780 the hindbrain of *betaPix$^{ct/ct}$* and *betaPix$^{m/m}$* embryos at 48 hpf. Lateral view,

781 anterior to left. Middle panel showing representative optical sections and right

782 panel showing the higher magnifications of boxed area, presenting atypical

783 glial structures with disoriented arrangements (yellow arrows) in *betaPix$^{m/m}$*

784 embryos.

785 (B) Quantification of glial parameters in (A). Left panel showing the average glia

786 length, and right panel showing glia length index normalized to individual

787 head length, which each dot represents one embryo. Data are presented in

788 mean ± SEM; unpaired Student's t test with individual *P* values mentioned in

789 the figure.

790 (C) Whole-mount RNA *in situ* hybridization revealed *nestin* and *pax2a* expression

791 pattern in *betaPix$^{ct/ct}$* and *betaPix$^{m/m}$* embryos at 48 hpf. Dorsal view, anterior

792 to the left.

793 (D) Optical sections of glial structure (green) and blood vessels (magenta) in the
794 heads of siblings and CRISPR-mediated *betaPix* F_0 knockout embryos.
795 Arteries in the hindbrain of *betaPix* KO mutants had developmental defects
796 (white arrowheads), showing shorter distance between basilar artery and glial
797 cell bodies.
798 (E) 3D reconstruction of the *sox2*-positive precursors (green) and vasculatures
799 (magenta) in the heads of siblings and CRISPR-mediated *betaPix* F_0 knockout
800 embryos at 48 hpf. Box areas are shown in higher magnifications at the middle
801 panels, with optical sections shown in the right panels. Arrows indicate CtA
802 with enlarged perivascular space.
803 (F) Representative stereomicroscopy images of *o*-dianisidine staining of
804 $betaPix^{ct/ct}$ and $betaPix^{m/m}$ embryos at 48 hpf that were treated with DMSO or
805 PAK inhibitor IPA3. Brain hemorrhages indicated with arrows.
806 (G) Quantification of brain hemorrhagic parameters in (F). Left panel showing
807 hemorrhage percentages, with independent experiments as dots. Right panel
808 showing hemorrhage areas, with each dot representing one embryo, #
809 represents the numbers of embryos scored for each analysis, and three or more
810 individual experiments conducted. Data are presented in mean ± SEM;
811 one-way ANOVA analysis with Dunnett's test, individual *P* values mentioned
812 in the figure.
813 (H) Left panels showing 3D reconstruction of the glial structure (green) and
814 vasculature (magenta) in the heads of $betaPix^{ct/ct}$ and $betaPix^{m/m}$ embryos at 48

815 hpf treated with DMSO or IPA3. Lateral view, anterior to left. Box areas are
816 shown in higher magnifications at the middle panels. Defects in hindbrain
817 central arteries indicated in white arrows, while defects in radial glia indicated
818 in yellow arrows. Right panels showing schematic diagrams. Glia (grey) and
819 CtAs (pink) develop normally in DMSO or IPA3-treated *betaPix*$^{ct/ct}$ embryos,
820 with fine radial glial processes and characteristic arch vasculture. Yet in
821 *betaPix*$^{m/m}$ embryos, abnormal development of the glia and central artery
822 presented. In IPA-3-treated *betaPix*$^{m/m}$ embryos, central arterial defects were
823 partially rescued with relatively complete arch architecture, and glial processes
824 defects significantly rescued.
825 (I) Quantification of CtA parameters in (H). Left panel showing the average CtA
826 length, and right panel showing the CtA length index normalized to individual
827 head length, with each dot representing one embryo. Data are presented in
828 mean ± SEM; one-way ANOVA analysis with Dunnett's test, individual *P*
829 values mentioned in the figure.
830 (J) Quantification of glia parameters in (H). Left panel showing the average glia
831 length, and right panel showing glia length index normalized to individual
832 head length, which each dot represents one embryo. Individual scale bars
833 indicated in the figure. Data are presented in mean ± SEM; one-way ANOVA
834 analysis with Dunnett's test, individual *P* values mentioned in the figure.
835 Individual scale bars indicated in the figure. BA, basilar artery.
836

837

838 **Figure 3. Glial-specific *betaPix* knockouts recapture global *betaPix* mutant**

839 **phenotypes.**

840 (A) Representative stereomicroscopy images of erythrocytes stained with

841 *o*-dianisidine in *betaPix*$^{ct/ct}$ siblings and *gfap:GFP-Cre*; *betaPix*$^{ct/ct}$ mutant

842 embryos treated with DMSO or IPA3 at 48 hpf. Brain hemorrhages indicated

843 with arrows in glial-specific *betaPix* knockouts. Lateral view with anterior to

844 the left.

845 (B) Left panels showing 3D reconstruction of the vasculature (magenta) in the

846 heads at 48 hpf, lateral view with anterior to the left. Box areas are shown in

847 higher magnifications of brain vasculatures at the right panels. CtA defects

848 indicated in yellow arrows in *gfap:GFP-Cre*; *betaPix*$^{ct/ct}$ mutant embryos.

849 (C) Quantification of brain hemorrhages in (A) and CtA parameters in (B). Left

850 panel showing hemorrhage percentages, with independent experiments as dots.

851 Middle panel showing hemorrhage areas with each dot representing one

852 embryo. # represents the numbers of embryos scored for each analysis, three

853 or more individual experiments conducted. Right panel showing CtA length

854 index normalized to individual head length, with each dot representing one

855 embryo. Data are presented in mean ± SEM; one-way ANOVA analysis with

856 Dunnett's test, individual *P* values mentioned in the figure. Individual scale

857 bars indicated in the figure.

858

859 **Figure 4. Single cell transcriptome reveals that a subcluster of glial progenitor**

860 **and stathmin family members are associated with *betaPix* mutation.**

861 (A) Experimental strategy for single cell RNA sequencing of embryonic heads

862 from wild-type siblings and *betaPix* CRISPR mutants at 1 dpf and 2 dpf.

863 (B) UMAP visualization and clustering of cells labeled by cell type. Four samples

864 were aggregated and analyzed together.

865 (C) Proportions of 24 cell clusters were differentially distributed among four

866 sample groups. ctrl_1d, PBS-injected siblings at 1 dpf; ko_1d, *betaPix*

867 CRISPR mutants at 1 dpf; ctrl_2d, PBS-injected siblings at 2 dpf; ko_2d,

868 *betaPix* CRISPR mutants at 2 dpf.

869 (D) Enriched GO terms for differentially expressed genes for progenitor

870 sub-cluster comparing ko_2d to ctrl_2d groups.

871 (E) Violin plots showing the expression of the stathmin family genes by all cells

872 among four sample groups (left panel) or by progenitor sub-cluster among

873 four sample groups (right panel).

874 (F) qRT-PCR analysis showing expression of *betaPix*, *stmn1a*, *stmn1b*, *stmn4l*

875 and *ppfia3* in glia of FACS-sorted $betaPix^{ct/ct}$ siblings and $betaPix^{m/m}$ mutants

876 at 48 hpf. Each dot represents cells sorted from one embryo. Data are

877 presented in mean ± SEM. ***P <0.005; ****P<0.001; unpaired

878 Student's t test.

879 (G) qRT-PCR analysis showing expression of *betaPix*, *stmn1a*, *stmn1b*, *stmn4l*

880 and *ppfia3* in glia of FACS-sorted $betaPix^{ct/ct}$ siblings and *gfap:GFP-Cre*;

881 *betaPix*$^{ct/ct}$ mutants at 48 hpf. Each dot represents cells sorted from one embryo.

882 Data are presented in mean ± SEM. ***P <0.005; ****P<0.001; unpaired

883 Student's t test.

884 (H) Whole-mount RNA *in situ* hybridization revealing down-regulation of *stmn1a*,

885 *stmn1b* and *stmn4l* in *betaPix*$^{ct/ct}$ siblings and *gfap:GFP-Cre*; *betaPix*$^{ct/ct}$

886 mutant embryos at 48 hpf. Individual scale bars indicated in the figure.

887

888 **Figure 5. *Stathmin* acts downstream of *betaPix* in glial migration *via* regulating**

889 **tubulin polymerization.**

890 (A) Whole-mount RNA *in situ* hybridization showing that *stmn1a, stmn1b and*

891 *stmn4l* expression in *gfap:GFP-Cre*; *betaPix*$^{ct/ct}$ embryos were partially

892 rescued by Pak1 inhibitor IPA3 treatment at 48 hpf. Dorsal views, anterior to

893 the left.

894 (B) qRT-PCR analysis showing that *stmn1a* and *stmn4l* expression were rescued

895 in *gfap:GFP-Cre*; *betaPix*$^{ct/ct}$ mutants by IPA3 treatment at 48 hpf. Each dot

896 represents one embryo. Data are presented in mean ± SEM; one-way ANOVA

897 analysis with Dunnett's test, individual P values mentioned in the figure.

898 (C) Representative stereomicroscopy images of erythrocytes stained with

899 *o*-dianisidine in siblings and *stmn1a/1b/4l* CRISPR mutants at 48 hpf. Brain

900 hemorrhages, indicated with arrows, appeared in *stmn1a/1b/4l* mutants.

901 Lateral views with anterior to the left.

902 (D) Quantification of hemorrhagic parameters in (C). Left panel showing
903 hemorrhage percentages, with independent experiment as dot. Right panel
904 showing hemorrhage areas with each dot representing one embryo. #
905 represents the numbers of embryos scored for each analysis, three or more
906 individual experiments conducted. Data are presented in mean ± SEM;
907 unpaired Student's t test with individual *P* values mentioned in the figure.
908 (E) 3D reconstruction of glial structure (green) and vasculature (magenta) in the
909 heads at 48 hpf. Lateral view with anterior to the left. CtA defects (white
910 arrows) indicated in *stmn1a/1b/4l* mutants.
911 (F) Quantification of CtA and glia parameters in (E). Length index normalized to
912 individual head length, with each dot representing one embryo. Data are
913 presented in mean ± SEM; unpaired Student's t test with individual *P* values
914 mentioned in the figure.
915 (G) Representative stereomicroscopy images of erythrocytes stained with
916 *o*-dianisidine in bbh^{fn40a} and bbh^{fn40a}; Tg(*gfap:GFP-stmn1b*) embryos at 48 hpf.
917 Brain hemorrhages, indicated with arrows, decreased in bbh^{fn40a} mutants with
918 glia-specific overexpression of *stmn1b*, compared with bbh^{fn40a} mutant siblings.
919 Lateral views with anterior to the left.
920 (H) Quantification of hemorrhagic parameters of (G). Left panel showing
921 hemorrhage percentages, with independent experiment as dot. Right panel
922 showing hemorrhage areas with each dot representing one embryo. #
923 represents the numbers of embryos scored for each analysis, three or more

924 individual experiments conducted. Data are presented in mean ± SEM;

925 unpaired Student's t test with individual *P* values mentioned in the figure.

926 (I) 3D reconstruction of the *gfap:GFP-stmn1b* overexpression (green) and

927 vasculature (magenta) in the heads of bbh^{fn40a} siblings and bbh^{fn40a};

928 Tg(*gfap:GFP-stmn1b*) mutants at 48 hpf. Lateral view with anterior to

929 left. White arrows indicate CtA defects.

930 (J) Quantification of CtA and glia parameters in (I). Length index normalized to

931 individual head length, with each dot representing one embryo. Data are

932 presented in mean ± SEM; unpaired Student's t test with individual *P* values

933 mentioned in the figure.

934 (K) Representative stereomicroscopy images of U251 cells at 0 and 24 hours after

935 wounding. U251 cells were transfected with negative control siRNA or

936 *betaPIX* siRNA separately, in combination with pcDNA3.1 vector, *betaPIX*

937 overexpression plasmid, and *STMN1* overexpression plasmid. The wound

938 edges are highlighted by dashed lines, with arrow lines indicating the wound

939 width.

940 (L) Quantification of wound closure in (K), showing $^{*}P<0.05$, $^{***}P<0.005$

941 compared to negative control siRNA with empty vector transfection. $^{\#\#}P<0.01$,

942 $^{\#\#\#}P<0.005$ compared to *betaPix* knockdown with empty vector transfection.

943 Data are presented in mean ± SEM; one-way ANOVA analysis with Dunnett's

944 test.

945 (M) Representative immunofluorescence image of alpha-tubulin and DAPI

946 signals in U251 cells. U251 cells were transfected with negative control

947 siRNA or *betaPIX* siRNA separately, in combination with pcDNA3.1 vector,

948 *betaPIX* overexpression plasmid, and *STMN1* overexpression plasmid. Box

949 areas are shown in higher magnifications. Arrows indicate protrusions at the

950 cell periphery.

951 (N) Quantification of cell percentages with protrusions in (M). $^{***}P<0.005$

952 compared to negative control siRNA with empty vector transfection. $^{\#}P<0.05$,

953 $^{\#\#}P<0.01$ compared to *betaPix* knockdown with empty vector transfection.

954 Data are presented in mean ± SEM; one-way ANOVA analysis with Dunnett's

955 test. Individual scale bars indicated in the figure.

956

957 **Figure 6. *Zfhx3/4* acts downstream of *betaPix* to regulate vascular integrity**

958 **development.**

959 (A) Whole-mount RNA *in situ* hybridization revealing that *Vegfaa* decreased in

960 bbh^{fn40a} mutants compared with siblings at 36 hpf. Lateral views with anterior

961 to the left. Arrows indicate *vegfaa* expression in the CtAs that shown depletion

962 in bbh^{fn40a} mutants.

963 (B) qRT-PCR analysis revealing that *ZFHX3*, *ZFHX4 and* VEGFA decreased in

964 U251 cells transfected with *betaPIX* siRNA, which were rescued by *betaPIX*

965 overexpression. Data are presented in mean ± SEM; one-way ANOVA

966 analysis with Dunnett's test, individual *P* values mentioned in the figure.

967 (C) Whole-mount RNA *in situ* hybridization showing that *vegfaa* decreased in

968 CRISPR-mediated *zfhx3/4* F_0 knockout embryos at 36 hpf. Lateral views with

969 anterior to the left. Arrows indicate *vegfaa* expression in the CtAs that shown

970 reduction in *zfhx3/4* knockouts.

971 (D) Representative stereomicroscopy images of erythrocytes stained with

972 *o*-dianisidine in siblings and CRISPR-mediated *zfhx3/4* F_0 knockout embryos

973 at 48 hpf. Arrows indicated brain hemorrhages in the knockout brains. Lateral

974 views with anterior to the left.

975 (E) Quantification of hemorrhagic parameters in (D). Left panel showing

976 hemorrhage percentages, with independent experiment as dot. Right panel

977 showing hemorrhage areas with each dot representing one embryo. #

978 represents the numbers of embryos scored for each analysis, three or more

979 individual experiments conducted. Data are presented in mean ± SEM;

980 unpaired Student's t test with individual *P* values mentioned in the figure.

981 (F) Left panel showing 3D reconstruction of the glial structure (green) and

982 vasculature (magenta) in the hindbrain of siblings and CRISPR-mediated

983 *zfhx3/4* F_0 knockouts at 48 hpf. Lateral view with anterior to the left. White

984 arrows indicate CtA defects. Right panels showing schematic diagrams. Glia

985 (grey) developed normally in both treatment, while defects in central artery

986 (pink) presented in *zfhx3/4* knockout embryos.

987 (G) Quantification of CtA and glia length parameters of (F). Length index

988 normalized to individual head length, with each dot representing one embryo.

989 Data are presented in mean ± SEM; unpaired Student's t test with individual *P*

990 values mentioned in the figure.

991 (H) Representative stereomicroscopy images of erythrocytes stained with

992 *o*-dianisidine in CRISPR-mediated *betaPix* F0 knockout embryos with or

993 without *zfhx4* mRNA injection at 48 hpf. Arrows indicate brain hemorrhages.

994 Lateral views with anterior to the left.

995 (I) Quantification of hemorrhagic parameters in (H). Left panel showing

996 hemorrhage percentages, with independent experiment as dot. Right panel

997 showing hemorrhage areas with each dot representing one embryo. #

998 represents the numbers of embryos scored for each analysis, three or more

999 individual experiments conducted. Data are presented in mean ± SEM;

1000 unpaired Student's t test with individual *P* values mentioned in the figure.

1001 (J) Left panel showing 3D reconstruction of the glial structure (green) and

1002 vasculature (magenta) in CRISPR-mediated *betaPix* F_0 knockout embryos

1003 with or without *zfhx4* mRNA injection at 48 hpf. White arrows indicate CtAs

1004 and yellow arrows indicate glia. Right panels showing schematic diagrams.

1005 Glia (grey) and CtA (pink) developmental defects rescued in *zfhx4* treatment.

1006 (K) Quantification of CtA and glia length parameters in (J). Length index

1007 normalized to individual head length, with each dot representing one embryo.

1008 Data are presented in mean ± SEM; unpaired Student's t test with individual *P*

1009 values mentioned in the figure.

1010 (L) Whole-mount RNA *in situ* hybridization revealed that *Zfhx4* and *Vegfaa*

1011 decreased in CRISPR-mediated *betaPix* F_0 knockout embryos at 36 hpf, which

1012 were rescued by *Zfhx4* mRNA injection. Lateral views with anterior to the left.

1013 Arrows indicate hindbrain regions.

1014 (M) Dot plots of several angiogenesis-associated genes expression in endothelial

1015 cell cluster. Dot size indicates the percentage of cells with gene expression,

1016 and dot color represents the average gene expression level. Individual scale

1017 bars indicated in the figure.

1018

1019 **Figure 7. Schematic diagram on the function of glial *betaPix* in zebrafish**

1020 **vascular integrity development of the hindbrain.** *betaPix* is enriched in glia and

1021 regulates the PAK1-Stathmin axis on microtublin stabilization, thus fine-tuning glial

1022 cell migration and their interactions with vanscular endothelial cells; and in paralelle,

1023 betaPix may also regulate Zfhx3/4-Vegfaa signaling in glia, which then modulates

1024 angiogenesis during cerebral vessel development and maturation. Deletion of *betaPix*

1025 affects glial cell migration and interaction with cerebral endothelial cells. MT,

1026 Microtubule.

1027

1028 **Figure S1. Generation of *betaPix* conditional trap (*betaPix*^{ct}) allele by an**

1029 **HDR-mediated knock-in method.**

1030 (A) Sanger sequencing results of the original pZwitch (+3) and the modified

1031 vector with glycine-serine-glycine spacer (GSG) in front of the 2A peptide.

1032 (B) Sanger sequencing results of the genomic PCR products at both junction sites

1033 from the *betaPix*^{ct} F_1 offspring showing the correct knock-in in the betaPix

1034 locus.

1035 (C) The screening process for *betaPix*^{ct} knock-in zebrafish showing about 1%

1036 efficiency with correct homologous recombinations.

1037 (D) Representative stereomicroscopy images of *o*-dianisidine staining in *bbh*^{fn40a}

1038 embryos at 48 hpf. Lateral view, anterior to the left in left panel; Dorsal view,

1039 anterior to the top in right panel.

1040 (E) Quantification of hemorrhagic parameters in (D). Left panel showing

1041 hemorrhage percentages, with independent experiment as dot. Right panel

1042 showing hemorrhage areas with each dot representing one embryo. #

1043 represents the numbers of embryos scored for each analysis, three or more

1044 individual experiments conducted. Data are presented in mean ± SEM;

1045 unpaired Student's t test with individual *P* values mentioned in the figure.

1046 (F) 3D reconstruction of the *betaPix* expression (magenta) in *betaPix*$^{ct/+}$ brains of

1047 embryos microinjected with PBS or *Cre* mRNA at 24 hpf, 48 hpf, 72 hpf and

1048 144 hpf. Cre-induced *RFP* expression indicates successful inversion of gene

1049 trap system (arrows). Dorsal view, anterior to the top.

1050 (G) 3D reconstruction of the *neurod1* transgenic expression (green) and *betaPix*

1051 expression (magenta) in *betaPix*$^{ct/+}$ brains of embryos microinjected with PBS

1052 or *Cre* mRNA at 24 hpf, 48 hpf, 72 hpf and 144 hpf. Cre-induced *RFP*

1053 expression indicates successful inversion of gene trap system (arrows),

1054 marking strong *betaPix* expression at the midbrain hindbrain boundary (MHB),

1055 and milder expression at hindbrain at early stages. At 144 hpf, *betaPix*

1056 expresses ubiquitously in the brain, outlining the cerebellum (arrowheads).

1057 Dorsal view, anterior to the top. Individual scale bars indicated in the figure.

1058

1059 **Figure S2. *betaPix*$^{m/m}$ mutant had brain hemorrhages, central arteries defects,**

1060 **and abnormal glial structure.**

1061 (A) 3D reconstruction of the vasculature (green) in the heads with lateral view,

1062 anterior to left. Endogenous *betaPix* expression (magenta) only shown in Cre

1063 mRNA-injected mutant embryos. Box areas are shown in higher

1064 magnifications of vasculatures at the right panels. Central arteries (CtA)

1065 defects (white arrows) were evident in *betaPix*$^{m/m}$ embryos at 48 hpf. Arrow

1066 lines indicating the CtA length.

1067 (B) Quantification of CtA parameters in (A). Left panel showing the average CtA

1068 length, and right panel showing the CtA length index normalized to individual

1069 head length, with each dot representing one embryo. Data are presented in

1070 mean ± SEM; unpaired Student's t test with individual *P* values mentioned in

1071 the figure.

1072 (C) 3D reconstruction of the glia structure. Box areas showing higher

1073 magnifications of glia at the right panels. D, dorsal; V, ventral. Arrow lines

1074 indicating the glia length. Individual scale bars indicated in the figure.

1075

1076 **Figure S3. CRISPR-mediated *betaPix* F_0 knockouts had similar phenotypes as**

1077 ***betaPix*$^{m/m}$ mutants.**

1078 (A) Schematic diagram illustrates guide RNA sites for CRISPR-mediated *betaPix*

1079 F_0 knockout. E, exon.

1080 (B) qRT-PCR revealing that *betaPix* decreased in CRISPR-mediated *betaPix* F_0

1081 knockout embryos compared with wild-type siblings at 48 hpf. Each dot

1082 represents one embryo. Data are presented in mean ± SEM; unpaired

1083 Student's t test with individual *P* values mentioned in the figure.

1084 (C) Maximal intensity projection of the glial structure of the hindbrains in siblings

1085 and CRISPR-mediated *betaPix* F_0 knockouts at 48 hpf, lateral view with

1086 anterior to left.

1087 (D) Whole-mount RNA *in situ* hybridization revealing up-regulated *nestin* and

1088 down-regulated *pax2a* expression in CRISPR-mediated *betaPix* F_0 knockout

1089 embryos at 48 hpf. Dorsal view with the anterior to the left.

1090 (E) Quantification of hemorrhagic parameters of siblings and CRISPR-mediated

1091 *betaPix* F_0 knockout embryos at 48 hpf. Left panel showing hemorrhage

1092 percentages, with independent experiment as dot. Right panel showing

1093 hemorrhage areas with each dot representing one embryo. # represents the

1094 numbers of embryos scored for each analysis, three or more individual

1095 experiments conducted. Data are presented in mean ± SEM; unpaired

1096 Student's t test with individual *P* values mentioned in the figure.

1097 (F) Quantification of CtA parameters of siblings and CRISPR-mediated *betaPix*

1098 F_0 knockout embryos at 48 hpf. Left panel showing average CtA length, and

1099 right panel showing CtA length index normalized to individual head length,

1100 with each dot representing one embryo. Data are presented in mean ± SEM;

1101 unpaired Student's t test with individual *P* values mentioned in the figure.

1102 (G) Quantification of glial parameters of siblings and CRISPR-mediated *betaPix*

1103 F_0 knockout embryos at 48 hpf. Left panel showing average glia length, and

1104 right panel showing glia length index normalized to individual head length,

1105 with each dot representing one embryo. Data are presented in mean ± SEM;

1106 unpaired Student's t test with individual *P* values mentioned in the

1107 figure. Individual scale bars indicated in the figure.

1108

1109 **Figure S4. Generating glial-specific *betaPix* knockout zebrafish.**

1110 (A) Schematic diagram illustrates establishment of glial-specific *betaPix* knockout

1111 zebrafish.

1112 (B) 3D reconstruction of the heads at 48 hpf with lateral view, anterior to

1113 left. Glial-specific *Cre* expression (green) was only shown in *gfap:GFP-Cre*;

1114 $betaPix^{ct/ct}$ mutant embryos, which overlaps with betaPix:RFP expression

1115 (magenta).

1116 (C) Genomic PCR analysis of the $betaPix^{ct}$- or $betaPix^{m}$-unique sequences in

1117 $betaPix^{ct/ct}$ siblings, *gfap:GFP-Cre*; $betaPix^{ct/+}$ heterozygous mutants, and

1118 *gfap:GFP-Cre*; $betaPix^{ct/ct}$ homozygous mutants.

1119 (D) qRT-PCR analysis revealing *Cre* expression in *gfap:GFP*-positive glial

1120 population and *gfap:GFP*-negative non-glial population that were sorted from

1121 *gfap:GFP-Cre*; *betaPix*$^{ct/ct}$ embryos. Each dot represents one embryo. Data are

1122 presented in mean ± SEM; unpaired Student's t test with individual *P* values

1123 mentioned in the figure.

1124 (E) qRT-PCR analysis showing *betaPix, betaPix-RFP* and *alphaPix* expression in

1125 *betaPix*$^{ct/ct}$ control siblings and *gfap:GFP-Cre*; *betaPix*$^{ct/ct}$ mutant embryos at

1126 48 hpf. Each dot represents one embryo. Data are presented in mean ± SEM;

1127 unpaired Student's t test with individual *P* values mentioned in the figure.

1128 (F) Whole-mount RNA *in situ* hybridization revealing that *alphaPix* was

1129 comparable but *betaPix* decreased in *gfap:GFP-Cre*; *betaPix*$^{ct/ct}$ mutants

1130 compared with *betaPix*$^{ct/ct}$ siblings at 48 hpf. Lateral view with anterior to the

1131 left. Individual scale bars indicated in the figure.

1132

1133 **Figure S5. Neither endothelial-, neuronal- nor mural-specific deletion of *betaPix***

1134 **caused brain hemorrhages and abnormal CtA phenotypes.**

1135 (A) Representative stereomicroscopy images of *o*-dianisidine staining in

1136 *betaPix*$^{ct/ct}$, *kdrl:Cre*; *betaPix*$^{ct/ct}$, *huC:GFP-Cre*; *betaPix*$^{ct/ct}$, and

1137 *acta2:GFP-Cre*; *betaPix*$^{ct/ct}$ embryos at 48 hpf.

1138 (B) Quantification of hemorrhage parameters in (A). Up panel showing

1139 hemorrhage percentages, with independent experiment as dot. Down panel

1140 showing hemorrhage areas with each dot representing one embryo. #

1141 represents the numbers of embryos scored for each analysis, three or more

1142 individual experiments conducted. Data are presented in mean ± SEM;

1143 unpaired Student's t test with individual *P* values mentioned in the figure.

1144 (C) 3D reconstruction of the vasculature of *betaPix*$^{ct/ct}$, *kdrl:Cre*; *betaPix*$^{ct/ct}$,

1145 *huC:GFP-Cre*; *betaPix*$^{ct/ct}$, and *acta2:GFP-Cre*; *betaPix*$^{ct/ct}$ embryos at 48 hpf.

1146 Lateral view with anterior to left. Boxed areas of the hindbrains are shown in

1147 higher magnifications at the right panels.

1148 (D) Quantification of CtA parameters in (C). Up panel showing average CtA

1149 length, and down panel showing CtA length index normalized to individual

1150 head length, with each dot representing one embryo. Data are presented in

1151 mean ± SEM; unpaired Student's t test with individual *P* values mentioned in

1152 the figure. Individual scale bars indicated in the figure.

1153

1154 **Figure S6. Glial progenitor sub-cluster of *betaPix* knockouts has**

1155 **down-regulation of s*tathmin* family members and up-regulation of *pak1* gene.**

1156 (A) Dot plot of marker genes expression in each cell type. Dot size indicates the

1157 percentage of cells expressed, and dot color represents the average expression

1158 level. Box area and arrow highlighting *gfap* expressions. Clusters with high

1159 *gfap* levels including neuronal and glial progenitors, hindbrain, ventral

1160 diencephalon, ventral midbrain and floor plate.

1161 (B) UMAP visualization and clustering of cells labeled by cell type across four

1162 sample groups.

1163 (C) UMAP feature plots displaying relative expression levels of selected

1164 transcripts among four sample groups. Cells are colored by expression level.

1165

1166 **Figure S7. CRISPR-mediated *stmn1a/1b/4l* F_0 knockouts have similar but milder**

1167 **phenotypes as *betaPix* knockouts.**

1168 (A) qRT-PCR analysis showing that IPA3 treatment rescued *stmn1a* and *stmn4l*

1169 expression in CRISPR-mediated *betaPix* F_0 knockouts at 48 hpf. Each dot

1170 represents one embryo. Data are presented in mean ± SEM; one-way ANOVA

1171 analysis with Dunnett's test, individual P values mentioned in the figure.

1172 (B) Schematic diagram illustrates 4-guide RNAs mediated F_0 knockout strategy in

1173 the loci of *stmn1a*, *stmn1b* and *stmn4l*.

1174 (C) Whole-mount RNA *in situ* hybridization confirming that *stmn1a, stmn1b* and

1175 *stmn4l* decreased in CRISPR-mediated *stmn1a/1b/4l* F_0 knockouts at 48 hpf.

1176 Dorsal views with anterior to the left.

1177 (D) qRT-PCR analysis confirming that *stmn1a, stmn1b* and *stmn4l* decreased in

1178 mutant embryos of CRISPR-mediated *stmn1a/1b/4l* F_0 knockouts at 48 hpf.

1179 Each dot represents one embryo. Data are presented in mean ± SEM; unpaired

1180 Student's t test with individual *P* values mentioned in the figure.

1181 (E) qRT-PCR analysis confirming that *stmn1a, stmn1b* and *stmn4l* decreased in

1182 the FACS-sorted glia of CRISPR-mediated *stmn1a/1b/4l* F_0 knockouts at 48

1183 hpf. Each dot represents sorted cells from one embryo. Data are presented in

1184 mean ± SEM; unpaired Student's t test with individual *P* values mentioned in

1185 the figure.

1186 (F) Optical sections of glial structure in the hindbrains of siblings and

1187 CRISPR-mediated *stmn1a/1b/4l* F_0 knockouts at 48 hpf. Lateral view with

1188 anterior to the left. Abnormal glial structures with disoriented arrangements

1189 (yellow arrows) in *stmn1a/1b/4l* mutant embryos.

1190 (G) Quantification of average CtA and glial length in Figure 5 (E). Each dot

1191 represents one embryo. Data are presented in mean ± SEM; unpaired

1192 Student's t test with individual *P* values mentioned in the figure.

1193 (H) Whole-mount RNA *in situ* hybridization revealed that *nestin* increased while

1194 *pax2a* decreased in CRISPR-mediated *stmn1a/1b/4l* F_0 knockout embryos at

1195 48 hpf. Dorsal views with anterior to the left.

1196 (I) 3D reconstruction and whole-mount RNA *in situ* hybridization showing that

1197 *gfap:GFP-stmn1b* transgenic overexpression rescued glial defects in bbh^{fn40a};

1198 Tg(*gfap:GFP-stmn1b*) embryos at 48 hpf. Lateral views with anterior to the

1199 left.

1200 (J) Whole-mount RNA *in situ* hybridization showing that *nestin* and *pax2a* were

1201 normally expressed in bbh^{fn40a}; Tg(*gfap:GFP-stmn1b*) embryos at 48 hpf.

1202 Dorsal views with anterior to the left.

1203 (K) Quantification of average CtA and glia length in Figure 5 (I). Each dot

1204 represents one embryo. Data are presented in mean ± SEM; unpaired

1205 Student's t test with individual *P* values mentioned in the figure.

1206 (L) qRT-PCR analysis confirming the efficacy of *betaPix* transgenic

1207 over-expression and *betaPix* siRNA knockdown in U251 cells. Data are

1208 presented in mean ± SEM; one-way ANOVA analysis with Dunnett's test,

1209 individual P values mentioned in the figure.

1210 (M) Representative stereomicroscopy images of A172 cells at 0 and 18 hours

1211 after wounding. *betaPIX* siRNA treatment decreased A172 cell migration,

1212 which were rescued by either *betaPIX* or STMN1 overexpression. The wound

1213 edges are highlighted by dashed lines, with arrow lines indicating the wound

1214 width.

1215 (N) Quantification of wound closures in (M). Data are presented in mean ± SEM;

1216 one-way ANOVA analysis with Dunnett's test. $^{**}P<0.01$ compared to negative

1217 control siRNA and empty vector transfection. $^{\#\#}P<0.01$, $^{\#\#\#}P<0.005$ compared

1218 to *betaPix* knockdown and empty vector transfecti on. Individual scale bars

1219 indicated in the figure.

1220

1221 **Figure S8. *Zfhx3/4* acts downstream of *betaPix* to regulate vascular integrity**

1222 **development.**

1223 (A) Violin plots showing that *Zfhx3* and *Zfhx4* decreased in progenitor sub-cluster

1224 of *betaPix* knockouts.

1225 (B) qRT-PCR analysis revealing that *Zfhx3* and *Zfhx4* decreased in FACS-sorted

1226 glia of *gfap:GFP-Cre*; *betaPix*$^{ct/ct}$ mutants compared with *betaPix*$^{ct/ct}$ siblings

1227 at 48 hpf. Each dot represents the cells sorted from one embryo. Data are

1228 presented in mean ± SEM; unpaired Student's t test with individual *P* values

1229 mentioned in the figure.

1230 (C) Schematic diagram illustrates 4-guide RNAs mediated F_0 knockout strategy in

1231 the *Zfhx3* and *Zfhx4* loci.

1232 (D) Whole-mount RNA *in situ* hybridization confirming *Zfhx3/4* efficiency in

1233 CRISPR-mediated *Zfhx3/4* F_0 knockout embryos at 48 hpf. Arrows indicate

1234 significant reduction of *Zfhx3* and *Zfhx4* levels in hindbrain by *Zfhx3/4* double

1235 knockout.

1236 (E) qRT-PCR analysis revealing that *Zfhx3*, *Zfhx4*, and *Vegfaa* decreased in

1237 CRISPR-mediated *Zfhx3/4* F_0 knockout embryos at 36 hpf. Data are presented

1238 in mean ± SEM; unpaired Student's t test with individual *P* values mentioned

1239 in the figure.

1240 (F) Whole-mount RNA *in situ* hybridization revealing that *nestin* increased in

1241 CRISPR-mediated *Zfhx3/4* F_0 knockout embryos at 36 hpf. Arrows indicate

1242 the hindbrain regions.

1243 (G) qRT-PCR analysis confirming overexpression of *Zfhx4* in CRISPR-mediated

1244 *betaPix* F_0 knockout embryos with *Zfhx4* mRNA injection at 70% epiboly.

1245 Data are presented in mean ± SEM; unpaired Student's t test with individual *P*

1246 values mentioned in the figure.

1247 (H) Representative stereomicroscopy images of erythrocytes stained with

1248 *o*-dianisidine showing that brain hemorrhages (arrows) decreased in bbh^{fn40a}

1249 mutants with *Zfhx4* mRNA injection at 48 hpf. Lateral views with anterior to

1250 the left.

1251 (I) Quantification of hemorrhagic parameters in (H). Left panel showing

1252 hemorrhage percentages, with independent experiment as dot. Right panel

1253 showing hemorrhage areas with each dot representing one embryo. #

1254 represents the numbers of embryos scored for each analysis, three or more

1255 individual experiments conducted. Data are presented in mean ± SEM;

1256 unpaired Student's t test with individual *P* values mentioned in the figure.

1257 Individual scale bars indicated in the figure.

1258 **References**

1259 1. Sheth, K.N. (2022). Spontaneous Intracerebral Hemorrhage. New England Journal of
1260 Medicine *387*, 1589–1596. doi:10.1056/NEJMra2201449.
1261 2. Chiang, P.-T., Tsai, L.-K., and Tsai, H.-H. (9900). New targets in spontaneous intracerebral
1262 hemorrhage. Current Opinion in Neurology.
1263 3. Thangameeran, S.I.M., Pang, C.Y., Lee, C.H., Tsai, S.T., Hu, W.F., and Liew, H.K. (2023).
1264 Experimental animal models and evaluation techniques in intracerebral hemorrhage. Tzu Chi
1265 Med J *35*, 1–10. 10.4103/tcmj.tcmj_119_22.
1266 4. Isogai, S., Horiguchi, M., and Weinstein, B.M. (2001). The vascular anatomy of the
1267 developing zebrafish: an atlas of embryonic and early larval development. Dev Biol *230*,
1268 278–301. 10.1006/dbio.2000.9995.
1269 5. Buchner, D.A., Su, F., Yamaoka, J.S., Kamei, M., Shavit, J.A., Barthel, L.K., McGee, B.,
1270 Amigo, J.D., Kim, S., Hanosh, A.W., et al. (2007). pak2a mutations cause cerebral
1271 hemorrhage in redhead zebrafish. Proceedings of the National Academy of Sciences *104*,
1272 13996–14001. 10.1073/pnas.0700947104.
1273 6. Jin, S.-W., Herzog, W., Santoro, M.M., Mitchell, T.S., Frantsve, J., Jungblut, B., Beis, D.,
1274 Scott, I.C., D'Amico, L.A., Ober, E.A., et al. (2007). A transgene-assisted genetic screen
1275 identifies essential regulators of vascular development in vertebrate embryos. Developmental
1276 Biology *307*, 29–42.
1277 7. Hegarty, J.M., Yang, H., and Chi, N.C. (2013). UBIAD1-mediated vitamin K2 synthesis is
1278 required for vascular endothelial cell survival and development. Development *140*,
1279 1713–1719. 10.1242/dev.093112.
1280 8. Stainier, D.Y., Fouquet, B., Chen, J.N., Warren, K.S., Weinstein, B.M., Meiler, S.E.,
1281 Mohideen, M.A., Neuhauss, S.C., Solnica-Krezel, L., Schier, A.F., et al. (1996). Mutations
1282 affecting the formation and function of the cardiovascular system in the zebrafish embryo.
1283 Development *123*, 285–292.
1284 9. Chen, J.N., van Bebber, F., Goldstein, A.M., Serluca, F.C., Jackson, D., Childs, S., Serbedzija,
1285 G., Warren, K.S., Mably, J.D., Lindahl, P., et al. (2001). Genetic steps to organ laterality in
1286 zebrafish. Comp Funct Genomics *2*, 60–68. 10.1002/cfg.74.
1287 10. Liu, J., Fraser, S.D., Faloon, P.W., Rollins, E.L., Vom Berg, J., Starovic-Subota, O., Laliberte,
1288 A.L., Chen, J.N., Serluca, F.C., and Childs, S.J. (2007). A betaPix Pak2a signaling pathway
1289 regulates cerebral vascular stability in zebrafish. Proc Natl Acad Sci U S A *104*, 13990–13995.
1290 10.1073/pnas.0700825104.
1291 11. Manser, E., Loo, T.-H., Koh, C.-G., Zhao, Z.-S., Chen, X.-Q., Tan, L., Tan, I., Leung, T., and
1292 Lim, L. (1998). PAK Kinases Are Directly Coupled to the PIX Family of Nucleotide
1293 Exchange Factors. Molecular Cell *1*, 183–192.
1294 12. Zhou, W., Li, X., and Premont, R.T. (2016). Expanding functions of GIT Arf
1295 GTPase-activating proteins, PIX Rho guanine nucleotide exchange factors and GIT-PIX
1296 complexes. J Cell Sci *129*, 1963–1974. 10.1242/jcs.179465.
1297 13. Morimoto, K., Tabata, H., Takahashi, R., and Nakajima, K. (2024). Interactions between
1298 neural cells and blood vessels in central nervous system development. Bioessays *46*,
1299 e2300091. 10.1002/bies.202300091.
1300 14. Grinchevskaya, L.R., Salikhova, D.I., Silachev, D.N., and Goldshtein, D.V. (2024). Neural

1301 and Glial Regulation of Angiogenesis in CNS in Ischemic Stroke. Bull Exp Biol Med *177*,
1302 528–533. 10.1007/s10517-024-06219-4.
1303 15. McCarty, J.H. (2009). Cell adhesion and signaling networks in brain neurovascular units. Curr
1304 Opin Hematol *16*, 209–214. 10.1097/MOH.0b013e32832a07eb.
1305 16. McCarty, J.H. (2009). Integrin-mediated regulation of neurovascular development, physiology
1306 and disease. Cell Adh Migr *3*, 211–215. 10.4161/cam.3.2.7767.
1307 17. Liu, J., Zeng, L., Kennedy, R.M., Gruenig, N.M., and Childs, S.J. (2012). βPix plays a dual
1308 role in cerebral vascular stability and angiogenesis, and interacts with integrin αvβ8. Dev Biol
1309 *363*, 95–105. 10.1016/j.ydbio.2011.12.022.
1310 18. Yang, R., Zhang, Y., Huang, D., Luo, X., Zhang, L., Zhu, X., Zhang, X., Liu, Z., Han, J.Y.,
1311 and Xiong, J.W. (2017). Miconazole protects blood vessels from MMP9-dependent rupture
1312 and hemorrhage. Dis Model Mech *10*, 337–348. 10.1242/dmm.027268.
1313 19. Sugimoto, K., Hui, S.P., Sheng, D.Z., and Kikuchi, K. (2017). Dissection of zebrafish shha
1314 function using site-specific targeting with a Cre-dependent genetic switch. Elife *6*.
1315 10.7554/eLife.24635.
1316 20. Ogawa, M., Geng, F.S., Humphreys, D.T., Kristianto, E., Sheng, D.Z., Hui, S.P., Zhang, Y.,
1317 Sugimoto, K., Nakayama, M., Zheng, D., et al. (2021). Krüppel-like factor 1 is a core
1318 cardiomyogenic trigger in zebrafish. Science *372*, 201–205. 10.1126/science.abe2762.
1319 21. Ogawa, M., and Kikuchi, K. (2024). Generation of Conditional Knockout Zebrafish Using an
1320 Invertible Gene-Trap Cassette. Methods Mol Biol *2707*, 205–214.
1321 10.1007/978-1-0716-3401-1_13.
1322 22. Wierson, W.A., Simone, B.W., WareJoncas, Z., Mann, C., Welker, J.M., Kar, B., Emch, M.J.,
1323 Friedberg, I., Gendron, W.A.C., Barry, M.A., et al. (2019). Expanding the CRISPR Toolbox
1324 with ErCas12a in Zebrafish and Human Cells. Crispr j *2*, 417–433. 10.1089/crispr.2019.0026.
1325 23. Wu, R.S., Lam, II, Clay, H., Duong, D.N., Deo, R.C., and Coughlin, S.R. (2018). A Rapid
1326 Method for Directed Gene Knockout for Screening in G0 Zebrafish. Dev Cell *46*, 112–125
1327 e114. 10.1016/j.devcel.2018.06.003.
1328 24. Quiñonez-Silvero, C., Hübner, K., and Herzog, W. (2020). Development of the brain
1329 vasculature and the blood-brain barrier in zebrafish. Dev Biol *457*, 181–190.
1330 10.1016/j.ydbio.2019.03.005.
1331 25. Deacon, S.W., Beeser, A., Fukui, J.A., Rennefahrt, U.E., Myers, C., Chernoff, J., and Peterson,
1332 J.R. (2008). An isoform-selective, small-molecule inhibitor targets the autoregulatory
1333 mechanism of p21-activated kinase. Chem Biol *15*, 322–331.
1334 10.1016/j.chembiol.2008.03.005.
1335 26. Bernardos, R.L., and Raymond, P.A. (2006). GFAP transgenic zebrafish. Gene Expr Patterns
1336 *6*, 1007–1013. 10.1016/j.modgep.2006.04.006.
1337 27. Kim, C.H., Ueshima, E., Muraoka, O., Tanaka, H., Yeo, S.Y., Huh, T.L., and Miki, N. (1996).
1338 Zebrafish elav/HuC homologue as a very early neuronal marker. Neurosci Lett *216*, 109–112.
1339 10.1016/0304-3940(96)13021-4.
1340 28. Raj, B., Wagner, D.E., McKenna, A., Pandey, S., Klein, A.M., Shendure, J., Gagnon, J.A.,
1341 and Schier, A.F. (2018). Simultaneous single-cell profiling of lineages and cell types in the
1342 vertebrate brain. Nature Biotechnology *36*, 442–450. 10.1038/nbt.4103.
1343 29. Raj, B., Farrell, J.A., Liu, J., El Kholtei, J., Carte, A.N., Navajas Acedo, J., Du, L.Y.,
1344 McKenna, A., Relić, Đ., Leslie, J.M., and Schier, A.F. (2020). Emergence of Neuronal

1345 Diversity during Vertebrate Brain Development. Neuron *108*, 1058–1074.e1056.
1346 10.1016/j.neuron.2020.09.023.
1347 30. Farnsworth, D.R., Saunders, L.M., and Miller, A.C. (2020). A single-cell transcriptome atlas
1348 for zebrafish development. Developmental Biology *459*, 100–108.
1349 31. Etienne-Manneville, S. (2013). Microtubules in cell migration. Annu Rev Cell Dev Biol *29*,
1350 471–499. 10.1146/annurev-cellbio-101011-155711.
1351 32. Kwon, Y., Jeon, Y.W., Kwon, M., Cho, Y., Park, D., and Shin, J.E. (2020). βPix-d promotes
1352 tubulin acetylation and neurite outgrowth through a PAK/Stathmin1 signaling pathway. PLoS
1353 One *15*, e0230814. 10.1371/journal.pone.0230814.
1354 33. Omelchenko, T., Rabadan, M.A., Hernandez-Martinez, R., Grego-Bessa, J., Anderson, K.V.,
1355 and Hall, A. (2014). beta-Pix directs collective migration of anterior visceral endoderm cells
1356 in the early mouse embryo. Genes Dev *28*, 2764–2777. 10.1101/gad.251371.114.
1357 34. Hsu, R.M., Hsieh, Y.J., Yang, T.H., Chiang, Y.C., Kan, C.Y., Lin, Y.T., Chen, J.T., and Yu,
1358 J.S. (2014). Binding of the extreme carboxyl-terminus of PAK-interacting exchange factor β
1359 (βPIX) to myosin 18A (MYO18A) is required for epithelial cell migration. Biochim Biophys
1360 Acta *1843*, 2513–2527. 10.1016/j.bbamcr.2014.06.023.
1361 35. López Tobón, A., Suresh, M., Jin, J., Vitriolo, A., Pietralla, T., Tedford, K., Bossenz, M.,
1362 Mahnken, K., Kiefer, F., Testa, G., et al. (2018). The guanine nucleotide exchange factor
1363 Arhgef7/βPix promotes axon formation upstream of TC10. Scientific Reports *8*, 8811.
1364 10.1038/s41598-018-27081-1.
1365 36. Cheng, K., Chahdi, A., Larabee, S.M., Tolaymat, M., Sundel, M.H., Drachenberg, C.B., Zhan,
1366 M., Hu, S., Said, A.H., Shang, A.C., et al. (2023). Muscarinic receptor agonist-induced βPix
1367 binding to β-catenin promotes colon neoplasia. Sci Rep *13*, 16920.
1368 10.1038/s41598-023-44158-8.
1369 37. Connor, K., Murray, D.W., Jarzabek, M.A., Tran, N.L., White, K., Dicker, P., Sweeney, K.J.,
1370 O'Halloran, P.J., MacCarthy, B., Shiels, L.P., et al. (2020). Targeting the RhoGEF
1371 βPIX/COOL-1 in Glioblastoma: Proof of Concept Studies. Cancers (Basel) *12*.
1372 10.3390/cancers12123531.
1373 38. Ward, J.D., Ha, J.H., Jayaraman, M., and Dhanasekaran, D.N. (2015). LPA-mediated
1374 migration of ovarian cancer cells involves translocalization of Gαi2 to invadopodia and
1375 association with Src and β-pix. Cancer Lett *356*, 382–391. 10.1016/j.canlet.2014.09.030.
1376 39. Bussmann, J., Wolfe, S.A., and Siekmann, A.F. (2011). Arterial-venous network formation
1377 during brain vascularization involves hemodynamic regulation of chemokine signaling.
1378 Development *138*, 1717–1726. 10.1242/dev.059881.
1379 40. Eubelen, M., Bostaille, N., Cabochette, P., Gauquier, A., Tebabi, P., Dumitru, A.C., Koehler,
1380 M., Gut, P., Alsteens, D., Stainier, D.Y.R., et al. (2018). A molecular mechanism for Wnt
1381 ligand-specific signaling. Science *361*. 10.1126/science.aat1178.
1382 41. Pitulescu, M.E., and Adams, R.H. (2014). Regulation of signaling interactions and receptor
1383 endocytosis in growing blood vessels. Cell Adh Migr *8*, 366–377.
1384 10.4161/19336918.2014.970010.
1385 42. Wang, J., Chen, Y., Zeng, Z., Feng, R., Wang, Q., Zhang, Q., Sun, K., Chen, A.F., Lu, Y., and
1386 Yu, Y. (2021). HMGA2 contributes to vascular development and sprouting angiogenesis by
1387 promoting IGFBP2 production. Exp Cell Res *408*, 112831. 10.1016/j.yexcr.2021.112831.
1388 43. Fu, C., An, N., Liu, J., A, J., Zhang, B., Liu, M., Zhang, Z., Fu, L., Tian, X., Wang, D., and

1389 Dong, J.T. (2020). The transcription factor ZFHX3 is crucial for the angiogenic function of
1390 hypoxia-inducible factor 1α in liver cancer cells. J Biol Chem *295*, 7060–7074.
1391 10.1074/jbc.RA119.012131.
1392 44. Gudbjartsson, D.F., Holm, H., Gretarsdottir, S., Thorleifsson, G., Walters, G.B., Thorgeirsson,
1393 G., Gulcher, J., Mathiesen, E.B., Njølstad, I., Nyrnes, A., et al. (2009). A sequence variant in
1394 ZFHX3 on 16q22 associates with atrial fibrillation and ischemic stroke. Nat Genet *41*,
1395 876–878. 10.1038/ng.417.
1396 45. Soriano-Tárraga, C., Lazcano, U., Giralt-Steinhauer, E., Avellaneda-Gómez, C., Ois, Á.,
1397 Rodríguez-Campello, A., Cuadrado-Godia, E., Gómez-González, A., Fernández-Sanlés, A.,
1398 Elosua, R., et al. (2020). Identification of 20 novel loci associated with ischaemic stroke.
1399 Epigenome-wide association study. Epigenetics *15*, 988–997.
1400 10.1080/15592294.2020.1746507.
1401 46. Malik, R., Traylor, M., Pulit, S.L., Bevan, S., Hopewell, J.C., Holliday, E.G., Zhao, W.,
1402 Abrantes, P., Amouyel, P., Attia, J.R., et al. (2016). Low-frequency and common genetic
1403 variation in ischemic stroke: The METASTROKE collaboration. Neurology *86*, 1217–1226.
1404 10.1212/wnl.0000000000002528.
1405 47. Kalvaitytė, M., and Balciunas, D. (2022). Conditional mutagenesis strategies in zebrafish.
1406 Trends Genet *38*, 856–868. 10.1016/j.tig.2022.04.007.
1407 48. Obermeier, B., Daneman, R., and Ransohoff, R.M. (2013). Development, maintenance and
1408 disruption of the blood-brain barrier. Nat Med *19*, 1584–1596. 10.1038/nm.3407.
1409 49. Langen, U.H., Ayloo, S., and Gu, C. (2019). Development and Cell Biology of the
1410 Blood-Brain Barrier. Annu Rev Cell Dev Biol *35*, 591–613.
1411 10.1146/annurev-cellbio-100617-062608.
1412 50. Fleming, A., Diekmann, H., and Goldsmith, P. (2013). Functional characterisation of the
1413 maturation of the blood-brain barrier in larval zebrafish. PLoS One *8*, e77548.
1414 10.1371/journal.pone.0077548.
1415 51. Xie, J., Farage, E., Sugimoto, M., and Anand-Apte, B. (2010). A novel transgenic zebrafish
1416 model for blood-brain and blood-retinal barrier development. BMC Dev Biol *10*, 76.
1417 10.1186/1471-213x-10-76.
1418 52. Stewart, P.A., and Wiley, M.J. (1981). Developing nervous tissue induces formation of
1419 blood-brain barrier characteristics in invading endothelial cells: a study using quail--chick
1420 transplantation chimeras. Dev Biol *84*, 183–192. 10.1016/0012-1606(81)90382-1.
1421 53. Daneman, R., Agalliu, D., Zhou, L., Kuhnert, F., Kuo, C.J., and Barres, B.A. (2009).
1422 Wnt/beta-catenin signaling is required for CNS, but not non-CNS, angiogenesis. Proc Natl
1423 Acad Sci U S A *106*, 641–646. 10.1073/pnas.0805165106.
1424 54. Kuhnert, F., Mancuso, M.R., Shamloo, A., Wang, H.T., Choksi, V., Florek, M., Su, H.,
1425 Fruttiger, M., Young, W.L., Heilshorn, S.C., and Kuo, C.J. (2010). Essential regulation of
1426 CNS angiogenesis by the orphan G protein-coupled receptor GPR124. Science *330*, 985–989.
1427 10.1126/science.1196554.
1428 55. Cullen, M., Elzarrad, M.K., Seaman, S., Zudaire, E., Stevens, J., Yang, M.Y., Li, X.,
1429 Chaudhary, A., Xu, L., Hilton, M.B., et al. (2011). GPR124, an orphan G protein-coupled
1430 receptor, is required for CNS-specific vascularization and establishment of the blood-brain
1431 barrier. Proc Natl Acad Sci U S A *108*, 5759–5764. 10.1073/pnas.1017192108.
1432 56. Zhou, Y., and Nathans, J. (2014). Gpr124 controls CNS angiogenesis and blood-brain barrier

1433 integrity by promoting ligand-specific canonical wnt signaling. Dev Cell *31*, 248–256.
1434 10.1016/j.devcel.2014.08.018.
1435 57. Thomas, M., and Augustin, H.G. (2009). The role of the Angiopoietins in vascular
1436 morphogenesis. Angiogenesis *12*, 125–137. 10.1007/s10456-009-9147-3.
1437 58. Nico, B., Frigeri, A., Nicchia, G.P., Quondamatteo, F., Herken, R., Errede, M., Ribatti, D.,
1438 Svelto, M., and Roncali, L. (2001). Role of aquaporin-4 water channel in the development and
1439 integrity of the blood-brain barrier. J Cell Sci *114*, 1297–1307. 10.1242/jcs.114.7.1297.
1440 59. Nicchia, G.P., Nico, B., Camassa, L.M., Mola, M.G., Loh, N., Dermietzel, R., Spray, D.C.,
1441 Svelto, M., and Frigeri, A. (2004). The role of aquaporin-4 in the blood-brain barrier
1442 development and integrity: studies in animal and cell culture models. Neuroscience *129*,
1443 935–945. 10.1016/j.neuroscience.2004.07.055.
1444 60. Hartfuss, E., Galli, R., Heins, N., and Götz, M. (2001). Characterization of CNS precursor
1445 subtypes and radial glia. Dev Biol *229*, 15–30. 10.1006/dbio.2000.9962.
1446 61. Malatesta, P., Appolloni, I., and Calzolari, F. (2008). Radial glia and neural stem cells. Cell
1447 Tissue Res *331*, 165–178. 10.1007/s00441-007-0481-8.
1448 62. Qian, X., Shen, Q., Goderie, S.K., He, W., Capela, A., Davis, A.A., and Temple, S. (2000).
1449 Timing of CNS cell generation: a programmed sequence of neuron and glial cell production
1450 from isolated murine cortical stem cells. Neuron *28*, 69–80. 10.1016/s0896-6273(00)00086-6.
1451 63. Price, J., Williams, B.P., and Götz, M. (1995). The generation of cellular diversity in the
1452 cerebral cortex. Ciba Found Symp *193*, 71–84; discussion 117–126.
1453 10.1002/9780470514795.ch4.
1454 64. Grupp, L., Wolburg, H., and Mack, A.F. (2010). Astroglial structures in the zebrafish brain. J
1455 Comp Neurol *518*, 4277–4287. 10.1002/cne.22481.
1456 65. Chen, J., Poskanzer, K.E., Freeman, M.R., and Monk, K.R. (2020). Live-imaging of astrocyte
1457 morphogenesis and function in zebrafish neural circuits. Nat Neurosci *23*, 1297–1306.
1458 10.1038/s41593-020-0703-x.
1459 66. Johnson, K., Barragan, J., Bashiruddin, S., Smith, C.J., Tyrrell, C., Parsons, M.J., Doris, R.,
1460 Kucenas, S., Downes, G.B., Velez, C.M., et al. (2016). Gfap-positive radial glial cells are an
1461 essential progenitor population for later-born neurons and glia in the zebrafish spinal cord.
1462 Glia *64*, 1170–1189. 10.1002/glia.22990.
1463 67. Umans, R.A., Pollock, C., Mills, W.A., 3rd, Clark, K.C., Pan, Y.A., and Sontheimer, H.
1464 (2021). Using Zebrafish to Elucidate Glial-Vascular Interactions During CNS Development.
1465 Front Cell Dev Biol *9*, 654338. 10.3389/fcell.2021.654338.
1466 68. Matsuoka, R.L., Rossi, A., Stone, O.A., and Stainier, D.Y.R. (2017). CNS-resident
1467 progenitors direct the vascularization of neighboring tissues. Proc Natl Acad Sci U S A *114*,
1468 10137–10142. 10.1073/pnas.1619300114.
1469 69. Alvarez, J.I., Dodelet-Devillers, A., Kebir, H., Ifergan, I., Fabre, P.J., Terouz, S., Sabbagh, M.,
1470 Wosik, K., Bourbonnière, L., Bernard, M., et al. (2011). The Hedgehog pathway promotes
1471 blood-brain barrier integrity and CNS immune quiescence. Science *334*, 1727–1731.
1472 10.1126/science.1206936.
1473 70. Brilha, S., Ong, C.W.M., Weksler, B., Romero, N., Couraud, P.O., and Friedland, J.S. (2017).
1474 Matrix metalloproteinase-9 activity and a downregulated Hedgehog pathway impair
1475 blood-brain barrier function in an in vitro model of CNS tuberculosis. Sci Rep *7*, 16031.
1476 10.1038/s41598-017-16250-3.

1477 71. Shi, T., Yue, S., Xie, C., Li, X., Yang, D., Hu, L., Zhong, Y., Zhang, Y., and Liu, W. (2024).
1478 MMP-2-mediated Scube2 degradation promotes blood-brain barrier disruption by blocking the
1479 interaction between astrocytes and endothelial cells via inhibiting Sonic hedgehog pathway
1480 during early cerebral ischemia. J Neurochem *168*, 1877–1894. 10.1111/jnc.16021.
1481 72. Xing, G., Zhao, T., Zhang, X., Li, H., Li, X., Cui, P., Li, M., Li, D., Zhang, N., and Jiang, W.
1482 (2020). Astrocytic Sonic Hedgehog Alleviates Intracerebral Hemorrhagic Brain Injury via
1483 Modulation of Blood-Brain Barrier Integrity. Front Cell Neurosci *14*, 575690.
1484 10.3389/fncel.2020.575690.
1485 73. Lawson, N.D., Vogel, A.M., and Weinstein, B.M. (2002). sonic hedgehog and vascular
1486 endothelial growth factor act upstream of the Notch pathway during arterial endothelial
1487 differentiation. Dev Cell *3*, 127–136. 10.1016/s1534-5807(02)00198-3.
1488 74. Mannan, A., Dhiamn, S., Garg, N., and Singh, T.G. (2023). Pharmacological modulation of
1489 Sonic Hedgehog signaling pathways in Angiogenesis: A mechanistic perspective. Dev Biol
1490 *504*, 58–74. 10.1016/j.ydbio.2023.09.009.
1491 75. Yan, J., Manaenko, A., Chen, S., Klebe, D., Ma, Q., Caner, B., Fujii, M., Zhou, C., and Zhang,
1492 J.H. (2013). Role of SCH79797 in maintaining vascular integrity in rat model of subarachnoid
1493 hemorrhage. Stroke *44*, 1410–1417. 10.1161/strokeaha.113.678474.
1494 76. Jagadeeshan, S., Sagayaraj, R.V., Paneerselvan, N., Ghouse, S.S., and Malathi, R. (2017).
1495 Toxicity and anti-angiogenicity evaluation of Pak1 inhibitor IPA-3 using zebrafish embryo
1496 model. Cell Biol Toxicol *33*, 41–56. 10.1007/s10565-016-9358-5.
1497 77. Zou, J., Li, W.Q., Li, Q., Li, X.Q., Zhang, J.T., Liu, G.Q., Chen, J., Qiu, X.X., Tian, F.J.,
1498 Wang, Z.Z., et al. (2011). Two functional microRNA-126s repress a novel target gene
1499 p21-activated kinase 1 to regulate vascular integrity in zebrafish. Circ Res *108*, 201–209.
1500 10.1161/circresaha.110.225045.
1501 78. Braverman, R., Bhattacharya, B., Feuerstein, N., and Cooper, H.L. (1986). Identification and
1502 characterization of the nonphosphorylated precursor of pp17, a phosphoprotein associated
1503 with phorbol ester induction of growth arrest and monocytic differentiation in HL-60
1504 promyelocytic leukemia cells. J Biol Chem *261*, 14342–14348.
1505 79. Luo, X.N., Mookerjee, B., Ferrari, A., Mistry, S., and Atweh, G.F. (1994). Regulation of
1506 phosphoprotein p18 in leukemic cells. Cell cycle regulated phosphorylation by p34cdc2
1507 kinase. J Biol Chem *269*, 10312–10318.
1508 80. Curmi, P.A., Noguès, C., Lachkar, S., Carelle, N., Gonthier, M.P., Sobel, A., Lidereau, R., and
1509 Bièche, I. (2000). Overexpression of stathmin in breast carcinomas points out to highly
1510 proliferative tumours. Br J Cancer *82*, 142–150. 10.1054/bjoc.1999.0891.
1511 81. Price, D.K., Ball, J.R., Bahrani-Mostafavi, Z., Vachris, J.C., Kaufman, J.S., Naumann, R.W.,
1512 Higgins, R.V., and Hall, J.B. (2000). The phosphoprotein Op18/stathmin is differentially
1513 expressed in ovarian cancer. Cancer Invest *18*, 722–730. 10.3109/07357900009012204.
1514 82. Liedtke, W., Leman, E.E., Fyffe, R.E., Raine, C.S., and Schubart, U.K. (2002).
1515 Stathmin-deficient mice develop an age-dependent axonopathy of the central and peripheral
1516 nervous systems. Am J Pathol *160*, 469–480. 10.1016/s0002-9440(10)64866-3.
1517 83. Belmont, L.D., and Mitchison, T.J. (1996). Identification of a protein that interacts with
1518 tubulin dimers and increases the catastrophe rate of microtubules. Cell *84*, 623–631.
1519 10.1016/s0092-8674(00)81037-5.
1520 84. Liu, A., Muggironi, M., Marin-Husstege, M., and Casaccia-Bonnefil, P. (2003).

1521 Oligodendrocyte process outgrowth in vitro is modulated by epigenetic regulation of
1522 cytoskeletal severing proteins. Glia *44*, 264–274. 10.1002/glia.10290.
1523 85. Carretero-Rodriguez, L., Guðjónsdóttir, R., Poparic, I., Reilly, M.L., Chol, M., Bianco, I.H.,
1524 Chiapello, M., Feret, R., Deery, M.J., and Guthrie, S. (2021). The Rac-GAP alpha2-Chimaerin
1525 Signals via CRMP2 and Stathmins in the Development of the Ocular Motor System. J
1526 Neurosci *41*, 6652–6672. 10.1523/jneurosci.0983-19.2021.
1527 86. Lin, M.J., and Lee, S.J. (2016). Stathmin-like 4 is critical for the maintenance of neural
1528 progenitor cells in dorsal midbrain of zebrafish larvae. Sci Rep *6*, 36188. 10.1038/srep36188.
1529 87. Jing, Y., Luo, Y., Li, L., Liu, M., and Liu, J.X. (2024). Deficiency of copper responsive gene
1530 stmn4 induces retinal developmental defects. Cell Biol Toxicol *40*, 2.
1531 10.1007/s10565-024-09847-8.
1532 88. Kim, T.S., Kawaguchi, M., Suzuki, M., Jung, C.G., Asai, K., Shibamoto, Y., Lavin, M.F.,
1533 Khanna, K.K., and Miura, Y. (2010). The ZFHX3 (ATBF1) transcription factor induces
1534 PDGFRB, which activates ATM in the cytoplasm to protect cerebellar neurons from oxidative
1535 stress. Dis Model Mech *3*, 752–762. 10.1242/dmm.004689.
1536 89. Gonzalez, G.A., and Montminy, M.R. (1989). Cyclic AMP stimulates somatostatin gene
1537 transcription by phosphorylation of CREB at serine 133. Cell *59*, 675–680.
1538 10.1016/0092-8674(89)90013-5.
1539 90. Kim, J., and Kaang, B.K. (2022). Cyclic AMP response element-binding protein (CREB)
1540 transcription factor in astrocytic synaptic communication. Front Synaptic Neurosci *14*,
1541 1059918. 10.3389/fnsyn.2022.1059918.
1542 91. Shaywitz, A.J., and Greenberg, M.E. (1999). CREB: a stimulus-induced transcription factor
1543 activated by a diverse array of extracellular signals. Annu Rev Biochem *68*, 821–861.
1544 10.1146/annurev.biochem.68.1.821.
1545 92. Chung, J.H., Kim, D.H., Kim, Y.S., Son, B.S., Kim, D., Hwang, C., Shin, D., Noh, S.G., Han,
1546 J.H., Kim, D.K., et al. (2018). Upregulation of P21-Activated Kinase 1 (PAK1)/CREB Axis in
1547 Squamous Non-Small Cell Lung Carcinoma. Cell Physiol Biochem *50*, 304–316.
1548 10.1159/000494007.
1549 93. Argaw, A.T., Asp, L., Zhang, J., Navrazhina, K., Pham, T., Mariani, J.N., Mahase, S., Dutta,
1550 D.J., Seto, J., Kramer, E.G., et al. (2012). Astrocyte-derived VEGF-A drives blood-brain
1551 barrier disruption in CNS inflammatory disease. J Clin Invest *122*, 2454–2468.
1552 10.1172/jci60842.
1553 94. Chapouly, C., Tadesse Argaw, A., Horng, S., Castro, K., Zhang, J., Asp, L., Loo, H., Laitman,
1554 B.M., Mariani, J.N., Straus Farber, R., et al. (2015). Astrocytic TYMP and VEGFA drive
1555 blood-brain barrier opening in inflammatory central nervous system lesions. Brain *138*,
1556 1548–1567. 10.1093/brain/awv077.
1557 95. Matsumoto, T., and Mugishima, H. (2006). Signal transduction via vascular endothelial
1558 growth factor (VEGF) receptors and their roles in atherogenesis. J Atheroscler Thromb *13*,
1559 130–135. 10.5551/jat.13.130.
1560 96. Jakobsson, L., Franco, C.A., Bentley, K., Collins, R.T., Ponsioen, B., Aspalter, I.M., Rosewell,
1561 I., Busse, M., Thurston, G., Medvinsky, A., et al. (2010). Endothelial cells dynamically
1562 compete for the tip cell position during angiogenic sprouting. Nature Cell Biology *12*,
1563 943–953. 10.1038/ncb2103.
1564 97. Liu, Z.J., Shirakawa, T., Li, Y., Soma, A., Oka, M., Dotto, G.P., Fairman, R.M., Velazquez,

1565 O.C., and Herlyn, M. (2003). Regulation of Notch1 and Dll4 by vascular endothelial growth
1566 factor in arterial endothelial cells: implications for modulating arteriogenesis and angiogenesis.
1567 Mol Cell Biol *23*, 14–25. 10.1128/mcb.23.1.14-25.2003.
1568 98. Olsson, A.K., Dimberg, A., Kreuger, J., and Claesson-Welsh, L. (2006). VEGF receptor
1569 signalling - in control of vascular function. Nat Rev Mol Cell Biol *7*, 359–371.
1570 10.1038/nrm1911.
1571 99. Xu, L., Nirwane, A., and Yao, Y. (2019). Basement membrane and blood-brain barrier. Stroke
1572 Vasc Neurol *4*, 78–82. 10.1136/svn-2018-000198.
1573 100. Jeanne, M., Jorgensen, J., and Gould, D.B. (2015). Molecular and Genetic Analyses of
1574 Collagen Type IV Mutant Mouse Models of Spontaneous Intracerebral Hemorrhage Identify
1575 Mechanisms for Stroke Prevention. Circulation *131*, 1555–1565.
1576 10.1161/circulationaha.114.013395.
1577 101. Halder, S.K., Sapkota, A., and Milner, R. (2022). The impact of genetic manipulation of
1578 laminin and integrins at the blood-brain barrier. Fluids Barriers CNS *19*, 50.
1579 10.1186/s12987-022-00346-8.
1580 102. Yao, Y., Chen, Z.L., Norris, E.H., and Strickland, S. (2014). Astrocytic laminin regulates
1581 pericyte differentiation and maintains blood brain barrier integrity. Nat Commun *5*, 3413.
1582 10.1038/ncomms4413.
1583 103. Milner, R., and Campbell, I.L. (2002). Developmental regulation of beta1 integrins during
1584 angiogenesis in the central nervous system. Mol Cell Neurosci *20*, 616–626.
1585 10.1006/mcne.2002.1151.
1586 104. Nishimura, S.L., Boylen, K.P., Einheber, S., Milner, T.A., Ramos, D.M., and Pytela, R.
1587 (1998). Synaptic and glial localization of the integrin alphavbeta8 in mouse and rat brain.
1588 Brain Res *791*, 271–282. 10.1016/s0006-8993(98)00118-8.
1589 105. McCarty, J.H., Lacy-Hulbert, A., Charest, A., Bronson, R.T., Crowley, D., Housman, D.,
1590 Savill, J., Roes, J., and Hynes, R.O. (2005). Selective ablation of alphav integrins in the
1591 central nervous system leads to cerebral hemorrhage, seizures, axonal degeneration and
1592 premature death. Development *132*, 165–176. 10.1242/dev.01551.
1593 106. Beis, D., Bartman, T., Jin, S.W., Scott, I.C., D'Amico, L.A., Ober, E.A., Verkade, H., Frantsve,
1594 J., Field, H.A., Wehman, A., et al. (2005). Genetic and cellular analyses of zebrafish
1595 atrioventricular cushion and valve development. Development *132*, 4193–4204.
1596 10.1242/dev.01970.
1597 107. Jin, S.W., Beis, D., Mitchell, T., Chen, J.N., and Stainier, D.Y. (2005). Cellular and molecular
1598 analyses of vascular tube and lumen formation in zebrafish. Development *132*, 5199–5209.
1599 10.1242/dev.02087.
1600 108. Jeon, T.Y., Han, M.E., Lee, Y.W., Lee, Y.S., Kim, G.H., Song, G.A., Hur, G.Y., Kim, J.Y.,
1601 Kim, H.J., Yoon, S., et al. (2010). Overexpression of stathmin1 in the diffuse type of gastric
1602 cancer and its roles in proliferation and migration of gastric cancer cells. Br J Cancer *102*,
1603 710–718. 10.1038/sj.bjc.6605537.
1604 109. Chang, N., Sun, C., Gao, L., Zhu, D., Xu, X., Zhu, X., Xiong, J.W., and Xi, J.J. (2013).
1605 Genome editing with RNA-guided Cas9 nuclease in zebrafish embryos. Cell Res *23*, 465–472.
1606 10.1038/cr.2013.45.
1607 110. Jao, L.-E., Wente, S.R., and Chen, W. (2013). Efficient multiplex biallelic zebrafish genome
1608 editing using a CRISPR nuclease system. Proceedings of the National Academy of Sciences

110, 13904–13909. doi:10.1073/pnas.1308335110.

111. Kawakami, K. (2004). Transgenesis and gene trap methods in zebrafish by using the Tol2 transposable element. Methods Cell Biol *77*, 201–222. 10.1016/s0091-679x(04)77011-9.

112. Lei, L., Yan, S.Y., Yang, R., Chen, J.Y., Li, Y., Bu, Y., Chang, N., Zhou, Q., Zhu, X., Li, C.Y., and Xiong, J.W. (2017). Spliceosomal protein eftud2 mutation leads to p53-dependent apoptosis in zebrafish neural progenitors. Nucleic Acids Res *45*, 3422–3436. 10.1093/nar/gkw1043.

113. Pang, M., Bai, L., Zong, W., Wang, X., Bu, Y., Xiong, C., Zheng, J., Li, J., Gao, W., Feng, Z., et al. (2020). Light-sheet fluorescence imaging charts the gastrula origin of vascular endothelial cells in early zebrafish embryos. Cell Discovery *6*, 74. 10.1038/s41421-020-00204-7.

Figure 1

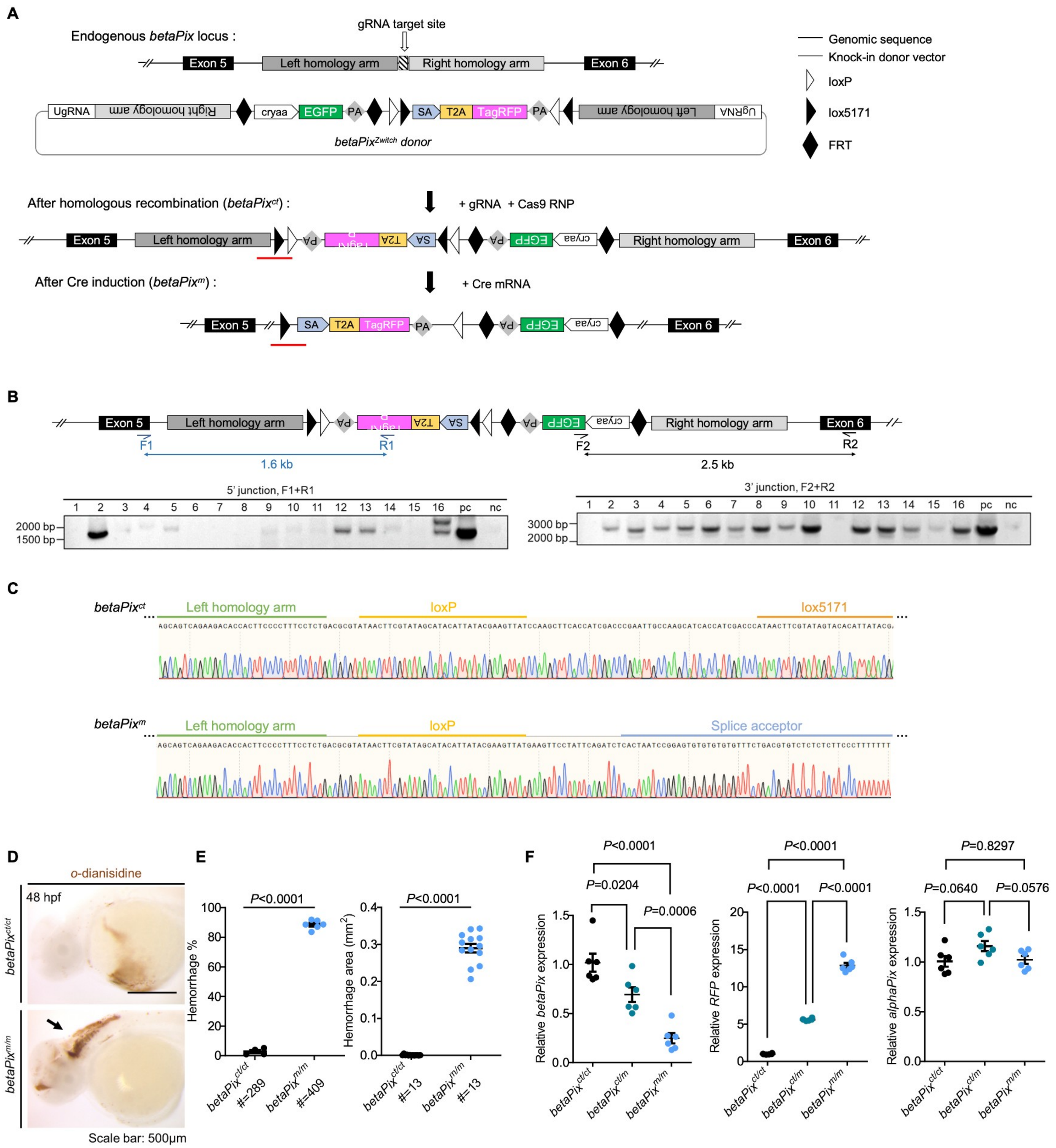
A
Endogenous betaPix locus :
gRNA target site
Exon 5
Left homology arm
Right homology arm
Exon 6
Genomic sequence
Knock-in donor vector
loxP
lox5171
FRT
UgRNA
Right homology arm
cryaa
EGFP
PA
SA
T2A
TagRFP
PA
Left homology arm
UgRNA
betaPix^Zwitch donor
After homologous recombination (betaPix^ct) :
+ gRNA + Cas9 RNP
After Cre induction (betaPix^m) :
+ Cre mRNA
B
F1
R1
1.6 kb
F2
R2
2.5 kb
5' junction, F1+R1
3' junction, F2+R2
2000 bp
1500 bp
3000 bp
2000 bp
pc
nc
C
betaPix^ct
Left homology arm
loxP
lox5171
betaPix^m
Splice acceptor
D
o-dianisidine
48 hpf
betaPix^ct/ct
betaPix^m/m
Scale bar: 500μm
E
P<0.0001
Hemorrhage %
Hemorrhage area (mm^2)
betaPix^ct/ct #=289
betaPix^m/m #=409
#=13
F
P<0.0001
P=0.0204
P=0.0006
P=0.8297
P=0.0640
P=0.0576
Relative betaPix expression
Relative RFP expression
Relative alphaPix expression
betaPix^ct/ct
betaPix^ct/m
betaPix^m/m

Figure 2

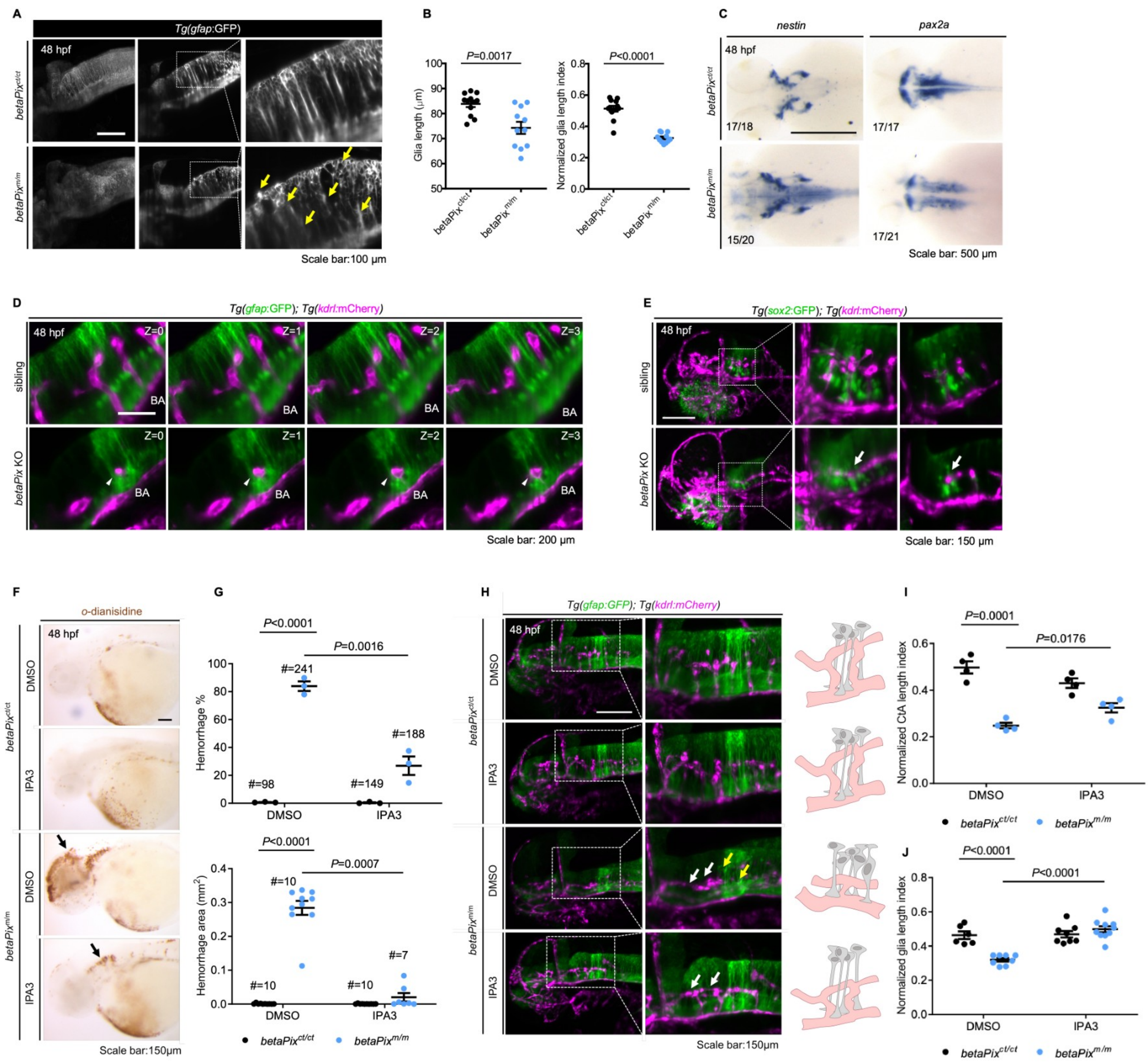
A
Tg(gfap:GFP)
48 hpf
betaPix ct/ct
betaPix m/m
Scale bar:100 µm
B
P=0.0017
Glia length (µm)
P<0.0001
Normalized glia length index
betaPix ct/ct
betaPix m/m
C
nestin
pax2a
48 hpf
17/18
17/17
15/20
17/21
Scale bar: 500 µm
D
Tg(gfap:GFP); Tg(kdrl:mCherry)
48 hpf
Z=0
Z=1
Z=2
Z=3
sibling
betaPix KO
BA
Scale bar: 200 µm
E
Tg(sox2:GFP); Tg(kdrl:mCherry)
48 hpf
sibling
betaPix KO
Scale bar: 150 µm
F
o-dianisidine
48 hpf
DMSO
IPA3
betaPix ct/ct
betaPix m/m
Scale bar:150µm
G
P<0.0001
P=0.0016
Hemorrhage %
#=241
#=188
#=98
#=149
DMSO
IPA3
P<0.0001
P=0.0007
Hemorrhage area (mm2)
#=10
#=7
#=10
#=10
betaPix ct/ct
betaPix m/m
H
Tg(gfap:GFP); Tg(kdrl:mCherry)
48 hpf
DMSO
IPA3
betaPix ct/ct
betaPix m/m
Scale bar:150µm
I
P=0.0001
P=0.0176
Normalized CtA length index
DMSO
IPA3
betaPix ct/ct
betaPix m/m
J
P<0.0001
P<0.0001
Normalized glia length index
DMSO
IPA3
betaPix ct/ct
betaPix m/m

Figure 3

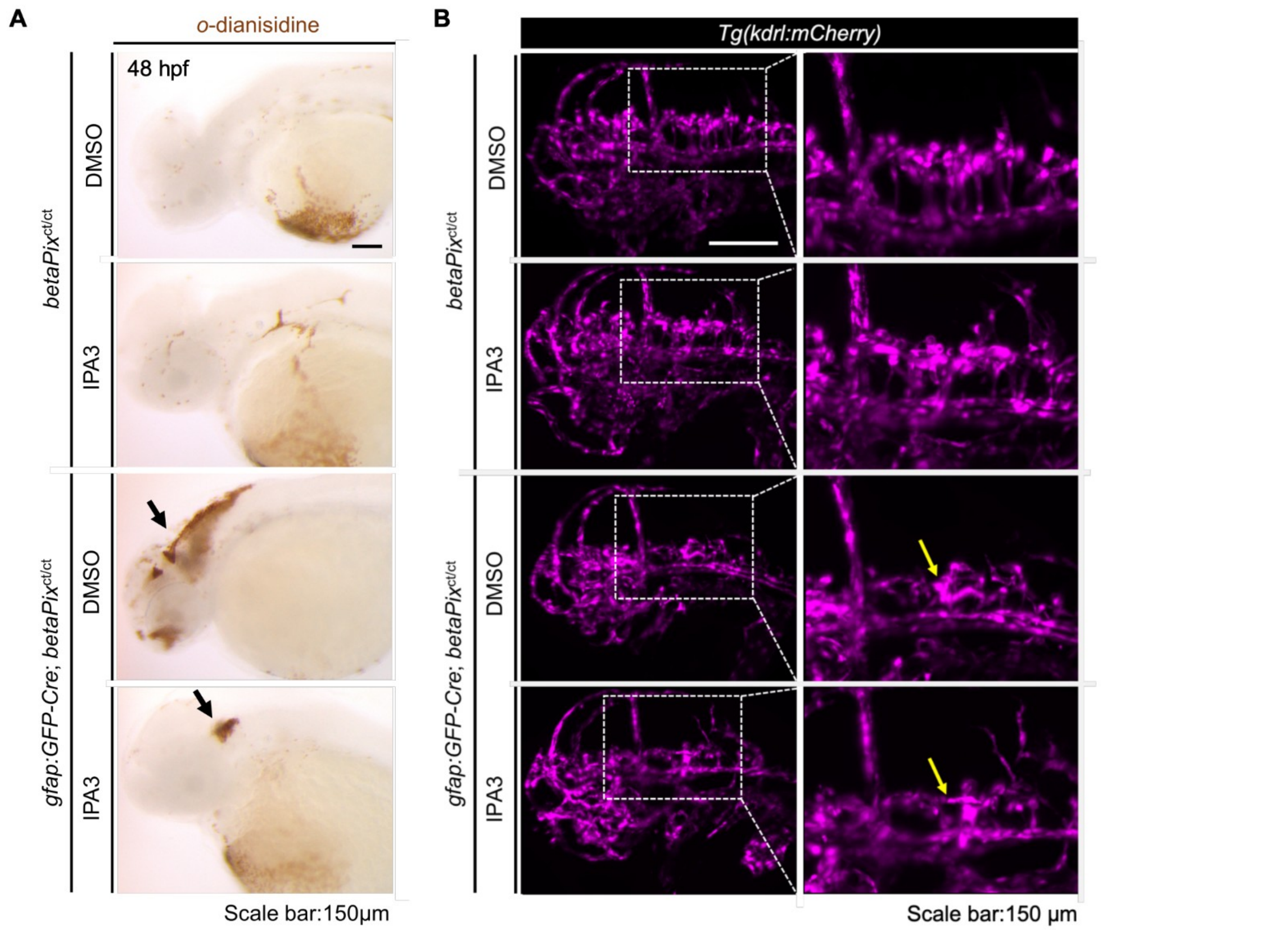
A
o-dianisidine
48 hpf
betaPix ct/ct
gfap:GFP-Cre; betaPix ct/ct
DMSO
IPA3
Scale bar:150μm
B
Tg(kdrl:mCherry)
Scale bar:150 μm

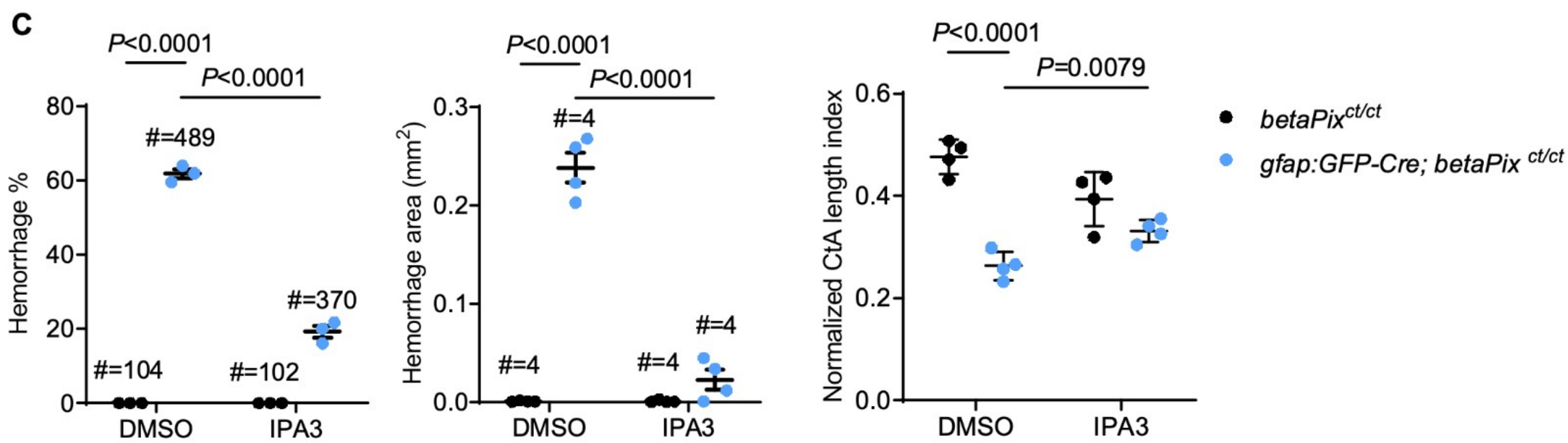
C
P<0.0001
P<0.0001
Hemorrhage %
#=489
#=370
#=104
#=102
DMSO
IPA3
Hemorrhage area (mm2)
#=4
#=4
#=4
#=4
P<0.0001
P=0.0079
Normalized CtA length index
betaPix ct/ct
gfap:GFP-Cre; betaPix ct/ct

Figure 4

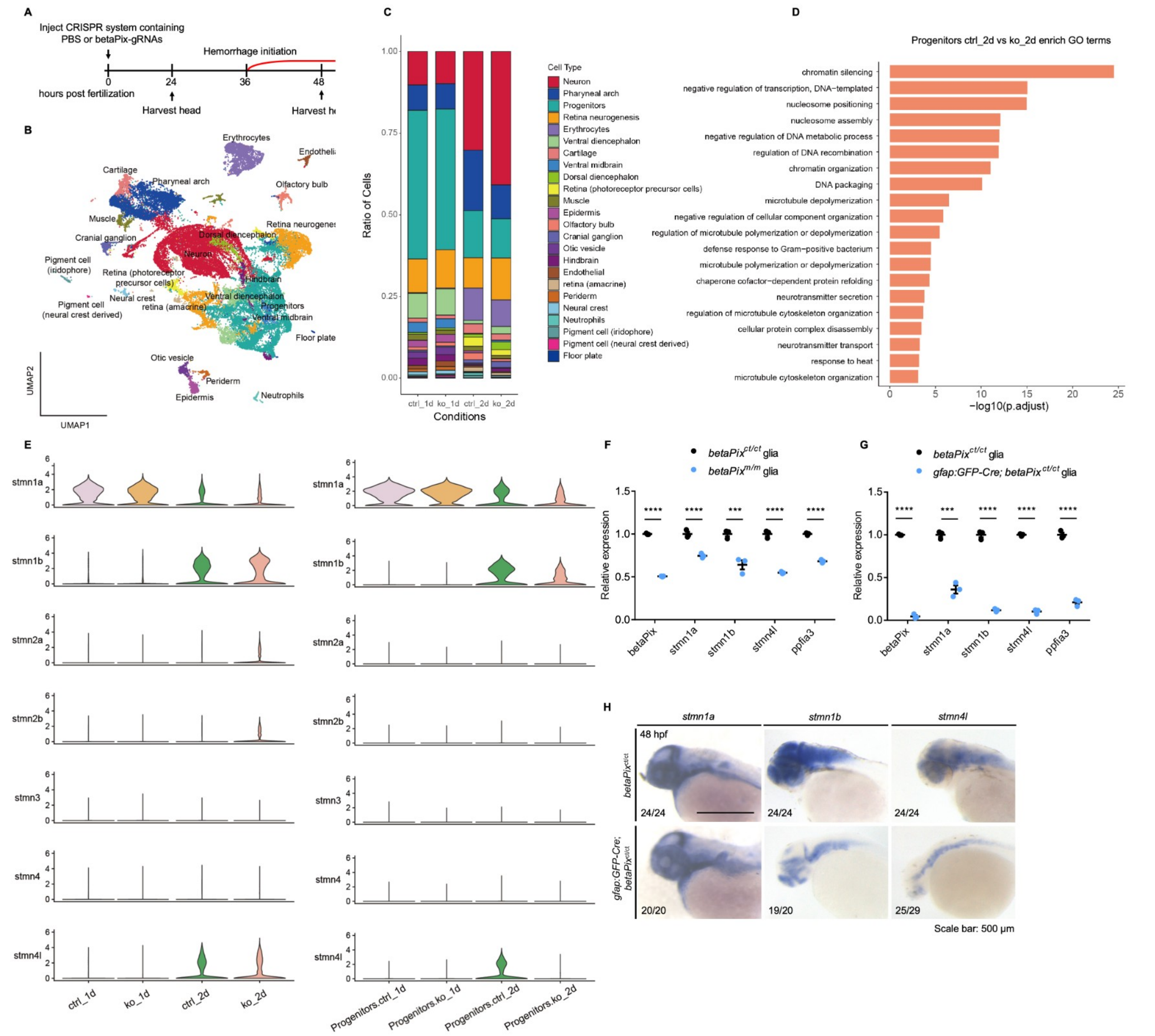
A
Inject CRISPR system containing PBS or betaPix-gRNAs
Hemorrhage initiation
0
24
36
48
hours post fertilization
Harvest head
B
Erythrocytes
Cartilage
Pharyneal arch
Olfactory bulb
Muscle
Retina neurogenesis
Cranial ganglion
Dorsal diencephalon
Neuron
Pigment cell (iridophore)
Retina (photoreceptor precursor cells)
Hindbrain
Neural crest
Ventral diencephalon
Pigment cell (neural crest derived)
retina (amacrine)
Progenitors
Ventral midbrain
Floor plate
Otic vesicle
Periderm
Epidermis
Neutrophils
UMAP2
UMAP1
C
Ratio of Cells
Conditions
ctrl_1d
ko_1d
ctrl_2d
ko_2d
Cell Type
Neuron
Pharyneal arch
Progenitors
Retina neurogenesis
Erythrocytes
Ventral diencephalon
Cartilage
Ventral midbrain
Dorsal diencephalon
Retina (photoreceptor precursor cells)
Muscle
Epidermis
Olfactory bulb
Cranial ganglion
Otic vesicle
Hindbrain
Endothelial
retina (amacrine)
Periderm
Neural crest
Neutrophils
Pigment cell (iridophore)
Pigment cell (neural crest derived)
Floor plate
D
Progenitors ctrl_2d vs ko_2d enrich GO terms
chromatin silencing
negative regulation of transcription, DNA−templated
nucleosome positioning
nucleosome assembly
negative regulation of DNA metabolic process
regulation of DNA recombination
chromatin organization
DNA packaging
microtubule depolymerization
negative regulation of cellular component organization
regulation of microtubule polymerization or depolymerization
defense response to Gram−positive bacterium
microtubule polymerization or depolymerization
chaperone cofactor−dependent protein refolding
neurotransmitter secretion
regulation of microtubule cytoskeleton organization
cellular protein complex disassembly
neurotransmitter transport
response to heat
microtubule cytoskeleton organization
−log10(p.adjust)
E
stmn1a
stmn1b
stmn2a
stmn2b
stmn3
stmn4
stmn4l
ctrl_1d
ko_1d
ctrl_2d
ko_2d
Progenitors.ctrl_1d
Progenitors.ko_1d
Progenitors.ctrl_2d
Progenitors.ko_2d
F
betaPix ct/ct glia
betaPix m/m glia
Relative expression
betaPix
stmn1a
stmn1b
stmn4l
ppfia3
G
betaPix ct/ct glia
gfap:GFP-Cre; betaPix ct/ct glia
Relative expression
betaPix
stmn1a
stmn1b
stmn4l
ppfia3
H
stmn1a
stmn1b
stmn4l
48 hpf
betaPix ct/ct
gfap:GFP-Cre; betaPix ct/ct
24/24
24/24
24/24
20/20
19/20
25/29
Scale bar: 500 μm

Figure 5

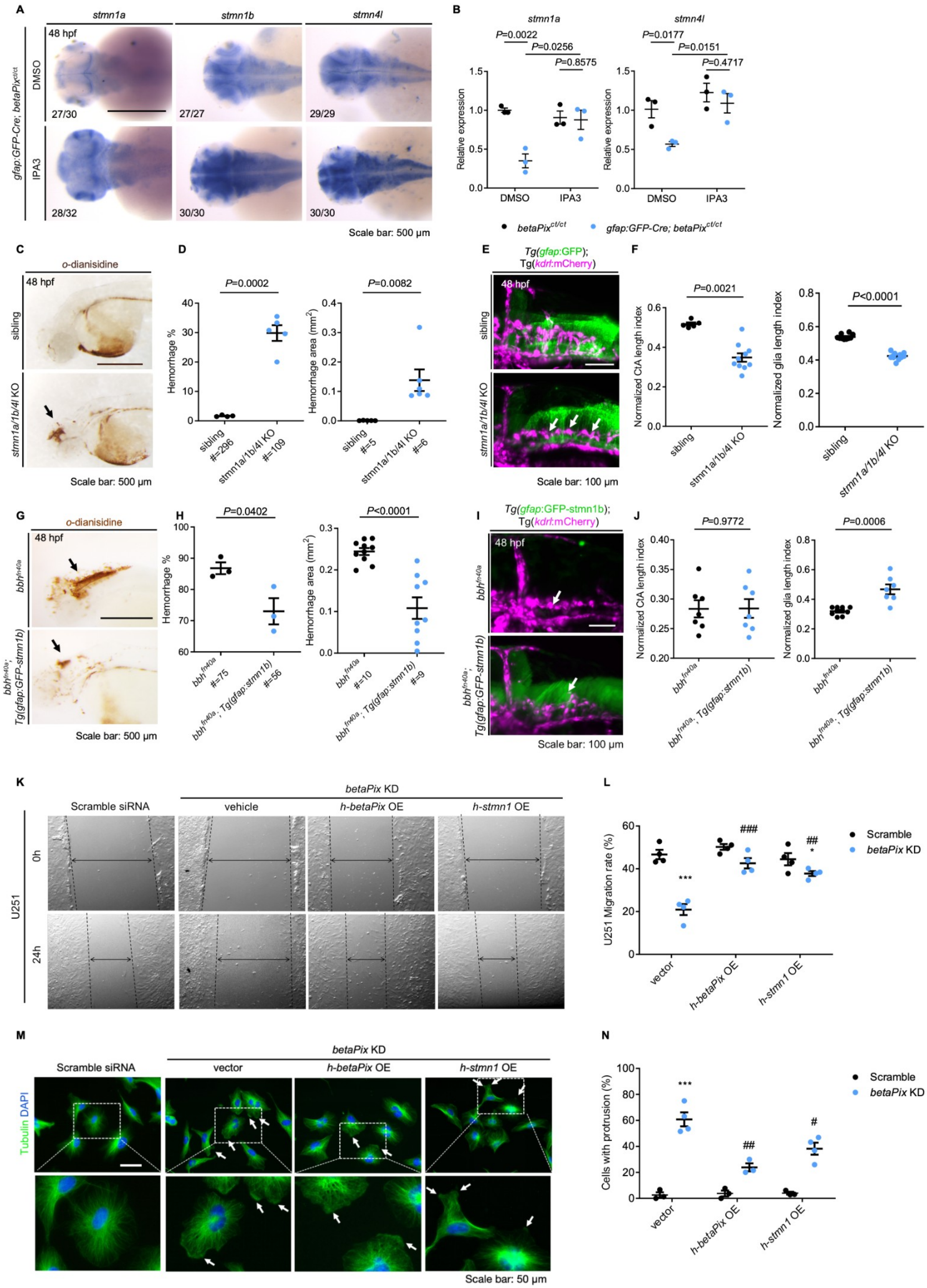
A
stmn1a
stmn1b
stmn4l
gfap:GFP-Cre; betaPix ct/ct
DMSO
IPA3
48 hpf
27/30
27/27
29/29
28/32
30/30
30/30
Scale bar: 500 μm
B
stmn1a
stmn4l
P=0.0022
P=0.0256
P=0.8575
P=0.0177
P=0.0151
P=0.4717
Relative expression
DMSO
IPA3
betaPix ct/ct
gfap:GFP-Cre; betaPix ct/ct
C
o-dianisidine
48 hpf
sibling
stmn1a/1b/4l KO
Scale bar: 500 μm
D
P=0.0002
P=0.0082
Hemorrhage %
Hemorrhage area (mm2)
sibling #=296
stmn1a/1b/4l KO #=109
sibling #=5
stmn1a/1b/4l KO #=6
E
Tg(gfap:GFP); Tg(kdrl:mCherry)
48 hpf
sibling
stmn1a/1b/4l KO
Scale bar: 100 μm
F
P=0.0021
P<0.0001
Normalized CtA length index
Normalized glia length index
sibling
stmn1a/1b/4l KO
G
o-dianisidine
48 hpf
bbh fn40a
bbh fn40a; Tg(gfap:GFP-stmn1b)
Scale bar: 500 μm
H
P=0.0402
P<0.0001
Hemorrhage %
Hemorrhage area (mm2)
bbh fn40a #=75
bbh fn40a; Tg(gfap:stmn1b) #=56
bbh fn40a #=10
bbh fn40a; Tg(gfap:stmn1b) #=9
I
Tg(gfap:GFP-stmn1b); Tg(kdrl:mCherry)
48 hpf
bbh fn40a
bbh fn40a; Tg(gfap:GFP-stmn1b)
Scale bar: 100 μm
J
P=0.9772
P=0.0006
Normalized CtA length index
Normalized glia length index
bbh fn40a
bbh fn40a; Tg(gfap:stmn1b)
K
betaPix KD
Scramble siRNA
vehicle
h-betaPix OE
h-stmn1 OE
U251
0h
24h
L
U251 Migration rate (%)
Scramble
betaPix KD
vector
h-betaPix OE
h-stmn1 OE
M
betaPix KD
Scramble siRNA
vector
h-betaPix OE
h-stmn1 OE
Tubulin DAPI
Scale bar: 50 μm
N
Cells with protrusion (%)
Scramble
betaPix KD
vector
h-betaPix OE
h-stmn1 OE

Figure 6

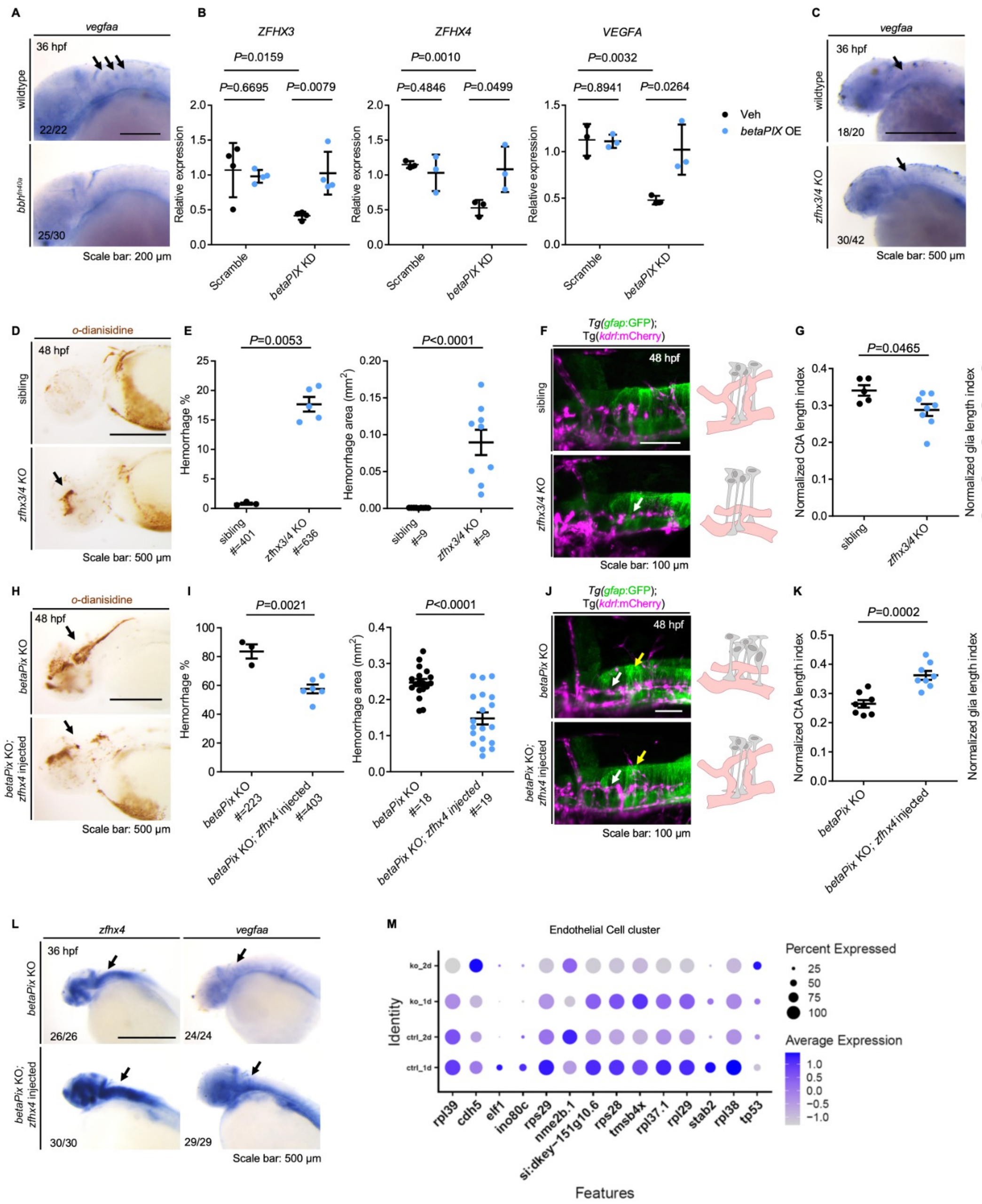
A
vegfaa
36 hpf
wildtype
22/22
bbh fn40a
25/30
Scale bar: 200 µm
B
ZFHX3
P=0.0159
P=0.6695
P=0.0079
ZFHX4
P=0.0010
P=0.4846
P=0.0499
VEGFA
P=0.0032
P=0.8941
P=0.0264
Relative expression
Scramble
betaPIX KD
Veh
betaPIX OE
C
vegfaa
36 hpf
wildtype
18/20
zfhx3/4 KO
30/42
Scale bar: 500 µm
D
o-dianisidine
48 hpf
sibling
zfhx3/4 KO
Scale bar: 500 µm
E
P=0.0053
Hemorrhage %
sibling #=401
zfhx3/4 KO #=636
P<0.0001
Hemorrhage area (mm2)
sibling #=9
zfhx3/4 KO #=9
F
Tg(gfap:GFP); Tg(kdrl:mCherry)
48 hpf
sibling
zfhx3/4 KO
Scale bar: 100 µm
G
P=0.0465
Normalized CtA length index
sibling
zfhx3/4 KO
P=0.3207
Normalized glia length index
H
o-dianisidine
48 hpf
betaPix KO
betaPix KO; zfhx4 injected
Scale bar: 500 µm
I
P=0.0021
Hemorrhage %
betaPix KO #=223
betaPix KO; zfhx4 injected #=403
P<0.0001
Hemorrhage area (mm2)
betaPix KO #=18
betaPix KO; zfhx4 injected #=19
J
Tg(gfap:GFP); Tg(kdrl:mCherry)
48 hpf
betaPix KO
betaPix KO; zfhx4 injected
Scale bar: 100 µm
K
P=0.0002
Normalized CtA length index
betaPix KO
betaPix KO; zfhx4 injected
P=0.0166
Normalized glia length index
L
zfhx4
vegfaa
36 hpf
betaPix KO
26/26
24/24
betaPix KO; zfhx4 injected
30/30
29/29
Scale bar: 500 µm
M
Endothelial Cell cluster
Identity
ko_2d
ko_1d
ctrl_2d
ctrl_1d
rpl39
cdh5
elf1
ino80c
rps29
nme2b.1
si:dkey-151g10.6
rps28
tmsb4x
rpl37.1
rpl29
stab2
rpl38
tp53
Features
Percent Expressed
25
50
75
100
Average Expression
1.0
0.5
0.0
−0.5
−1.0

Figure 7

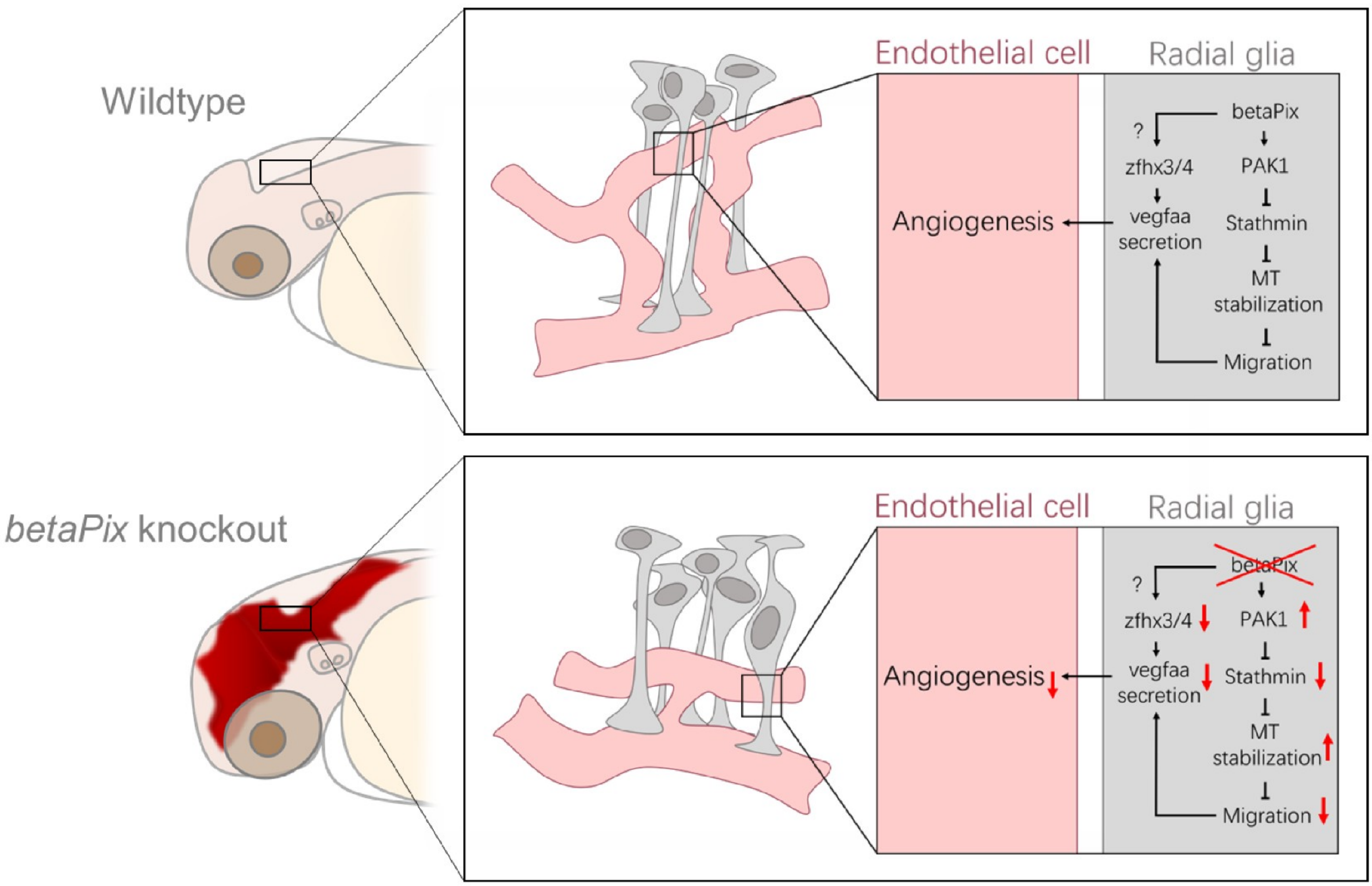
Wildtype
Endothelial cell
Radial glia
betaPix
?
zfhx3/4
PAK1
Angiogenesis
vegfaa secretion
Stathmin
MT stabilization
Migration
betaPix knockout
Endothelial cell
Radial glia
betaPix
?
zfhx3/4
PAK1
Angiogenesis
vegfaa secretion
Stathmin
MT stabilization
Migration

Figure S1

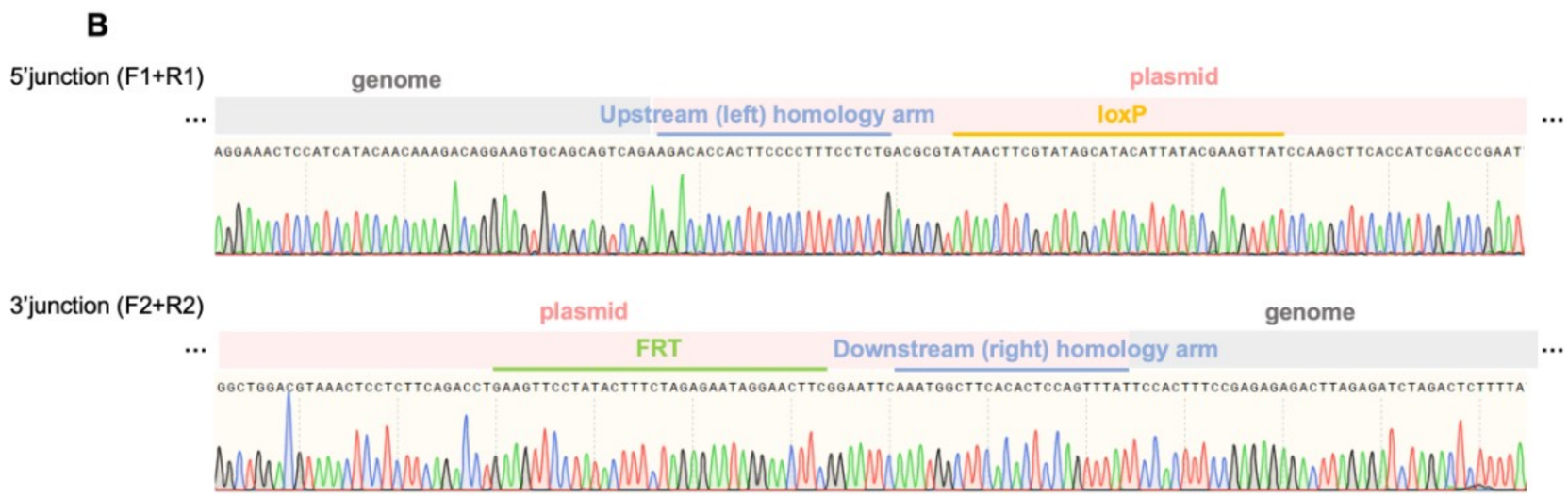

C

Screening process	Number of positive fish	ratio
EGFP screening at F0	184	/
EGFP screening at F1	84	45.65%
Genomic PCR diagnosis	7	8.33%
Sequence diagnosis	2	28.57%
Overall	**2**	**1.09%**

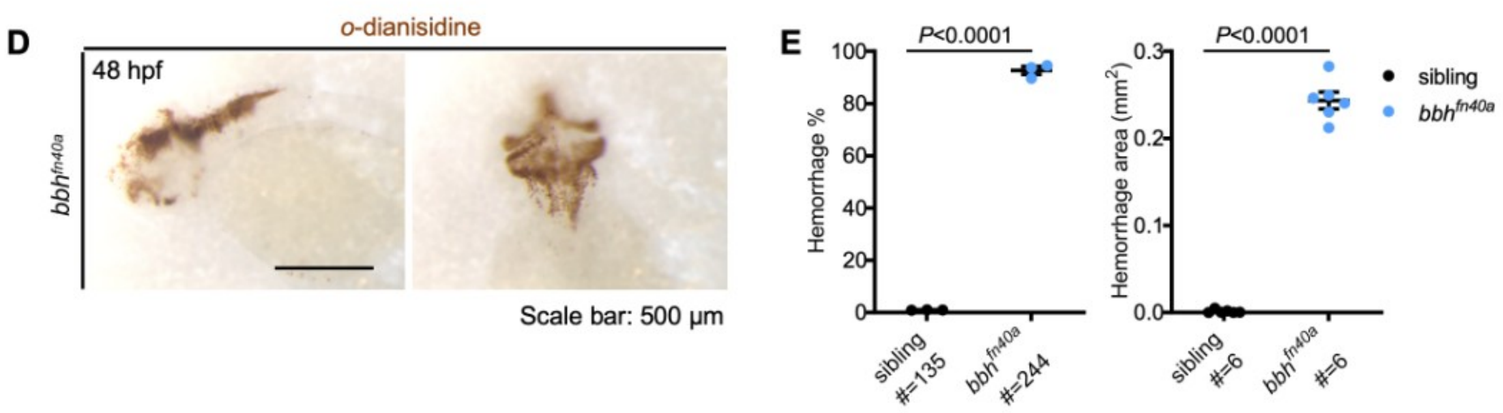

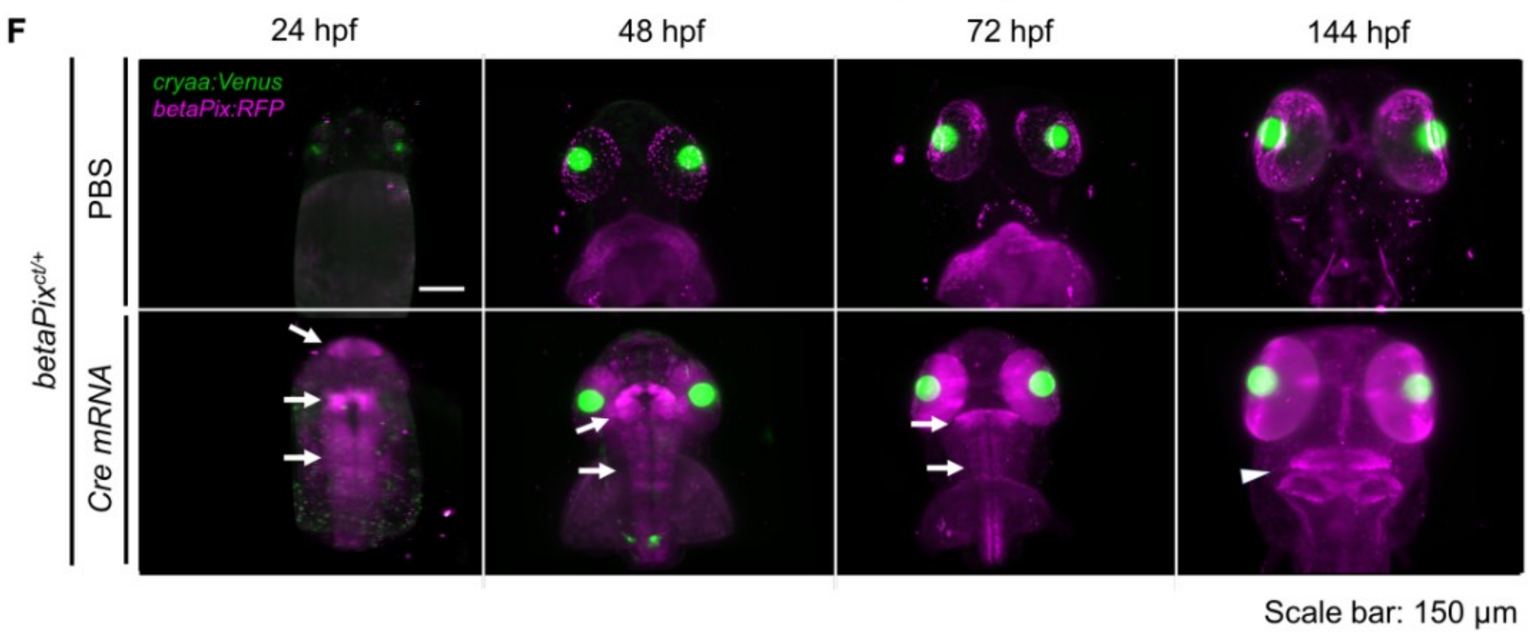

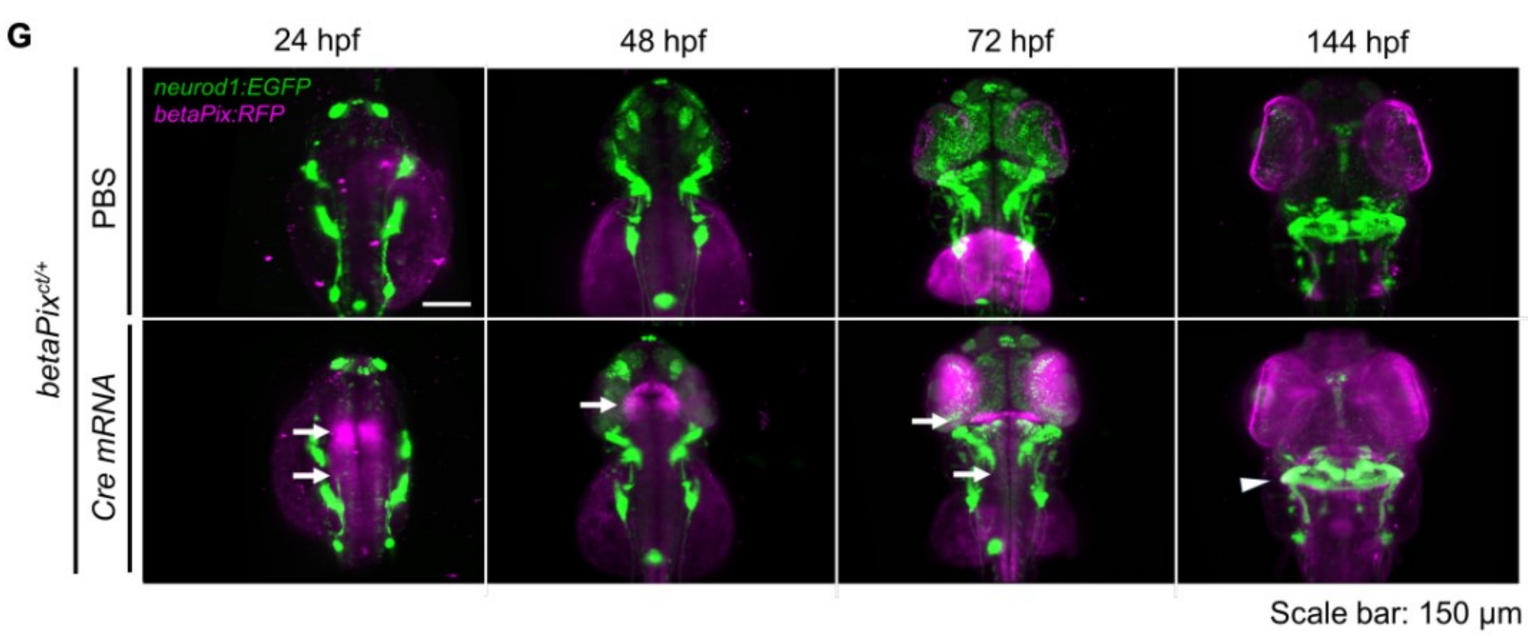

Figure S2

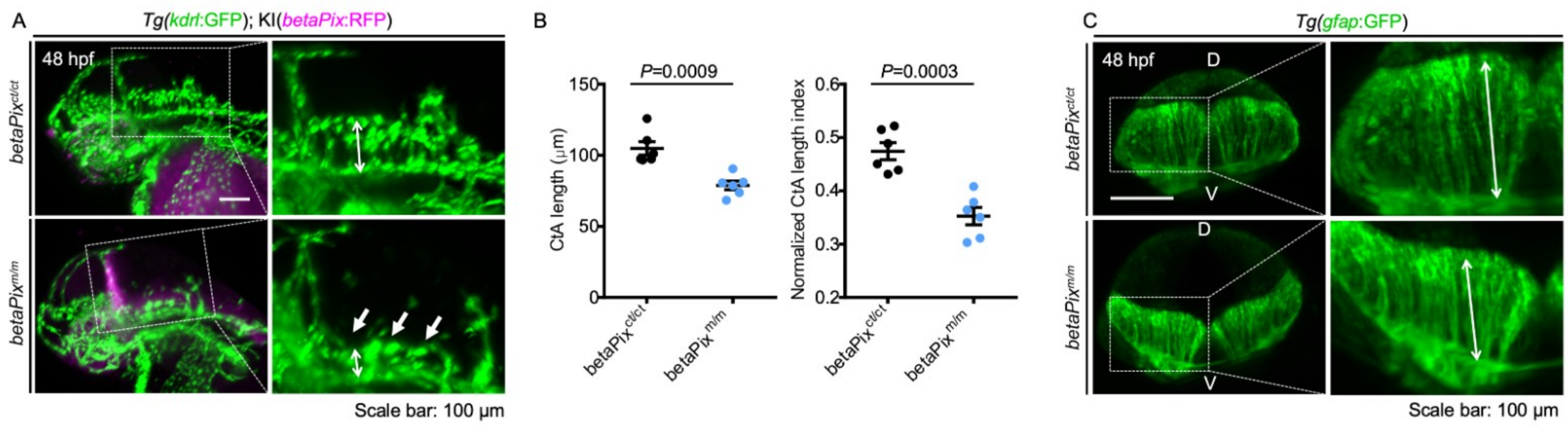
A
Tg(kdrl:GFP); KI(betaPix:RFP)
48 hpf
betaPix ct/ct
betaPix m/m
Scale bar: 100 μm
B
P=0.0009
CtA length (μm)
150
100
50
0
betaPix ct/ct
betaPix m/m
P=0.0003
Normalized CtA length index
0.6
0.5
0.4
0.3
0.2
betaPix ct/ct
betaPix m/m
C
Tg(gfap:GFP)
48 hpf
D
V
betaPix ct/ct
betaPix m/m
Scale bar: 100 μm

Figure S3

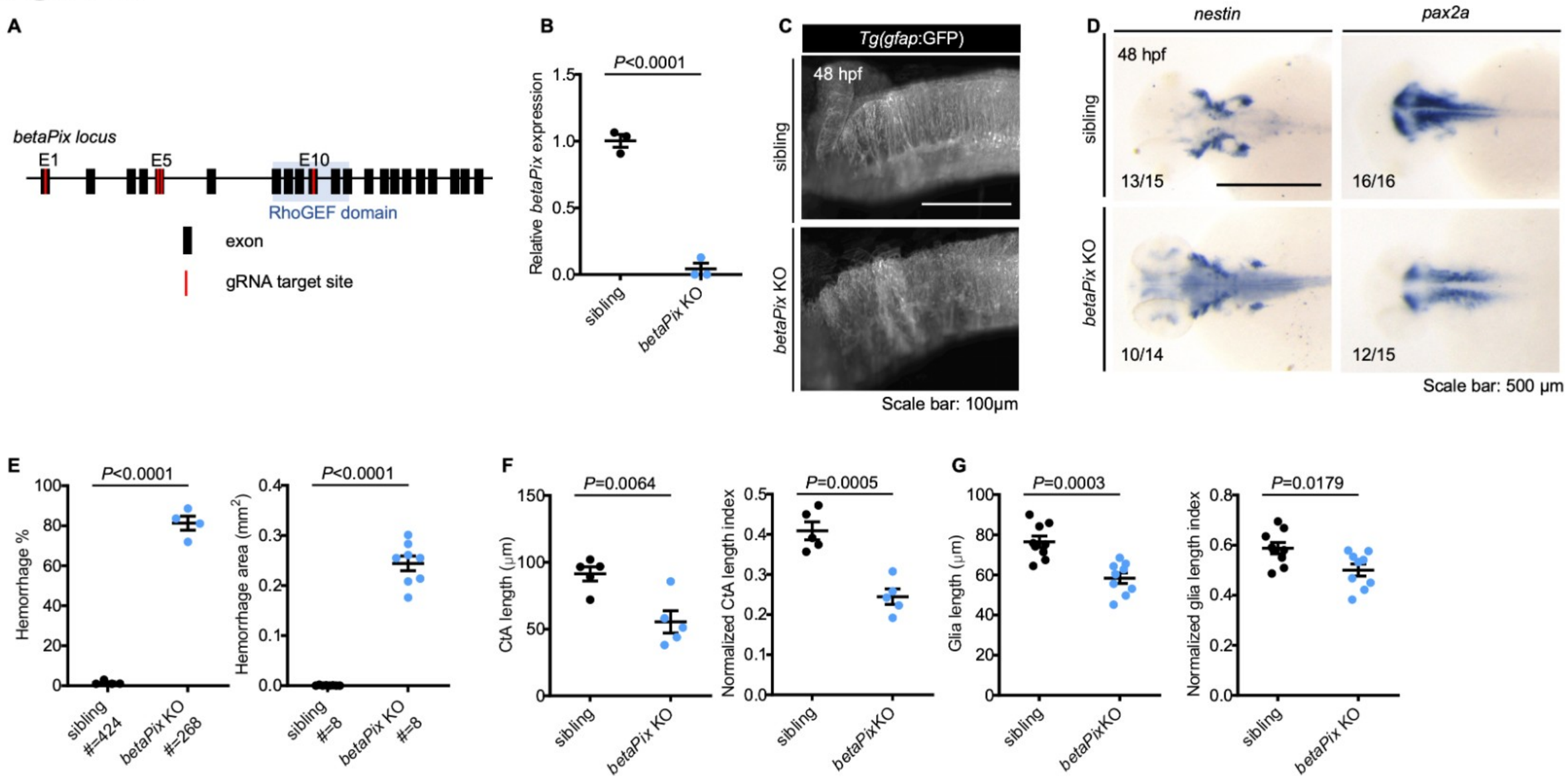
A
betaPix locus
E1
E5
E10
RhoGEF domain
exon
gRNA target site
B
P<0.0001
Relative betaPix expression
1.5
1.0
0.5
0.0
sibling
betaPix KO
C
Tg(gfap:GFP)
48 hpf
sibling
betaPix KO
Scale bar: 100μm
D
nestin
pax2a
48 hpf
sibling
13/15
16/16
betaPix KO
10/14
12/15
Scale bar: 500 μm
E
P<0.0001
Hemorrhage %
100
80
60
40
20
0
sibling #=424
betaPix KO #=268
P<0.0001
Hemorrhage area (mm2)
0.4
0.3
0.2
0.1
0.0
sibling #=8
betaPix KO #=8
F
P=0.0064
CtA length (μm)
150
100
50
0
sibling
betaPix KO
P=0.0005
Normalized CtA length index
0.5
0.4
0.3
0.2
0.1
0.0
sibling
betaPixKO
G
P=0.0003
Glia length (μm)
100
80
60
40
20
0
sibling
betaPixKO
P=0.0179
Normalized glia length index
0.8
0.6
0.4
0.2
0.0
sibling
betaPix KO

Figure S4

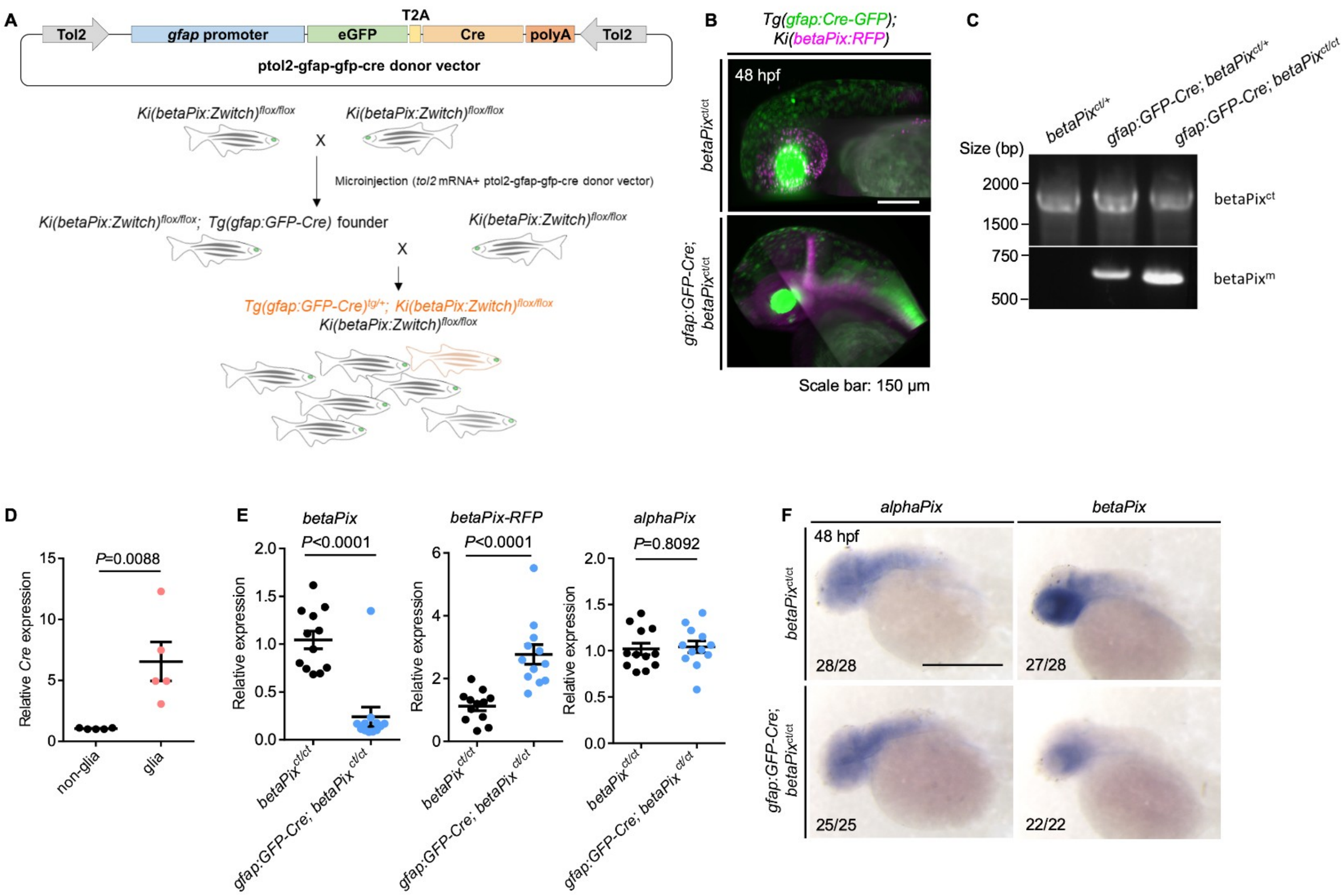
A
Tol2
gfap promoter
eGFP
T2A
Cre
polyA
Tol2
ptol2-gfap-gfp-cre donor vector
Ki(betaPix:Zwitch)flox/flox
Ki(betaPix:Zwitch)flox/flox
X
Microinjection (tol2 mRNA+ ptol2-gfap-gfp-cre donor vector)
Ki(betaPix:Zwitch)flox/flox; Tg(gfap:GFP-Cre) founder
Ki(betaPix:Zwitch)flox/flox
X
Tg(gfap:GFP-Cre)tg/+; Ki(betaPix:Zwitch)flox/flox
Ki(betaPix:Zwitch)flox/flox
B
Tg(gfap:Cre-GFP);
Ki(betaPix:RFP)
48 hpf
betaPixct/ct
gfap:GFP-Cre;
betaPixct/ct
Scale bar: 150 µm
C
betaPixct/+
gfap:GFP-Cre; betaPixct/+
gfap:GFP-Cre; betaPixct/ct
Size (bp)
2000
1500
750
500
betaPixct
betaPixm
D
P=0.0088
Relative Cre expression
15
10
5
0
non-glia
glia
E
betaPix
P<0.0001
betaPix-RFP
P<0.0001
alphaPix
P=0.8092
Relative expression
2.0
1.5
1.0
0.5
0.0
6
4
2
0
betaPixct/ct
gfap:GFP-Cre; betaPixct/ct
F
alphaPix
betaPix
48 hpf
betaPixct/ct
28/28
27/28
gfap:GFP-Cre;
betaPixct/ct
25/25
22/22

Figure S5

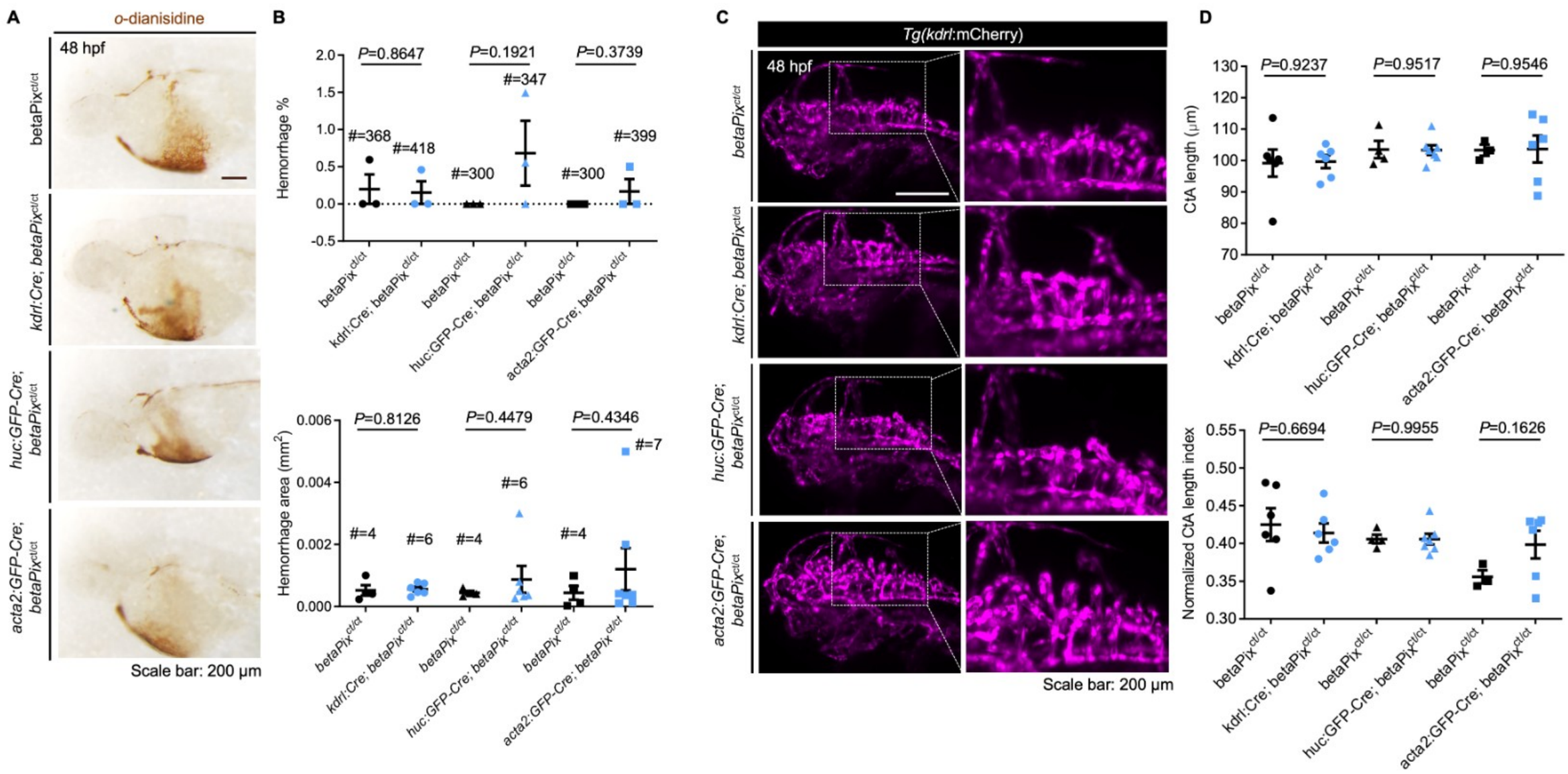
A
o-dianisidine
48 hpf
betaPix ct/ct
kdrl:Cre; betaPix ct/ct
huc:GFP-Cre; betaPix ct/ct
acta2:GFP-Cre; betaPix ct/ct
Scale bar: 200 µm
B
Hemorrhage %
P=0.8647
P=0.1921
P=0.3739
#=368
#=418
#=300
#=347
#=300
#=399
Hemorrhage area (mm2)
P=0.8126
P=0.4479
P=0.4346
#=4
#=6
#=4
#=6
#=4
#=7
betaPix ct/ct
kdrl:Cre; betaPix ct/ct
huc:GFP-Cre; betaPix ct/ct
acta2:GFP-Cre; betaPix ct/ct
C
Tg(kdrl:mCherry)
48 hpf
Scale bar: 200 µm
D
CtA length (µm)
P=0.9237
P=0.9517
P=0.9546
Normalized CtA length index
P=0.6694
P=0.9955
P=0.1626

Figure S6

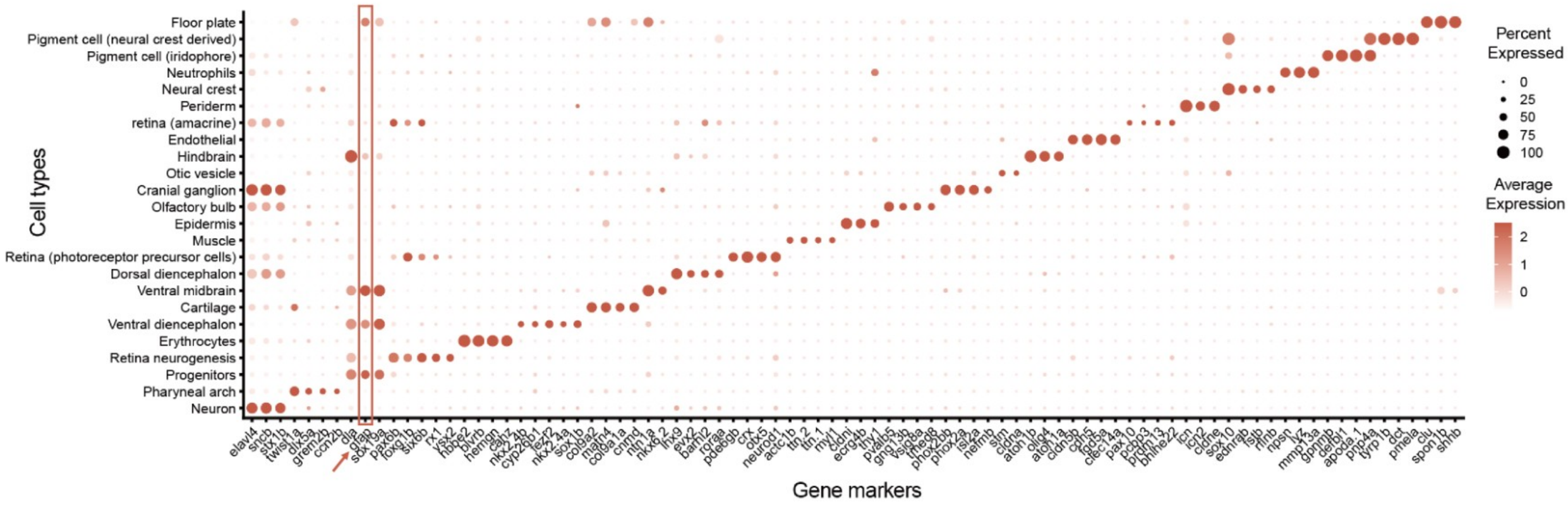
A
Cell types
Floor plate
Pigment cell (neural crest derived)
Pigment cell (iridophore)
Neutrophils
Neural crest
Periderm
retina (amacrine)
Endothelial
Hindbrain
Otic vesicle
Cranial ganglion
Olfactory bulb
Epidermis
Muscle
Retina (photoreceptor precursor cells)
Dorsal diencephalon
Ventral midbrain
Cartilage
Ventral diencephalon
Erythrocytes
Retina neurogenesis
Progenitors
Pharyneal arch
Neuron
Gene markers
Percent Expressed
0
25
50
75
100
Average Expression
2
1
0

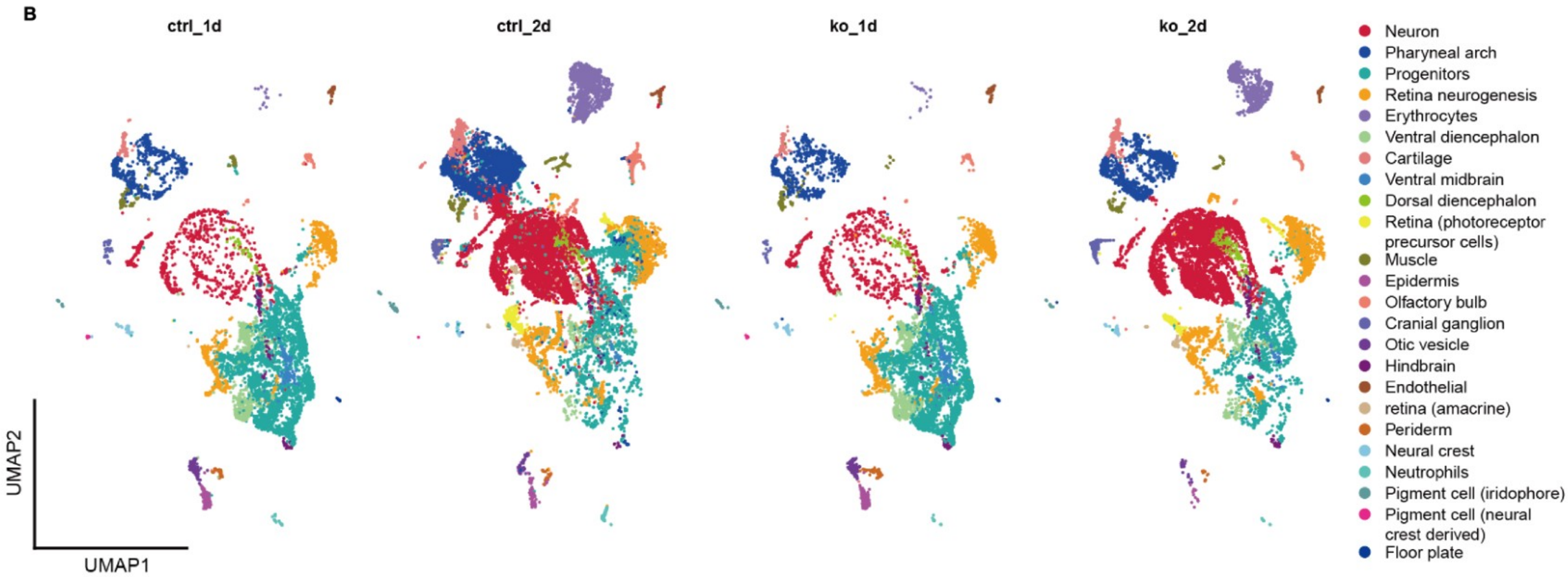
B
ctrl_1d
ctrl_2d
ko_1d
ko_2d
UMAP2
UMAP1
Neuron
Pharyneal arch
Progenitors
Retina neurogenesis
Erythrocytes
Ventral diencephalon
Cartilage
Ventral midbrain
Dorsal diencephalon
Retina (photoreceptor precursor cells)
Muscle
Epidermis
Olfactory bulb
Cranial ganglion
Otic vesicle
Hindbrain
Endothelial
retina (amacrine)
Periderm
Neural crest
Neutrophils
Pigment cell (iridophore)
Pigment cell (neural crest derived)
Floor plate

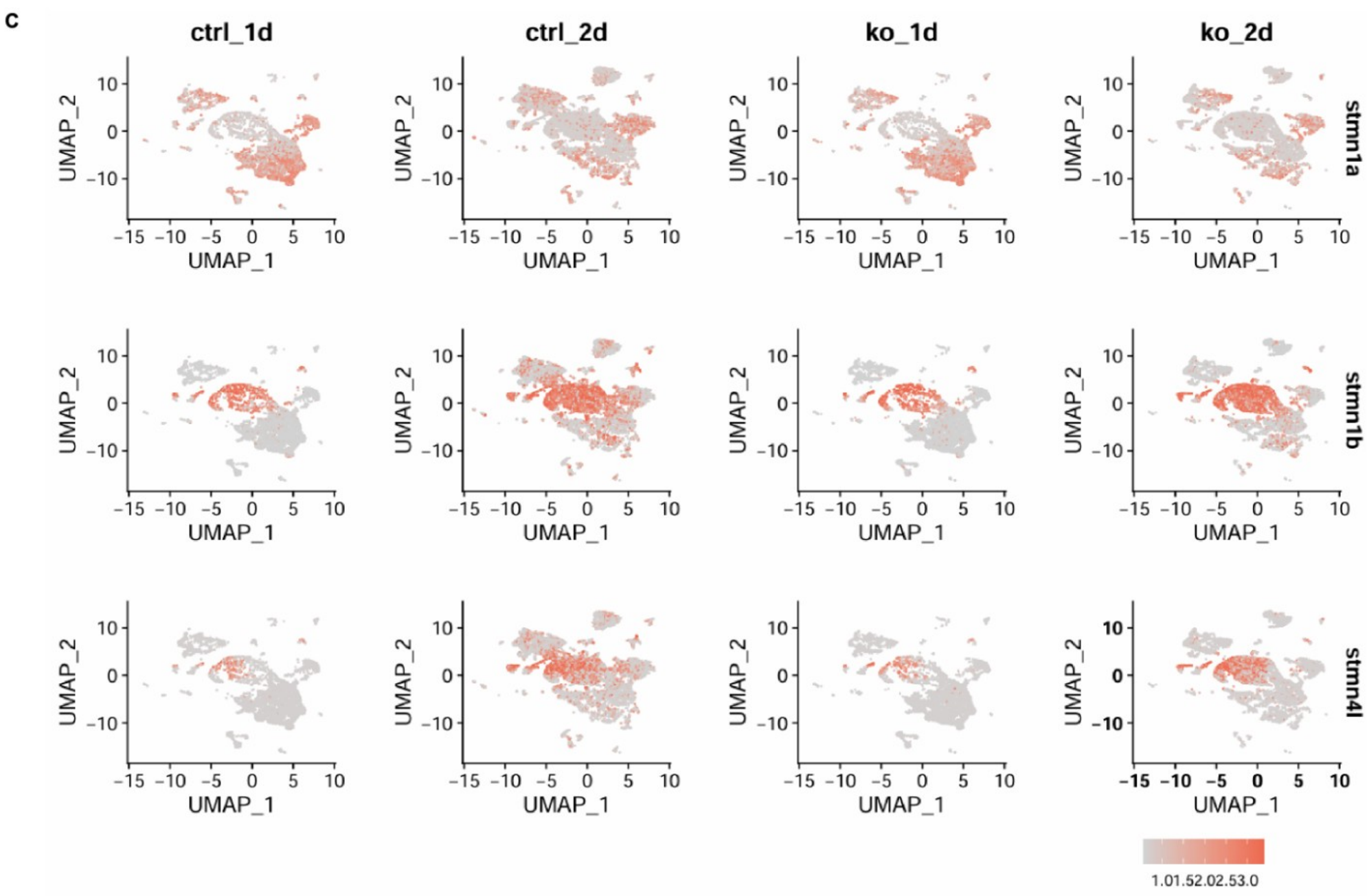
c
ctrl_1d
ctrl_2d
ko_1d
ko_2d
UMAP_2
UMAP_1
stmn1a
stmn1b
stmn4l
1.01.52.02.53.0

Figure S7

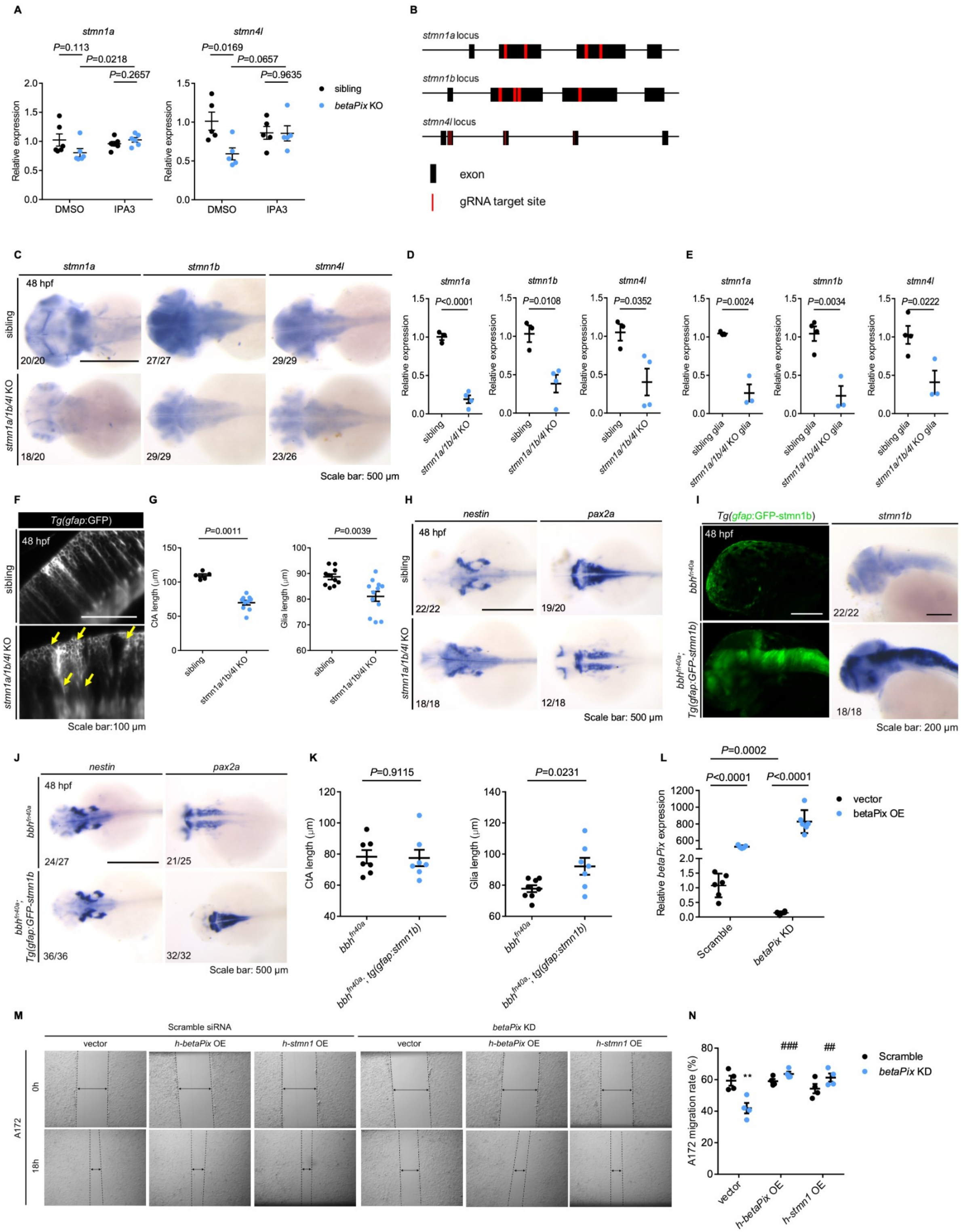
A
stmn1a
stmn4l
P=0.113
P=0.0218
P=0.2657
P=0.0169
P=0.0657
P=0.9635
Relative expression
DMSO
IPA3
sibling
betaPix KO
B
stmn1a locus
stmn1b locus
stmn4l locus
exon
gRNA target site
C
stmn1a
stmn1b
stmn4l
48 hpf
sibling
stmn1a/1b/4l KO
20/20
27/27
29/29
18/20
29/29
23/26
Scale bar: 500 μm
D
P<0.0001
P=0.0108
P=0.0352
sibling
stmn1a/1b/4l KO
E
P=0.0024
P=0.0034
P=0.0222
sibling glia
stmn1a/1b/4l KO glia
F
Tg(gfap:GFP)
48 hpf
sibling
stmn1a/1b/4l KO
Scale bar:100 μm
G
P=0.0011
P=0.0039
CtA length (μm)
Glia length (μm)
sibling
stmn1a/1b/4l KO
H
nestin
pax2a
48 hpf
sibling
stmn1a/1b/4l KO
22/22
19/20
18/18
12/18
Scale bar: 500 μm
I
Tg(gfap:GFP-stmn1b)
stmn1b
48 hpf
bbh fn40a
bbh fn40a; Tg(gfap:GFP-stmn1b)
22/22
18/18
Scale bar: 200 μm
J
nestin
pax2a
48 hpf
bbh fn40a
bbh fn40a; Tg(gfap:GFP-stmn1b)
24/27
21/25
36/36
32/32
Scale bar: 500 μm
K
P=0.9115
P=0.0231
CtA length (μm)
Glia length (μm)
bbh fn40a
bbh fn40a; tg(gfap:stmn1b)
L
P=0.0002
P<0.0001
P<0.0001
Relative betaPix expression
vector
betaPix OE
Scramble
betaPix KD
M
Scramble siRNA
betaPix KD
vector
h-betaPix OE
h-stmn1 OE
A172
0h
18h
N
A172 migration rate (%)
**
###
##
Scramble
betaPix KD
vector
h-betaPix OE
h-stmn1 OE

Figure S8

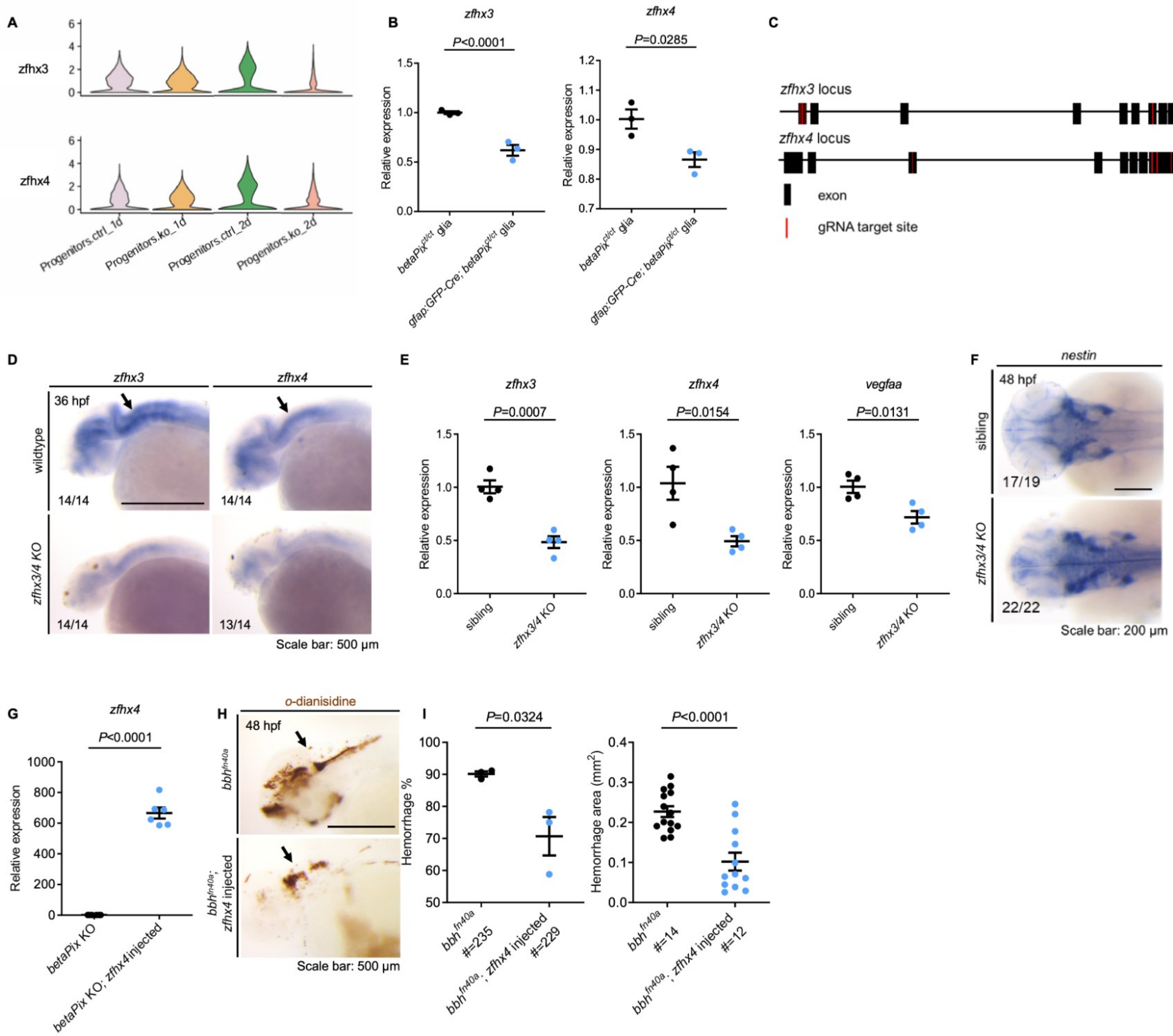
A
zfhx3
zfhx4
Progenitors.ctrl_1d
Progenitors.ko_1d
Progenitors.ctrl_2d
Progenitors.ko_2d
B
zfhx3
P<0.0001
zfhx4
P=0.0285
Relative expression
betaPix ct/ct glia
gfap:GFP-Cre; betaPix ct/ct glia
C
zfhx3 locus
zfhx4 locus
exon
gRNA target site
D
zfhx3
zfhx4
36 hpf
wildtype
zfhx3/4 KO
14/14
14/14
14/14
13/14
Scale bar: 500 µm
E
zfhx3
P=0.0007
zfhx4
P=0.0154
vegfaa
P=0.0131
Relative expression
sibling
zfhx3/4 KO
F
nestin
48 hpf
sibling
zfhx3/4 KO
17/19
22/22
Scale bar: 200 µm
G
zfhx4
P<0.0001
Relative expression
betaPix KO
betaPix KO; zfhx4 injected
H
o-dianisidine
48 hpf
bbh fn40a
bbh fn40a; zfhx4 injected
Scale bar: 500 µm
I
P=0.0324
Hemorrhage %
bbh fn40a
#=235
bbh fn40a; zfhx4 injected
#=229
P<0.0001
Hemorrhage area (mm2)
bbh fn40a
#=14
bbh fn40a; zfhx4 injected
#=12

Supplementary Table 1.xlsx

Supplementary Table 2 | Primers used for siRNA

Gene	Forward
betaPIX	AGCCUUCAGAUGAGGAGUUCGCGTC
STMN1	UAAAGAGAACCGAGAGGCA

Supplementary Table 3 | Primers used for guide RNA synthesis

oligo	
betaPix-1	TAATACGACTCACTATAGGATGCCTGCAAAAATCCTTGTTTTAGAGCTAGAAATAGC
betaPix-2	TAATACGACTCACTATAGGACGAGTTATCCTTCAGCAGTTTTAGAGCTAGAAATAGC
betaPix-3	TAATACGACTCACTATAGGCGCTCTCAATGGCAAAACGTTTTAGAGCTAGAAATAGC
betaPix-4	TAATACGACTCACTATAGGAGAGTTCATGGAAAGTAAGTTTTAGAGCTAGAAATAGC
stmn1a-1	TAATACGACTCACTATAGAGCTGGACAAGCGTGCTTCGTTTTAGAGCTAGAAATAGC
stmn1a-2	TAATACGACTCACTATAGAAGAAGGACCTTTCCTTGGGTTTTAGAGCTAGAAATAGC
stmn1a-3	TAATACGACTCACTATAAGAAAAGCGTGAGCATGAAAGTTTTAGAGCTAGAAATAGC
stmn1a-4	TAATACGACTCACTATAGAAACTGAACCAGAAAATGGGTTTTAGAGCTAGAAATAGC
stmn1b-1	TAATACGACTCACTATAGGACAAGCGTGCCTCAGGACGTTTTAGAGCTAGAAATAGC
stmn1b-2	TAATACGACTCACTATAGGGAATTCTCCCTTGGCATCGTTTTAGAGCTAGAAATAGC
stmn1b-3	TAATACGACTCACTATAGGAAAGTGGGAATTCTCCCTGTTTTAGAGCTAGAAATAGC
stmn1b-4	TAATACGACTCACTATAGGAGGTCCTTCAGAAAGCTAGTTTTAGAGCTAGAAATAGC
stmn4l-1	TAATACGACTCACTATAGAGCAGAAGAGAGACACTAGGTTTTAGAGCTAGAAATAGC
stmn4l-2	TAATACGACTCACTATAGGGAATTATCAAAGACATGGGTTTTAGAGCTAGAAATAGC
stmn4l-3	TAATACGACTCACTATAAGTGAAGGGTCCCGGCGAGGGTTTTAGAGCTAGAAATAGC
stmn4l-4	TAATACGACTCACTATAGGCTCACATCGCCGCCATGCGTTTTAGAGCTAGAAATAGC
zfhx3-1	TAATACGACTCACTATAGGGAGAGGGAGCTCACCAAAGTTTTAGAGCTAGAAATAGC
zfhx3-2	TAATACGACTCACTATAGGGCGATCCCTCACTTGGAGGTTTTAGAGCTAGAAATAGC
zfhx3-3	TAATACGACTCACTATAGGGCTCCACAGTTGGCAGCTGTTTTAGAGCTAGAAATAGC
zfhx3-4	TAATACGACTCACTATAGGCCCACTTCGTGAGCAATGGTTTTAGAGCTAGAAATAGC
zfhx4-1	TAATACGACTCACTATAGGTTGTCTTCATCTGGAGGAGTTTTAGAGCTAGAAATAGC
zfhx4-2	TAATACGACTCACTATAGGAACTGAAACCACTAAAGGGTTTTAGAGCTAGAAATAGC
zfhx4-3	TAATACGACTCACTATAGGAAGTGCGGAAAGAACGCTGTTTTAGAGCTAGAAATAGC
zfhx4-4	TAATACGACTCACTATAGGCTGGCAAGTTGAGTACATGTTTTAGAGCTAGAAATAGC
UgRNA	TAATACGACTCACTATAGGGAGGCGTTCGGGCCACAGGTTTTAGAGCTAGAAATAGC
Universal bottom-strand Ultramer	AAAAGCACCGACTCGGTGCCACTTTTTCAAGTTGATAACGGACTAGCCTTATTTTAACTTGCTATTTCTAGCTCTAAAAC

Supplementary Table 4 | Primers used for WISH probe synthesis

Gene	Forward	Reverse*
alphaPix	GGACACTCTCGATCCCAAACTGAC	GCCACACACTCCCGTCTCAC
betaPix	GCCATACACTGCCCTCTCACC	GCAGCTTTGCCAGACCACATC
RFP	GTGTCTAAGGGCGAAGAGCTGAT	CAGTTTGCTAGGGAGGTCGCAG
stmn1a	GGCTGCTACAAGTGACATTCAGG	GCAGACAGTAACAGGCATGTTAAGC
stmn1b	GCGTCCTCTGGAGCTGATATCC	GGCAGTGGCAAAACTGGCAC
stmn2a	CTGGAGGCGGCTGAGGAC	CAAGCTGTCTATCCGAAGGGTCC
stmn4l	ATGACTCTCGCCGCGTACAG	GATGCAAGTCAACTGTGGCCAC
vegfaa	ACTCACCGCAACACTCCACT	GAGCAAGGCTCACAGTGGTT
zfhx3	CTGAGCAGCACGAAGTGGATG	CAATCTGATGGAGTCCGATCCTACAC
zfhx4	GTTACAGGACAACGCGCATATCC	CACCCTTGACAGCGTTCACATTC

*The T7 sequence TAATACGACTCACTATAGGG was added to the 5' end of each reverse primer.

Supplementary Table 5 | Primers used for qRT-PCR

Zebrafish Gene	Forward	Reverse
alphaPix	ATGTTAAACCTTTAACCATGCCTGG	TTAGTGACCTCCTTCATCCCAGGAA
betaPix	GACCAAAGGCTCCGACAAAC	GGCCTTGGGTGGACTCTTC
cre	AATTTACTGACCGTACACCAAA	ATAACCAGTGAAACAGCATTGC
gapdh	GATACACGGAGCACCAGGTT	GCCATCAGGTCACATACACG
pak1	CTCTGCTGGGAGTATAGTCAGCG	CTGCTGCTGCAGGTTCATCTG
ppfia3	CCAGACGAGGATGGCACTAAGAC	CCCTTGGAGATGCATCGCTCTG
RFP	GTGTCTAAGGGCGAAGAGCTGAT	GGTGGTTGTTCACGGTGCC
stmn1a	GGCTGCTACAAGTGACATTCAGG	CATAGCTGCCATAATTGCTGTACGG
stmn1b	GCGTCCTCTGGAGCTGATATCC	CTGCCTCATGGTTCTTGCGTC
stmn4l	CACATTCCCACCTCGCCG	CTCAGCATGCTTGTCCTTCTCC
vegfaa	TCCAGGAGTATCCCGATGAG	GCTTTGACTTCTGCCTTTGG
zfhx3	GCCACTGTGGCAGCATCAG	CAGGCTCAGCATCTGCCAC
zfhx4	GAGCAGGTGCAGCAATGCC	CGCAGCTGAATGCAATGCAAG
ZO-1	CCGAACCCATCAACCGCATC	GAGTGAGATCCTTGGCACTCGG

Human Gene	Forward	Reverse
betaPIX	CCTCACGGAACACAGTGAGGAG	GTCAGGATCTGCAGCTCAAGC
gapdh	CGCTGAGTACGTCGTGGAGTC	CAGGAGGCATTGCTGATGATCTTG
pak1	GTGAAGGCTGTGTCTGAGACTC	GGAAGTGGTTCAATCACAGACCG
stmn1	GAACTGGAGAAGCGTGCCTCAG	CTTCAGTCTCGTCAGCAGGGTC
VEGFA	CCATGCCAAGTGGTCCCAG	GGTCTCGATTGGATGGCAGTAGC
ZFHX3	CCACGGACCCAGAAGAAGCC	CTTCTCTGCTTGGCTGGACG
ZFHX4	CAGAGGAGGACAACCTCAGTGAG	CCTCACTTTGTTCTTCTGAGGTCG
ZO-1	CCTGGGGCTGTCTCAACTCC	CATGCTGGGCCGAAGAATCC